

# Period of Eclipsing Binary EPIC 201458798

IVAN ALTUNIN<sup>1</sup>, RYAN CAPUTO<sup>1</sup>, AND KALÉE TOCK<sup>1</sup>

<sup>1</sup>Stanford Online High School, Stanford, California, United States

\*Corresponding author: [ialtunin@ohs.stanford.edu](mailto:ialtunin@ohs.stanford.edu), [ryanjc@ohs.stanford.edu](mailto:ryanjc@ohs.stanford.edu)

In this study we observed and determined the period of the eclipsing binary star EPIC 201458798, finding that its period has not changed since it was last measured and published in the Kepler catalog in 2014. We did this by developing Python code to determine the period using two independent algorithms and partially automating the search for suitable comparison stars. Our system was imaged by the 0.4m Las Cumbres Observatory telescopes in four filters. We analyzed six photometry types returned for each image from the Our Solar Siblings pipeline. Of these photometries, we found source extractor kron (sek) to be the most appropriate type for our 2x2 binned images of EPIC 201458798. Both of the period-finding algorithms we developed gave results that were not statistically different from the Kepler catalog period for the infrared, red, and visual filter images. The blue filter images were statistically different from the Kepler catalog period for one of our algorithms but not the other.

© 2020 Astronomy Theory, Observations and Methods Journal

**Keywords:** binaries: eclipsing — celestial mechanics – methods: data analysis – techniques: photometric

<https://doi.org/10.32374/atom.2020.1.1>

## INTRODUCTION

A subset of binary star systems are known as eclipsing binaries (EBs). These systems are aligned such that the two orbiting stars eclipse each other relative to Earth's line of sight. This produces a change in the observed brightness of the system as a function of time. Although most EBs are so close together that they appear as a single source of light, this brightness change during their eclipses allows us to deduce their characteristics, including period and position on the Hertzsprung-Russell diagram (Southworth, 2012). This makes EBs a primary and direct source of information on star properties and stellar evolution.

In this study, we measure EPIC 201458798, a short period ( $p < 1$  day) EB, and confirm the Third Revision

of the Kepler Eclipsing Binary Catalog's period for this system using our own period-finding algorithms and an independently acquired data set (Kirk, 2016). In the process, we examine some photometric considerations that arise when using 0.4m LCO telescopes with 2x2 image binning.

## TARGET SELECTION

We chose an EB that was visible during the early spring because that was when our study was conducted. The Kepler 1 campaign contained stars that were observable during the spring, so we searched the Kepler Catalog in this campaign (Kirk, 2016).

Furthermore, we narrowed our selection to detached EBs, excluding semi-attached and contact bi-

naries. Since detached binaries are completely separate, they can yield more accurate estimates of relative masses and temperatures of the individual stars (Rozmus, 2010). When searching the Kepler catalog, we were looking for a target with a Morph between 0 and 0.5. The Morph metric was developed for the second release of Kepler data to classify EBs by the shape of the primary eclipse. A system with Morph  $c < 0.5$  is predominantly detached, a Morph of  $0.5 < c < 0.7$  is semi-detached, and a Morph of  $0.7 < c < 0.8$  is an overcontact binary (Matijevic, 2012).

In addition, our target had to have a period less than 1.5 days both to avoid using excessive telescope time and because we wanted to collect sufficient images to calculate the period from our own observations within a few weeks. The target also had to be sufficiently bright for the ground-based 0.4m LCO telescopes to observe it; a system with  $k_{\text{mag}}$  less than 13 was optimal. Finally, the eclipses needed to be deep enough to be accessible for analysis. A primary eclipse depth that was at 0.8 or deeper on a plot of normalized flux was deemed adequate.

## OUR TARGET

Applying the criteria specified above, we settled on EPIC 201458798 as our target star. This system's characteristics are shown in Table 1. The target star has a magnitude ( $k_{\text{mag}}$ ) close to 12 and a primary eclipse that causes its brightness to dip to 0.75 on a plot of normalized flux versus phase. Its lightcurve from the Kepler Eclipsing Binary Catalog, Third Revision, is shown in Figure 1 (Kirk, 2016).

**Table 1. Characteristics of EPIC201458798**

Property	Value
RA (deg)	168.2801
Dec (deg)	-0.0925
$k_{\text{mag}}$	12.091
Period (days)	0.6193964
Period Error	0.0000347
Morph	0.13

## OBSERVATION HISTORY

Our target was observed by Kepler from June 2, 2014 to August 21, 2014. These dates were found by con-

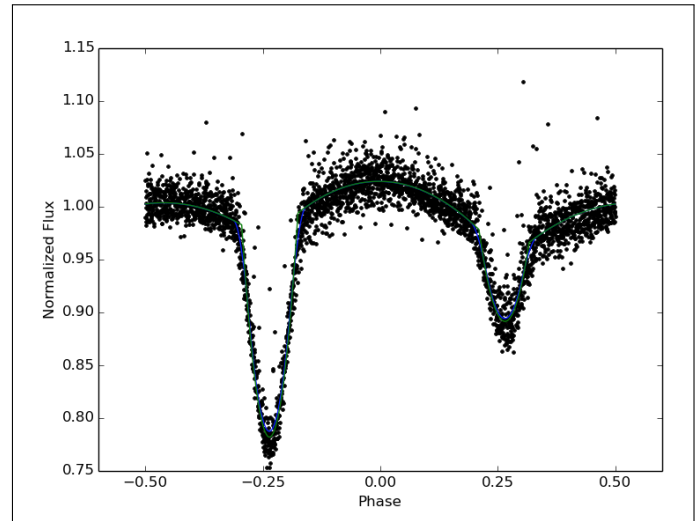


**Fig. 1.** EPIC 201458798 light curve from the Kepler Eclipsing Binary Catalog, Third Revision.

verting the modified Julian dates of the observations listed under “LC data” on the Kepler catalog website to the calendar date. In 2016, our target was part of the study “Planet Hunters K2” which aimed to detect exoplanets orbiting eclipsing binary stars. This study collected data on 75 targets from Kepler campaigns 1-3 using speckle interferometry on the *Southern Astrophysical Research telescope* and adaptive optics imaging on the *Keck II telescope*. Our target was not found to have exoplanets (Schmitt, 2016).

## INSTRUMENTS USED

The telescopes used for our observations were part of the Las Cumbres Observatory network (Brown, 2013). All ten of these 0.4-meter telescopes have identical specifications. They are located at Siding Spring Observatory in Australia, South African Astronomical Observatory in Sutherland, South Africa, Cerro Tololo Interamerican Observatory in Chile, Teide Observatory in Spain, McDonald Observatory in Texas, United States, and Haleakala Observatory in Hawaii. All have an SBIG STL-6303 camera. A sample telescope is shown in Figure 2. Table 2 gives a count of the number of images of EPIC 201458798 that were returned by each of the telescopes.

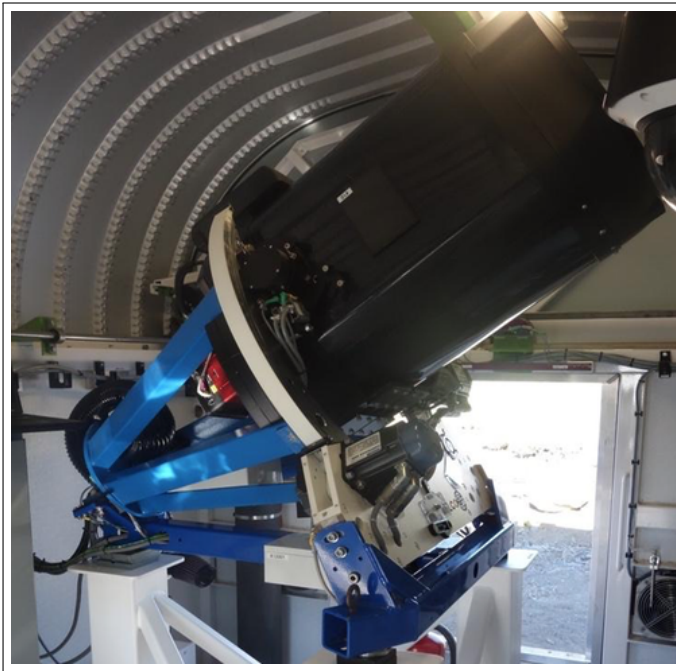
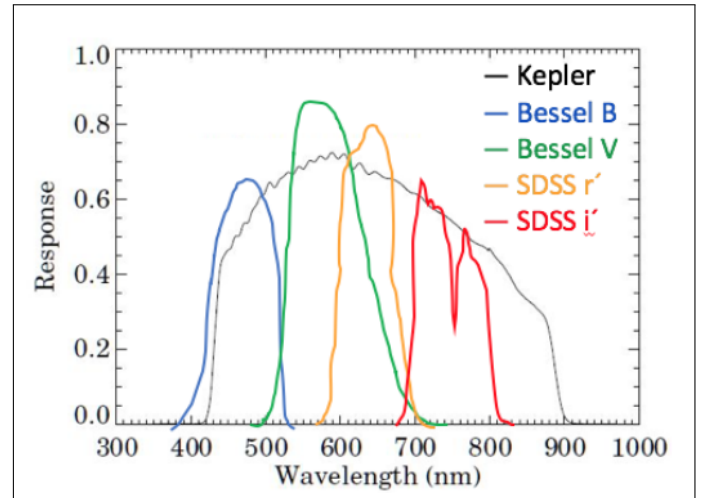
## FILTERS

Our images were taken in the *Bessel B and V*, *Sloan Digital Sky Survey* (SDSS)  $r'$  and  $i'$  filters, corresponding to blue, visible, red, and infrared light. A rough, handdrawn sketch of the bandwidth comparison of

**Table 2.** LCO telescope images of EPIC 201458798

Telescope	Telescope ID	Number of Images
Sliding Spring, New South Wales, Australia	kb97, kb98	324
SAAO, Sutherland, South Africa	kb96	100
Teide Observatory, Tenerife, Spain	kb88, kb99	119
CTIO, Region IV, Chile, Spain	kb26, kb95, kb81	313
McDonald Observatory, Texas, USA	kb80	39
Haleakala Observatory, Maui, USA	kb27, kb82	58
Total		953

these filters to that of Kepler is shown in Figure 3 (Bar-entsen 2018), (Abazajian, 2009), (Giallongo, 2008).

**Fig. 2.** A LCO 0.4m telescope.**Fig. 3.** Photometric response function of Kepler telescope compared to that of the filters used, sketched by hand from images from the references above.

## EXPOSURE TIMES

The optimal exposure time in each filter was determined from test images of the target. Using AstroImageJ software, the ADU counts within an aperture surrounding the target are summed. The average ADU counts per pixel from the surrounding sky in an outer annulus is multiplied by the number of pixels within the target aperture and subtracted from this sum to obtain the AstroImageJ “Source minus Sky” number. Figure 4 shows a zoomed in image of the target in AstroImageJ surrounded by a 6-pixel radius aperture, which is in turn enclosed by the 8-pixel radius outer annulus used for the “Sky” counts. Because

of the 2x2 binning on the images used for this study, each pixel in Figure 4 actually represents 4 pixels worth of ADU counts.

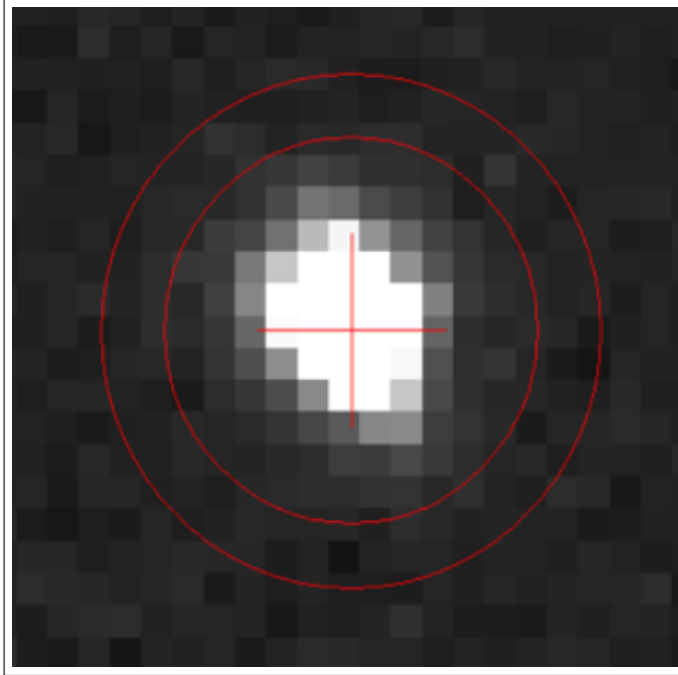


**Fig. 4.** Aperture photometry in AstroImageJ, using a 6-pixel radius target aperture and an outer annulus with an 8-pixel radius.

For a star like that shown in Figure 4, the ideal value of “Source minus Sky” is around 100,000 counts. A value much lower than 50,000 counts is associated with measurements that start to become dominated by noise. A value higher than 500,000 counts risks saturating the CCD camera on the telescope (Fitzgerald, 2018a). Complicating this is the fact that we expect our target star’s brightness to vary (that is exactly what we are trying to measure!), possibly by a factor of 2 or more. Therefore, it is necessary not only for our test images’ counts to be in range, but also double or half of those counts to be in range as well. Our initial 90s-exposure test images for the blue filter had photometry counts that were slightly on the low side (around 70,000 counts), so we increased the exposure time to 150 seconds for that filter. All of the other filters’ test image exposure times were initially in range.

After the images were returned, we flipped through them by hand, scoring them from 0 (bad) to 4 (good) based on their quality. Small streaks (as from cosmic rays) that did not seem to affect the stars’ images significantly earned a score of 3. Slightly oval stars

got a score of 2, and very grainy or otherwise compromised images got a score of 1. Images that were of the wrong starfield, or that were completely clouded over, or that lacked a plate solution due to a World Coordinate System registration failure got a score of 0. In the final analysis, we used stars with scores of 2 or above. This represented a little more than half of the images returned, as shown in Table 3.

**Table 3.** Exposure times and image counts for the filters used.

Filter	Exposure Time (seconds)	Total Images Returned	Images Used
Bessel B	150	226	121
	90	16	10
SDSS i'	45	239	124
SDSS r'	30	235	157
Bessel V	45	237	162

## IMAGE REQUESTS: CADENCE AND JITTER

We initially requested images to be taken with a cadence of approximately every couple of hours. LCO has a robotic scheduling system that recalculates which requests should be filled every 10 minutes based on priority, time sensitivity of the request, telescope availability, and weather (Pickles, 2014). Therefore, we knew that not all of our requests would be filled. EPIC 201458798 is eclipsing over approximately a third of its phase, so we initially set the “jitter” to be high (meaning that we gave the scheduler a broad time window in which to fulfill the request). Towards the end of the project, however, we were requesting images to be taken at specific times with lower jitter to fill in the primary eclipse. For these image requests, we calculated when the next eclipse would occur by taking the image date for the minimum flux in the lightcurve, and adding time in increments of one period until the present day.

## PHOTOMETRY

The OSS pipeline (Fitzgerald, 2018b) performs six types of photometry on images that are returned from LCO: aperture photometry (Laher et al., 2012), source extractor photometry and source extractor kron photometry (Bertin & Arnouts, 2018), and



three types of point-spread function (PSF) photometry known as DAOPhot (Stetson, 1987), DOPhot (Schechter & Mateo, 1993), and PSFEx (Bertin & Arnouts, 2018). Aperture photometry is the simplest of these and is similar to the algorithm that is used by AstroImageJ to obtain the ADU counts referenced above. The photometry types will be referred to as apt, sex, sek, dao, dop, and psf, respectively. Sex is similar to apt, although it uses a different algorithm to undertake the aperture photometry. Sek also uses a similar algorithm except that the star's image is modeled as an ellipse rather than a circle, the size of which is varied to capture 90% of the object's light. The other three photometry types (dao, dop, and psx) report counts not by summing them but instead by fitting the counts for each pixel to various mathematical models of the way in which a star's brightness is expected to vary from pixel to pixel on an image.

The raw data returned by the OSS pipeline consists of text files containing the RA's and Dec's of the star centroids located by each photometry type in each image, along with their associated pixel coordinates, integrated ADU counts, and count errors. To find the counts for our target, we wrote Python code to scan through the RA's and Dec's of the image text files, finding the closest one based on its coordinates. As is evident in Figure 4, the target's light is smeared out over a diameter of about 7 pixels. Since the pixel scale for our images is approximately  $1.16''/\text{pixel}$ , this amounts to about  $8''$ . We identified the target in each image as the star whose computed centroid fell within  $2''$  of its expected coordinates from Table 1. This is comfortably within the image of the star and also corresponds to the amount that the star's apparent coordinates might vary with slight changes in the air's index of refraction due to passing cells of warm or cold air (the "seeing").

## COMPARISON STARS

In addition to the target, it is necessary to observe a few other stars in the same field of view. These are denoted as "comparison stars" or just "comp stars". These stars enable our observation to be calibrated against atmospheric fluctuations and differing exposure times, as they provide a relative measurement of brightness rather than an absolute one. To make this relative measurement, the ratio between the intensity of the target and the comp star is taken. This is equivalent to the difference of the star magnitudes, where magnitude is the logarithm of intensity. However,

this only works if the comp stars are not intrinsically variable themselves.

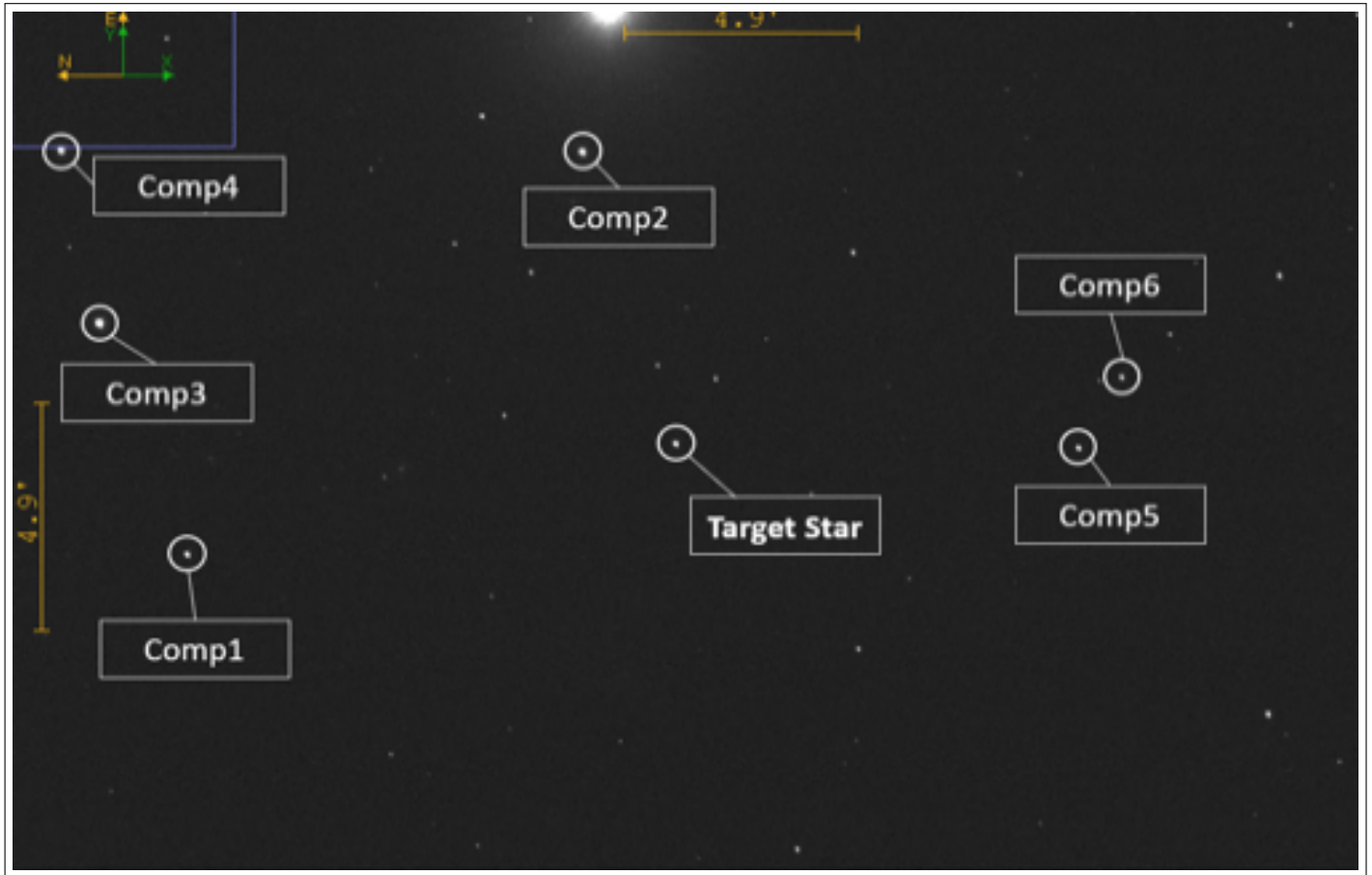
The first criteria for choosing comp stars for EPIC 201458798 was that they needed to be in the  $27.5' \times 18.5'$  field of view surrounding the target. In addition, they had to be roughly the same color as the target star to keep everything as similar as possible. The comp stars also needed to be round in shape. This is a rule of thumb to verify that they are exposed properly and that they are single stars.

Figure 5 shows the star field, with our target star labeled along with six potential comp stars, located by examining a returned LCO image and also inspecting the corresponding starfield in AladinLite software (Boch & Fernique, 2014). The particularly bright star at the top of the image is a cause for concern as it might induce some error in the photon counts for stars nearby. Table 4 shows the coordinates and magnitudes of the stars identified in Figure 5.

## LIGHTCURVE CONSTRUCTION

The visually-identified comp star candidates in Table 4 were used to construct lightcurves of the target star for each of the six photometry types. Due to the short period of the target EB, our observations span several periods. Therefore, plotting the target-minus-comp magnitude versus Julian date results in a visually apparent random scatter of data, as shown at the left in Figure 6. Although it is clear that the images were requested in four separate batches spaced out over a few months, the lightcurve itself is not discernible when plotted versus date. To organize this data, it must be "phased", or plotted as a function of relative phase over the course of a single period. The phase of an observation is equal to the relative Julian date (observation date in days minus initial observation date in days) divided by the Kepler period and modulated by one. For example, if the Julian date of the first observation is 2458600.0 days and the period of the system is 3 days, then an observation taken on 2458601.5 days and an observations taken on 2458604.5 days would both have phase of 0.5. As shown on the right in Figure 6, the target's primary and secondary eclipses become evident when the lightcurve is plotted in this way.

To normalize the lightcurve, the average flux of a region of the graph where the system is not eclipsing is set equal to 1, and all other fluxes are plotted relative to that. For this system, the region of the graph where the system is not eclipsing is taken to be



**Fig. 5.** Star field of EPIC 201458798, taken from one of our images.

**Table 4.** Stars in the field of view of EPIC 201458798.

	Star Identifier	RA HH:MM:SS	Dec Deg:min:sec	Mag B Filter
Target	EPIC 201458798	11:13:07.231	-00:05:33.01	12.8
Comp 1	TYC 263-777-1	11:13:07.231	-00:05:33.01	12.8
Comp 2	UCAC2 31687136 High Proper Motion Star	11:13:32.232	-00:03:37.81	11.841
Comp 3	BD+00 2760	11:13:17.825	+00:06:28.96	10.552
Comp 4	N/A	11:13:32.626	+00:07:15.85	11.18
Comp 5	N/A	11:13:06.703	-00:13:57.27	13.58
Comp 6	N/A	11:13:12.724	-00:14:51.80	12.8

between phase 0.3 and 0.4. On the Kepler Eclipsing Binary Catalog plot of Figure 1, the depth of the primary eclipse is approximately 0.75, but for our data, the depth is closer to 0.65 and even lower for the blue filter (almost as low as 0.6). This likely stems primarily from differences between the filter on the Kepler telescope and the filters used here, whose response curves are sketched above in Figure 3. Also, some of the discrepancy may be due to a different choice of where the system is deemed to be out of eclipse. Finally, the primary eclipse depths can change in different filters due to the stars' unequal temperatures.

## CHOICE OF PHOTOMETRY

Figure 7 shows the same lightcurve with all six types of photometry, using Comp 1 as the comparison star, and using the Kepler period to compute the phase. Based on the cleaner visual appearance of the lightcurve, we decided that sek photometry was most appropriate for images of this system taken with the 0.4m LCO telescopes. However, it is noteworthy that the images used here had 2x2 binning, meaning that the integrated photometry count from sets of four adjacent pixels was reported. This type of binning has the advantages of a faster readout, a higher signal-to-noise ratio, and a smaller image filesize than 1x1 binning, in which the photometry count of each pixel is recorded separately. However, in June of 2018, after this study was concluded, LCO switched to 1x1 binning. The increased spatial resolution of this method may cause different photometry types, particularly those that use PSF methods, to be more appropriate for future studies using the 0.4m LCO telescopes.

## COMPARISON STARS REVISITED WITH AUTOMATED SELECTION

Because they are interdependent, the choice of a comp star and selection of photometry is necessarily a somewhat cyclical process. The procedure described above for choosing provisional comp stars by eye, inspecting the resulting lightcurves, and selecting a photometry type must be followed by a re-examination of the comp stars using that photometry. So, after choosing sek as our photometric method, we wrote code to inspect the stars across all of the images to ensure that we were making the best possible choice of comp star for sek photometry.

For each star in each image, we counted how many sek-processed images contained that same star within 2'' of RA and Dec. The coordinates were computed as those that enabled the star to be identified in the highest number of images. Any non-target star that occurred in more than 75% of the images with photometry counts between 40,000 and 500,000 was deemed as a potential comp. In this field of relatively dim stars, only 5 candidates met these criteria. Three of those were Comp Stars 1, 2, and 5 in the list of visually-identified comps from Table 4. We decided to call the other two automatically-identified stars Comp 7 and Comp 8. They are shown in Figure 8.

To ensure that the comp stars were not themselves variable, all of their differential magnitudes were plotted versus each other. This resulted in 4 comp-versus-comp plots for each of the 5 candidates in 4 filters: a total of 80 plots, where 60 were unique (e.g. Comp1/Comp8 contained the same information as Comp 8/Comp1). Most of these showed flat horizontal lines, as shown in Figure 9.

However, Comp 2 had a slight curve when plotted versus all four other candidates. Although this eliminated it as a potential comp star for this study, its curve may cause Comp 2 to become interesting in its own right. If it is variable, it has an unknown period. To disentangle what if anything might be going on with this star, it would be necessary to continue monitoring it. Also and perhaps significantly, Comp 2 was the closest star to the bright star at the top of the star field.

To determine which of the other comp star candidates to use, we examined the remaining differential magnitude graphs, looking for the flattest lines. It was helpful to arrange the plots as a matrix in order to disentangle the effect of one comp star from that of another. For example, the curve shown for Comp 2 above should not eliminate the comp star against which it was plotted, because this feature showed up for all of the Comp 2 plots. In addition to examining the comp-versus-comp plots visually, we also compared the standard deviations of the differential magnitudes and the slopes from linear fits of each graph, took into account the roundness, color, and average counts from the comp star candidate compared to the target across all of our images, and compared the scatter of the phased lightcurve of the system plotted using sek photometry. So many competing factors made the selection difficult, but in the end, we chose Comp 1 as our comp star.

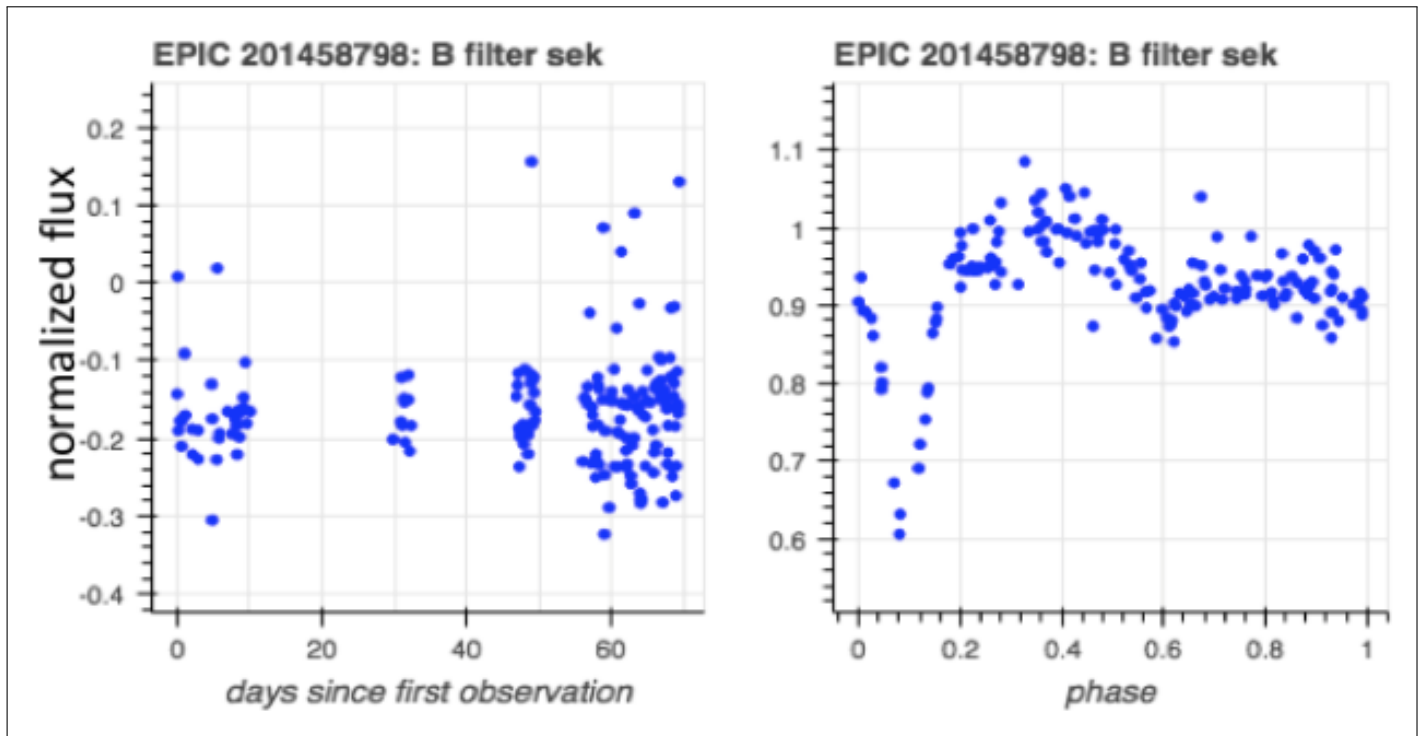


**Fig. 6.** Differential magnitude of EPIC 201458798 in the Bessel B filter as a function of date (left) and as a function of phase (right) using Comp 1, sek photometry, Kepler period.

## CALCULATING THE PERIOD

To independently find the period of our EB, we guessed the period in iterations of one second and constructed the system's lightcurve based on that period. Since the period listed for this system on the Kepler site was 0.6193964 days, we checked periods within 0.4 days of that value. A correct period guess should cause the fluxes to arrange themselves into a recognizable lightcurve, as shown in Figure 10. However, visual examination of thousands of lightcurves generated by incriminating the period guess by one second was impractical and prone to subjectivity. Instead, an automated method was needed to determine which of the guessed periods was correct.

Two different phase dispersion minimization (PDM) algorithms were employed to determine the correctness of each period guess so that the results could be compared for consistency. Both algorithms operate under the assumption that if the guessed period for a system is correct, then two points with similar phase with also have similar flux, putting them relatively close together in flux-phase space. This is visually apparent in Figure 10. Within the tool, as the slider is moved to adjust the period parameter  $p$ , the correctness of any given period can be assessed by how close the fluxes are for points that are adjacent

in phase.

## PDM ALGORITHM 1: MINIMUM DISTANCE METHOD FOR FINDING THE PERIOD

For the distance method, a period is guessed, and the distance between adjacent points on the resulting flux-versus-phase plot is computed using the distance formula. Once all the distances between adjacent points have been determined, these are summed, and the result is stored in a list. Another period is guessed, and the process is repeated. The minimum distance sum will correspond to a flux versus phase plot in which adjacent points are close to each other. For example, the plot on the right of Figure 10 has a smaller distance between adjacent points than the plot on the left. Therefore, we can conclude that the plot on the right's corresponding period is more likely to be the correct period for the system. (Dworetzky, 1983).

This process of guessing periods and computing the distance sums continues until the range of periods within  $\pm 0.4$  days of the Kepler period is exhausted, iterating by 1 second. This range greatly exceeds the period changes typically observed for EBs, which are on the order of seconds per year (Lohr, 2012). Since the Kepler period was computed only four years



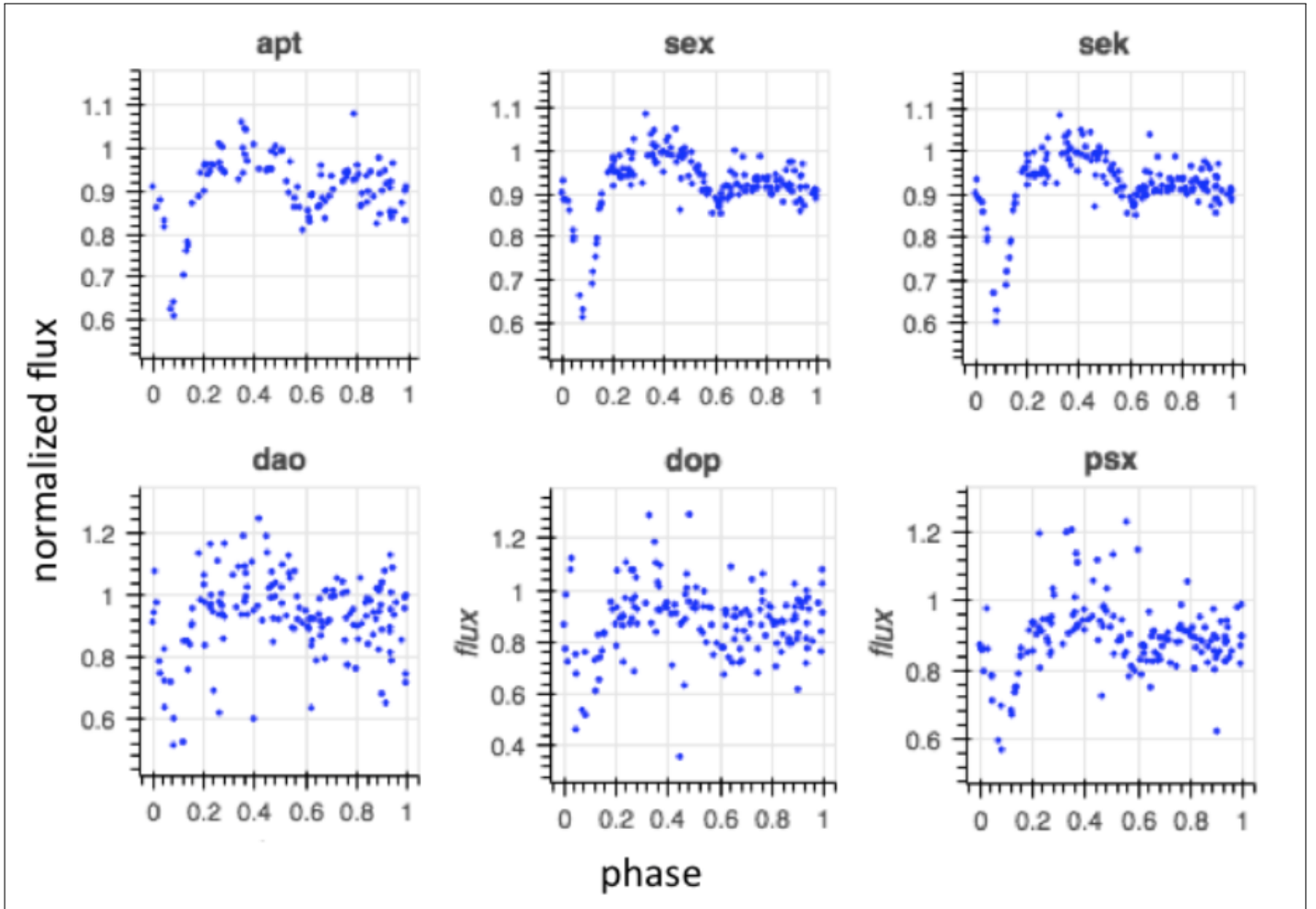


**Fig. 7.** Lightcurve in blue filter with various photometries, using Comp 1 as the comparison star, and using the Kepler period to compute the phase.

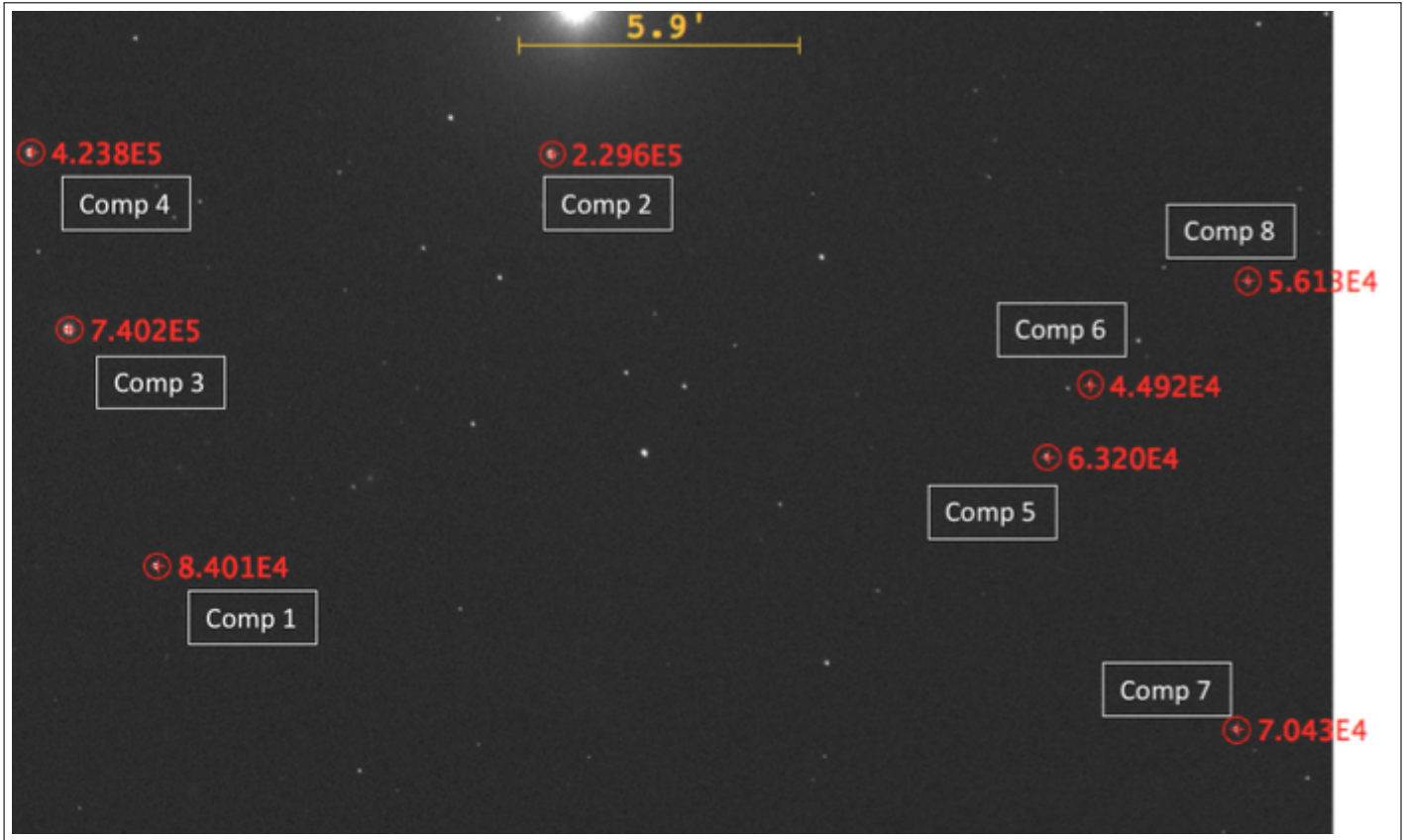


**Fig. 8.** EPIC 201458798 star field including the automatically-identified Comps 7 and 8 at right.

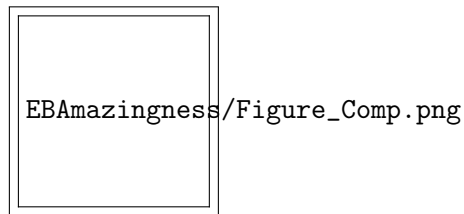


**Fig. 9.** A sample lightcurve for comp stars. All comp lightcurves are shown in the supplemental documents.

before this project, the period is not expected to have changed significantly in the interim.

## PDM ALGORITHM 2: MINIMUM STANDARD DEVIATION METHOD FOR FINDING THE PERIOD

For the standard deviation method, a period is guessed, and the resulting fluxes are sorted into bins based on phase, as shown in Figure 11.

The fluxes with a phase from 0 to 0.1 are in the first bin, 0.1 to 0.2 in the second, 0.2 to 0.3 in the third, and so on. The standard deviation of the fluxes is

taken for each of the bins, the ten standard deviations are summed, and then stored in a list. As before, this process is repeated for every period within  $\pm 0.4$  days of the Kepler period, with increments of 1 second. The period given by this method is the period guess that corresponds to the lowest standard deviation-sum (Stellingwerf, 1978). This is because the lowest sum indicates that the points within the phase bins of the light curves have similar fluxes.

## RESULTS

The best periods found by the algorithms above are shown in Table 5, and the resulting lightcurves are plotted in Figure 12.

## ESTIMATING ERROR

There is no universally accepted way of finding error for these types of algorithms, though many methods have been suggested (Montgomery & Odonoghue, 1999). To obtain the error values shown in Table 5, we used a method suggested by Michael Fitzgerald (Fitzgerald, 2018a). The points of the plot in Figure 13 represent the PDM result, shown on the vertical

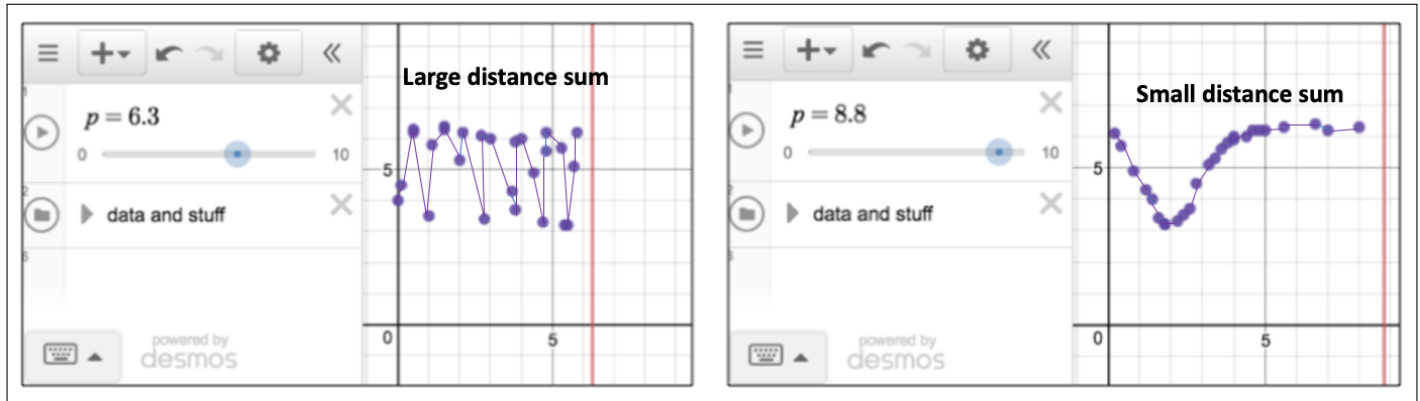


**Fig. 10.** Hensley's [interactive Desmos tool](#) demonstrating a more recognizable lightcurve and a smaller distance sum when fluxes (vertical axis) are plotted versus time over the course of one period for correct ( $p = 8.8$ ) versus incorrect ( $p = 6.3$ ) period ([Hensley, n.d.](#)).

**Table 5.** The best periods found by each algorithm for each filter for EPIC 201458798, compared to the Kepler period of 0.6193964 days (53516 seconds).

Filter	Minimum distance best period (s)	Minimum distance best period difference from Kepler (s)	Error (s)	Minimum standard deviation best period (s)	Minimum standard deviation best period difference from Kepler (s)	Error (s)
Bessel B	53491	-25	$\pm 20$	53516	0	$\pm 20$
Bessel V	53514	-2	$\pm 8$	53475	-41	$\pm 45$
SDSS $r'$	53521	5	$\pm 6$	53517	1	$\pm 12$
SDSS $i'$	53515	-1	$\pm 8$	53518	2	$\pm 10$

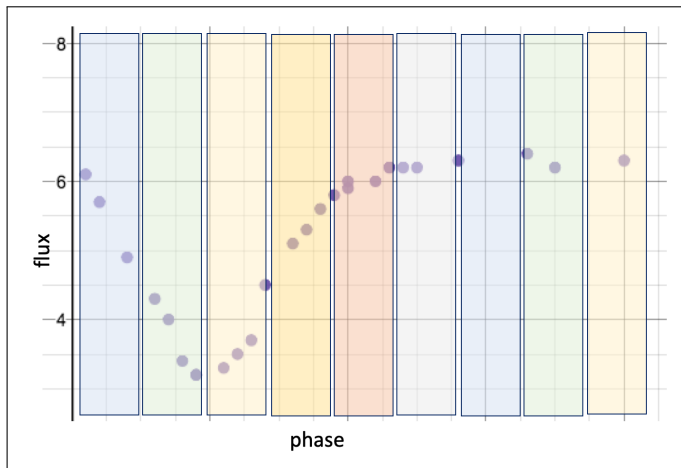


**Fig. 11.** Method for finding the best period from the sum of the standard deviations of the binned fluxes.

axis, as a function of period guess, which is shown on the horizontal axis. The period that corresponds to the lowest point on this plot is the period our algorithm returns. We estimate the error of this period as the width of the curve 5% of the way up from the minimum. This gives an approximation of the amount of scatter surrounding the period found by the algorithm. The error estimates of Table 5 were obtained visually by zooming in on the plot in the region of the minimum. As is evident from the numbers in the table, the period results that were the farthest from Kepler's showed the most evidence of scatter about the minimum and therefore had the highest error. The SDSS  $r'$  and  $i'$  filters had both the lowest error and the closest period results to the period calculated by Kepler.

The four filters and two algorithms used generated 8 PDM plots for sek photometry. As expected, secondary minima were observed at semi-regular intervals from the main minimum. For the red filter distance algorithm, but not for the other filters or for the standard deviation algorithm, the secondary minima occurred with an interesting pattern, shown in Figure 14.

## CONCLUSION

We developed Python code to process time series data from the six types of photometry that are returned by the Our Solar Siblings pipeline, and to automate the search for appropriate comp stars within that data set. We found source extractor kron photometry to be the most appropriate of the six for our magnitude 12 eclipsing binary system imaged with the 0.4m LCO

telescopes. We developed Python code to compute a period for EPIC 201458798 according to two different algorithms. Neither algorithm had a significant deviation from the Kepler period, indicating the period has not changed over the past four years since it was last measured by Kepler.

## ACKNOWLEDGMENTS

This work has made use of data from the European Space Agency (ESA) mission ([Gaia Website](#)), processed by the Gaia Data Processing and Analysis Consortium (DPAC). Funding for the DPAC has been provided by national institutions, in particular the institutions participating in the Gaia Multilateral Agreement.

Special thanks to Michael Fitzgerald of Our Solar Siblings for his inspiration and generous and frequent support throughout this project.

Special thanks to Stanford Online High School for its support of student research and to Gary Oas for his help with LaTeX.

## SUPPLEMENTAL DOCUMENTS

The images used for this analysis are [here](#). The PDM Python code developed for this analysis is [here](#). The comparison star analysis Python code, including all of the comp vs. comp stars plots is [here](#).

## REFERENCES

- Abazajian, K. e. a. (2009). The seventh data release of the sloan digital sky survey. *The Astrophysical Journal Supplement Series*, 182(2).
- Bertin, E., & Arnouts, S. (2018). SExtractor: Software for source extraction. *Astronomy and Astrophysics Supplement Series*, 117(2), 393–404.
- Boch, T., & Fernique, P. (2014, May). Aladin Lite: Embed your Sky in the Browser. In N. Manset & P. Forshay (Eds.), *Astronomical data analysis software and systems xxiii* (Vol. 485, p. 277).
- Brown, T. M. e. a. (2013). Las cumbres observatory global telescope network. *Publications of the Astronomical Society of the Pacific*, 125(931), 1031–1055.
- Dworetzky, M. M. (1983). A period-finding method for sparse randomly space observations or "how long is a piece of string?". *Monthly Notices of the Royal Astronomical Society*, 203(4), 917–924.
- Fitzgerald, M. e. a. (2018a). Our solar siblings. a high school focused robotic telescope-based astron-



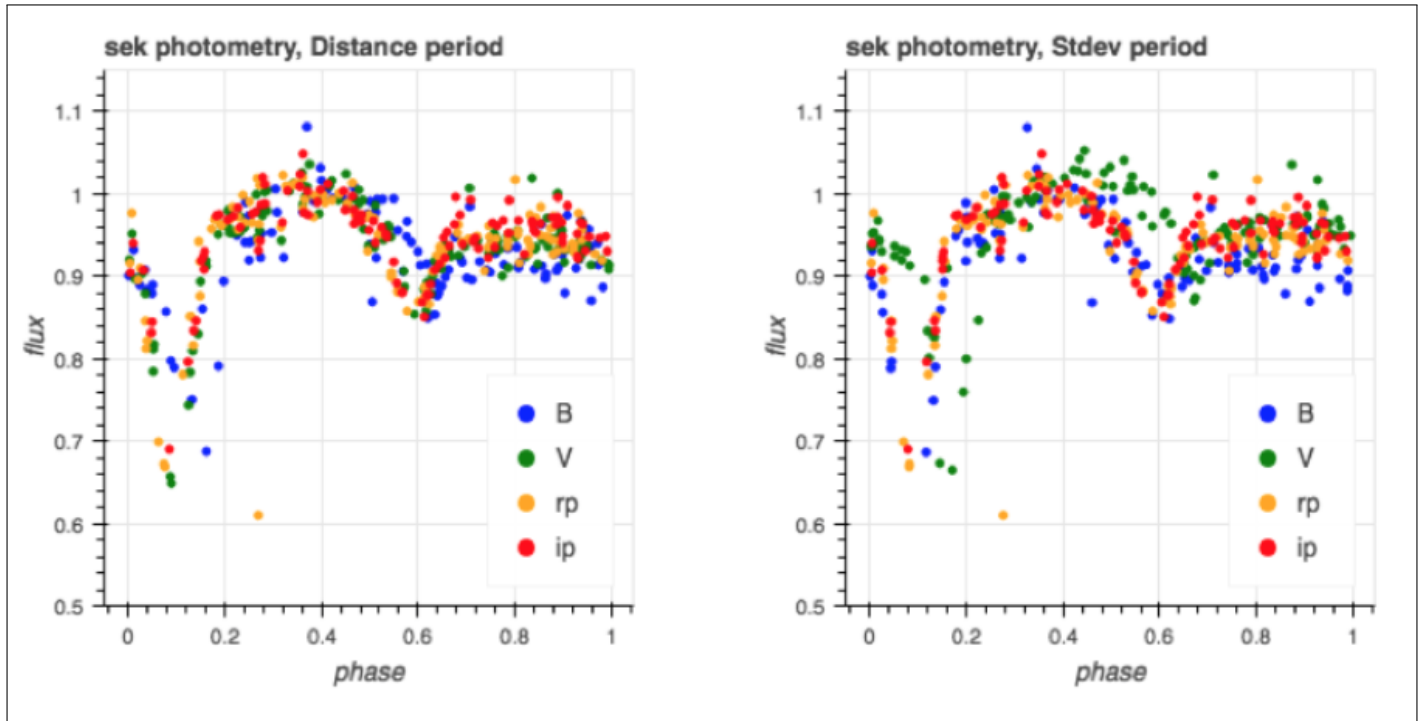


**Fig. 12.** Sek photometry lightcurves constructed from minimum distance method best periods for each filter (left) and minimum standard deviation periods for each filter (right).

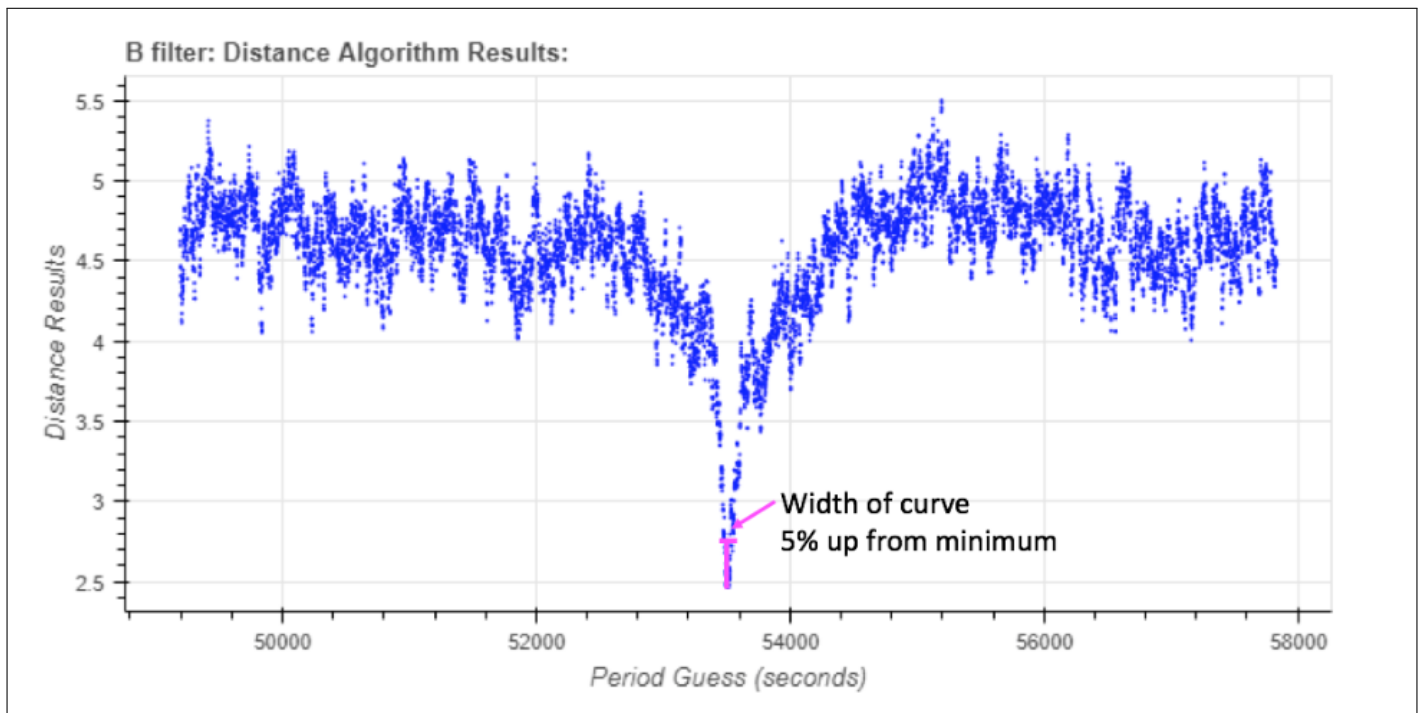


**Fig. 13.** Method for estimating error of PDM algorithms by finding the width of the curve 5% of the way up from its minimum value.

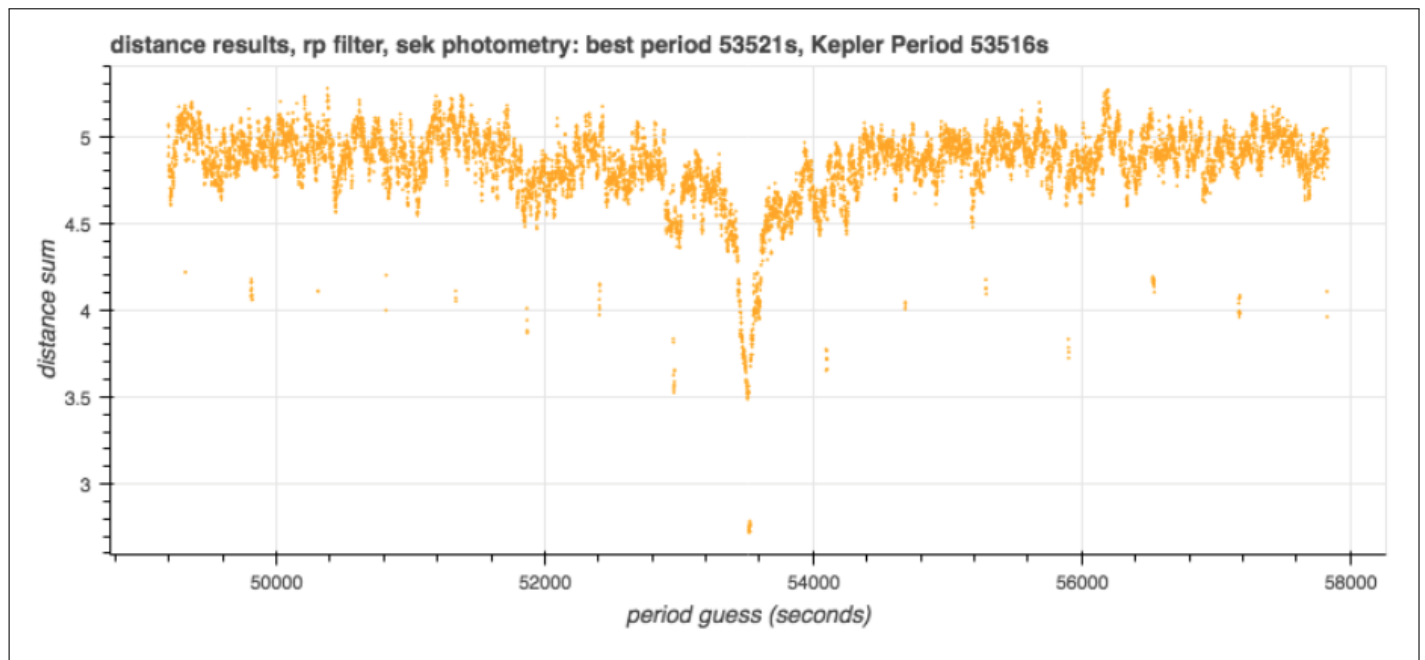


**Fig. 14.** Primary and secondary minima for distance method on SDSS  $r'$  filter images with sek photometry.

omy education project. *Robotic Telescopes, Student Research and Education Proceedings*, 1(1), 221–235.

Fitzgerald, M. e. a. (2018b). The our solar siblings pipeline: Tackling the data issues of the scaling problem for robotic telescope based astronomy education projects. *Robotic Telescope, Student Research and Education Proceedings*, 1(1), 347–358.

Giallongo, E. e. a. (2008). The performance of the blue prime focus large binocular camera at the large binocular telescope. *Astronomy and Astrophysics*, 482(1), 349–357.

Hensley, H. (n.d.). *Period finder simulation*. Retrieved from <https://www.desmos.com/calculator/o3thrlvlg>

Kirk, B. e. a. (2016). Kelper eclipsing binary stars. vii. the catalog of eclipsing binaries found in the entire kepler data set. *The Astrophysical Journal*, 151(3), 22.

Laher, R., Gorjian, V., Rebull, L., J. Masci, F., Fowler, J., Helou, G., ... Law, N. (2012, 07). Aperture photometry tool. *Publications of the Astronomical Society of the Pacific*.

Lohr, M. e. a. (2012). Period decrease in three superwasp eclipsing binary candidates near the short period limit. *Astronomy and Astrophysics*, 542.

Matijevic, G. e. a. (2012). Kepler eclipsing binary stars. iii. classification of kepler eclipsing binary

light curves with locally linear embedding. *The Astronomical Journal*, 143(5), 1–6.

Montgomery, M. H., & Odonoghue, D. (1999). A derivation of the errors for least squares fitting to time series data. *Delta Scuti Star Newsletter*, 13, 28–32.

Pickles, A. e. a. (2014). *Lcogt network observatory operations* (Vol. 9149). Retrieved from <https://doi.org/10.1117/12.2055215>

Rozmus, D. (2010). Eclipsing binary stars. *Seminar Files, 2010 - 2011*(1), 1–13.

Schechter, P., & Mateo, M. (1993). Dophot, a ccd photometry program: Description and tests. *Publications of the Astronomical Society of the Pacific*, 105, 1342–1353.

Schmitt, J. e. a. (2016). Planet hunters. x. searching for nearby neighbors of 75 planet and eclipsing binary candidates from the k2 kepler extended mission. *The Astronomical Journal*, 151–159.

Southworth, J. (2012). Eclipsing binary stars: The royal road to stellar astrophysics. In D. H. F. Arenou (Ed.), (Vol. Proceedings of the workshop 'Orbital Couples: Pas de Deux in the Solar System and the Milky Way' (Paris 2012), pp. 51–58).

Stellingwerf, R. F. (1978). Period determination using phase dispersion minimization. *The Astrophysical Journal*, 224, 953–960.

Stetson, P. (1987). Daophot: A computer program for

crowded-field stellar photometry. *Publications of the Astronomical Society of the Pacific*, 99, 191–222.

# New distance estimates to RX Eri, an RR Lyrae star in Eridanis, using near infrared photometry

TIMOTHY JONES<sup>1,\*</sup>

<sup>1</sup>Alfred Deakin High School, ACT Education Department

\*Corresponding author: [timdjones7@gmail.com](mailto:timdjones7@gmail.com)

This paper presents the results of analysis of the RRab type star, RX Eri, building on previous work to include light curves further into the infrared. This project has yielded light curve results which have determined the period to  $0.587 \pm 0.005$ d, agreeing with prior research. The distance estimation using Period-Luminosity-Metallicity relationships, V:  $612 \pm 27$ pc, i:  $608 \pm 21$ pc, z:  $613 \pm 23$ pc broadly agreed with Gaia DR2's estimation of  $605 \pm 11$ pc. These infrared filters yielded better estimations in terms of error than those in the V band, although they all fall within the margins of error of the measurements made.

© 2020 Astronomy Theory, Observations and Methods Journal

**Keywords:** Stars: Variable: RR Lyrae, techniques: photometric, catalogs, parallaxes

<https://doi.org/10.32374/atom.2020.1.2>

## INTRODUCTION

RR Lyrae stars are used as tools to determine the distance to star clusters in our galaxy which is made possible by photometric analysis of their light curves in a range of frequencies. This paper presents the results of one such analysis of the star, RX Eri, building on previous work to include light curves further into the Infra red. The use of RR Lyrae variable stars as standard candles for the measurement of distances and ages of globular clusters will be improved if the error can be reduced by using filters in the near infrared (Caceres & Catelan, 2008).

Catelan et al (2004) demonstrated that more reliable distance calculations are possible when analysing RR Lyrae stars in the near infrared compared to traditional optical observations. This analysis showed that the Period-Luminosity relationship becomes more linear and tighter as the light frequency moves towards

the near infrared (V band  $r = 0.19$ , K band  $r = 0.9990$ ) (Catelan, Pritzl, & Smith, 2004). This relationship has been shown to best suit the accurate determination of distance using absolute magnitudes and most suited to modelling the Period-Luminosity relationship in RR Lyrae stars (Caceres & Catelan, 2008).

Observations of RX Eri demonstrate a reliable measurement of its period and class (RRab) across many authors (Carrillo et al., 1995; Kovacs, 2005; Neeley et al., 2017; Andrievsky et al., 2017; Siegel, 1982). A summary of RX Eri data is presented in table 1.

Metallicity measurements however are in stark contrast and this represents a challenge to this study. As Table 2 shows, there has been a large amount of variability in the measurement of metallicity which is difficult to critique without detailed analysis of the various methods used. In the absence of this information the calculations used for this paper, the value determined by (Neeley et al., 2017) was selected as



**Table 1. RX Eri General Properties**

Type	Value	Source
ICRS	Ra 4 49 44.29	(Gaia et al., 2018)
Coordinates	Dec -15 44 31.8	
Period	0.587246d	(Carrillo et al., 1995)
	0.587247d	(Kovacs, 2005)
	0.587242d	(Neeley et al., 2017)
Teff	6178K	(Andrievsky et al., 2017)
	6300K	(Siegel, 1982)
Radial Velocity	80Km/s-1	(Andrievsky et al., 2017)
Spectral Type	F2D	(Gaia et al., 2018)
Mv	0.41	(Siegel, 1982)
	0.66	(Fernley, Carney, Skillen, Cacciari, & Janes, 1998)
	0.54	(Woolley & Dean, 1976)
Vmag	9.72	(Kovacs, 2005)
	9.70	(Carrillo et al., 1995)
	9.69	(Muraveva et al., 2015)
O/Fe	0.52	(Andrievsky et al., 2017)
Na/Fe	-0.37	(Andrievsky et al., 2017)

it represented the measurement most related to the time the photometric measurements were made and is also a mode value of the data presented.

**Table 2. Measurement of Metallicity of Rx Eri from past studies**

Fe/H	Source
-1.07	Kovacs 2005
-1.18	Andrievsky et al 2017
-1.32	Butler 1975
-1.63	Fernley et al 1997
-1.33	Neeley et al 2018
-1.98	Muraveva 2015
-1.4	Skillen et al 1992

## METHODS

### Observations

The data upon which this project is based was gathered using the Las Cumbres Observatory (LCO) 0.4m SBIG telescopes at Siding Springs, (Australia), Sutherland (South Africa), Cerra Tololo (Chile), Haleakala (Maui) and Teide (Spain). This experiment is dependant in the systems described in detail in Brown et al 2013 (Brown et al., 2013). The observational data, consisting of sets of B, V, i and z optical images was collected during a cadence of at least 70 observation opportunities as part of the Our Solar Siblings (Fitzgerald et al., 2018) proposal between February and April 2019.

Data gathered by the LCO telescope network was optimised to ensure that the images produced met the data collection needs but did not risk over-exposure, avoiding an unquantifiable error in the photometric measurements made. These optimal times were determined using AstroImageJ software (AstroimageJ) to count the pixels within an aperture and compare these to the sky background. In this manner the data collected represented the radiation created by only the target star. Optimal times for each band were determined to be 3 seconds for the i band, 12 seconds for z. 4 seconds for V and 13 seconds for B which represented  $\approx 100000$  counts for RX Eri.

### Photometry

The images and photometry were processed using the Our SolarSiblings pipeline (Fitzgerald, 2018). The SEK (Source Extractor Kron) files were found to produce the least variable photometry data and thus this method was used (Bertin & Arnouts, 1996). This data was then further processed by astrosource (Astrosources). Astrosources identifies the most optimal stars in the image with the lowest variability to use as comparison star for each of the B, V, i and z filters used in this study. Astrosources analysis identified 6 standard stars, shown in Figure 1, with variability between 0.01-0.03 that were used as comparison sources. The known magnitudes are from APASS (Henden et al., 2016) for B and V and from Skymapper (Onken et al., 2019) for i and z. The comparison stars are listed in Table 3. These stars allowed the extraction of a calibrated lightcurve in each of these filters using differential photometry.

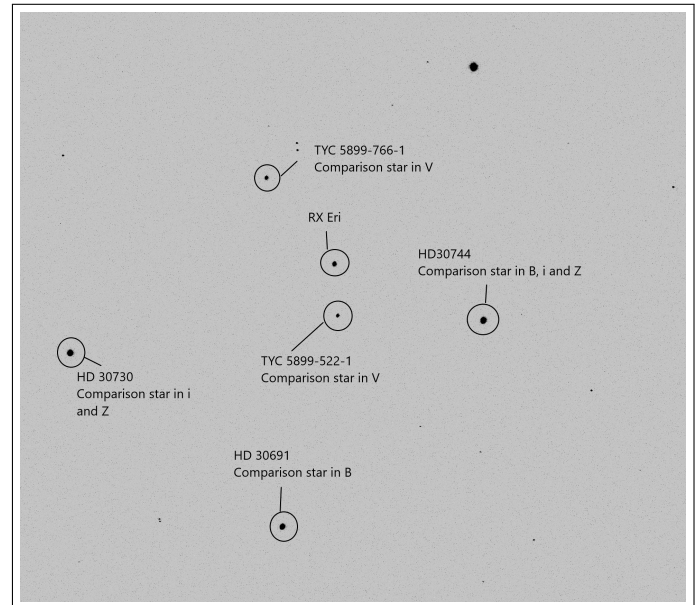


**Fig. 1.** Inverted image of the analysed starfield. Image taken with SBIG 0.4m telescope operated by Las Cumbres Observatory

The final lightcurves were identified using the Phase Dispersion Method, coded by (Altunin, Caputo, & Tock, 2020) to determine a period likelihood plot (see Figure 3) and folded on the determined period as shown below in figures 2-5.

In this paper we investigated the photometric properties of RX Eri using the robotic telescopes of the Las Cumbres Observatory network. Filter bands B,V, i, and z were captured using the 0.4m SBIG tele-

**Table 3. Calibration Stars Used**

RA	Dec	Filter	Var	Mag
72.30953	-15.7178	B	0.013	9.25
72.40799	-15.8093	B	0.030	8.77
		i	0.012	7.90
		z	0.014	8.16
72.39154	-15.6205	i	0.012	8.16
72.40968	-15.7428	V	0.017	10.99
72.47515	-15.7098	V	0.023	10.64
72.39157	-15.6205	z	0.010	8.24

scopes of this network, allowing determination of light curves and an estimation of the distance to RX Eri.

## RESULTS

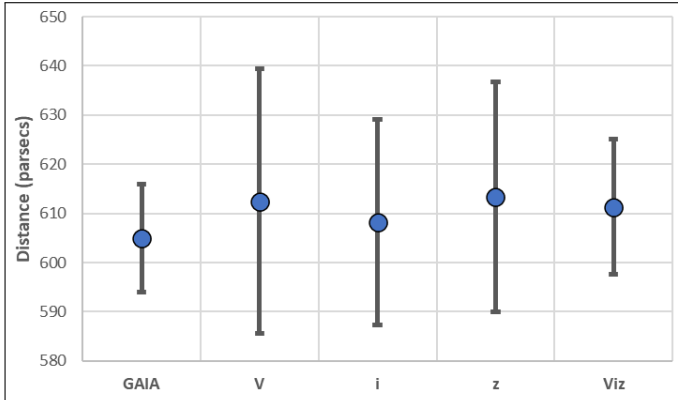


**Fig. 2.** Visual comparison of distance results from this study compared to GAIA

Distance estimation equations rely on the complex interactions of the chemical compositions of RR Lyrae stars as well as their period of flux and luminosity. Following the derived equations of (Bertelli, Bressan, Chiosi, Fagotto, & Nasi, 1994) which account for the chemical composition of the target star in its estimation of  $\log(Z)$ . The equation;  $\log(Z) = 0.977Fe/H - 1.699$  was used to determine the  $\log(Z)$  value for use in the distance calculations. Following this calculation the value was incorporated into the equations of period-luminosity-metallicity (Catelan et al., 2004; Caceres & Catelan, 2008) used to determine the absolute magnitude and, hence, the distance

to RX Eri as estimated by each band:

$$Mv = 2.288 + 0.882\log Z + 0.108(\log Z)^2 \quad (1)$$

$$Mi = 0.908 - 1.035\log P + 0.220\log Z \quad (2)$$

$$Mz = 0.839 - 1.295\log P + 0.211\log Z \quad (3)$$

Incorporating the distance modulus  $m_M = 5\log d - 5$  the distance (d) was determined for each band analysed. The interstellar reddening,  $E(B - V) \approx 0.011$  was estimated by minimising the variance in the distance across the three filters used. This value was reasonable given the maximum reddening in this direction of  $E(B - V) \approx 0.05$  (Schlafly & Finkbeiner, 2011). Distance errors were incorporated the errors in magnitude, period, metallicity.

The distance estimations using Period-Luminosity-Metallicity relationships broadly agreed with Gaia DR2's (Gaia et al., 2018) estimation of  $605 \pm 11$  pc. The distances are presented in Table 4 and shown visually in Figure 2. The combined estimate of the distance using all three of the V, i and z PLM estimates is  $611 \pm 14$  pc.

**Table 4. Distance Calculations**

Filter	m	M	Distance	Error
		(pc)	(pc)	
B	10.148±0.015			
V	10.104±0.021	0.604	612	27
i	9.422±0.015	0.476	608	21
z	9.452±0.014	0.497	613	23

Light curves were obtained in each filter which show a clear adherence to an RRab magnitude variation pattern. Comparing the V band results gained to AAVSO data (see figure 8) it is clear to see that the data gained for this study compares well to that of other observers.

## CONCLUSION

This research has determined the period of RR Lyrae variable star, RX Eri to be 0.587 days, supporting the research of several other groups (e.g (Carrillo et al., 1995; Kovacs, 2005; Neeley et al., 2017)). V band light curves comparable to past research have been generated and new observations in the near infrared range (bands i and z) have been presented. The

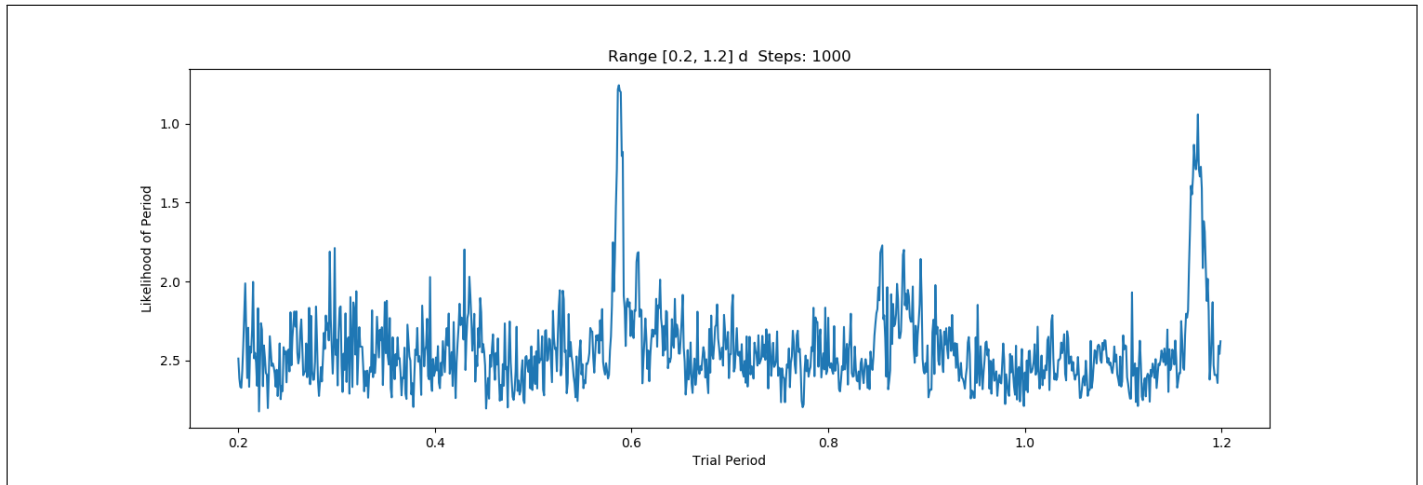


**Fig. 3.** PDM Likelihood plot in i band

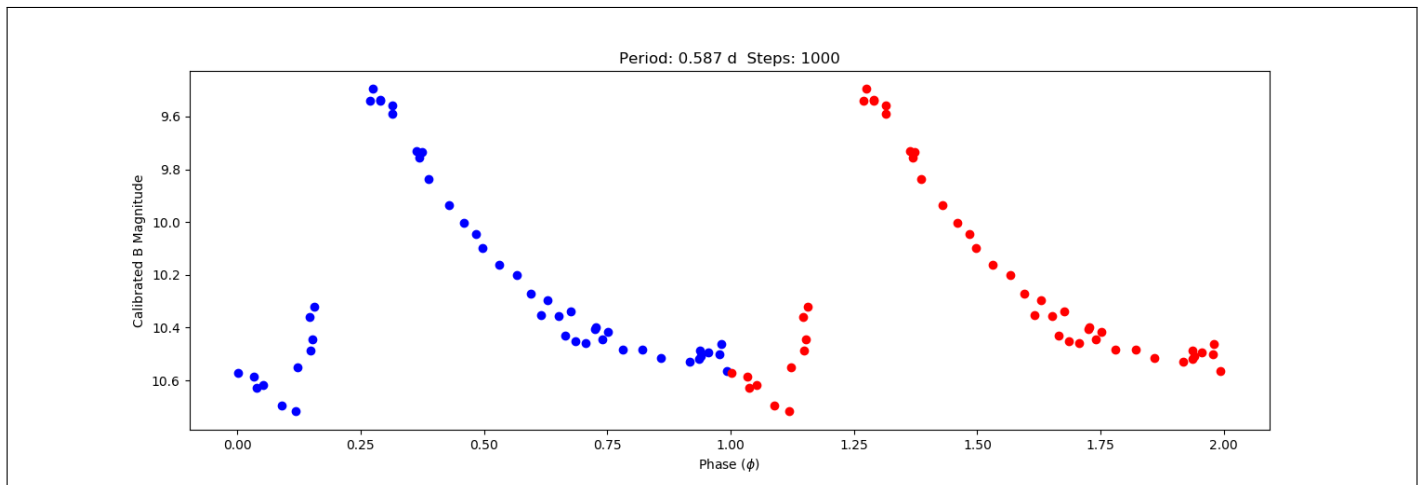


**Fig. 4.** Light curve in B (890 Angstroms)

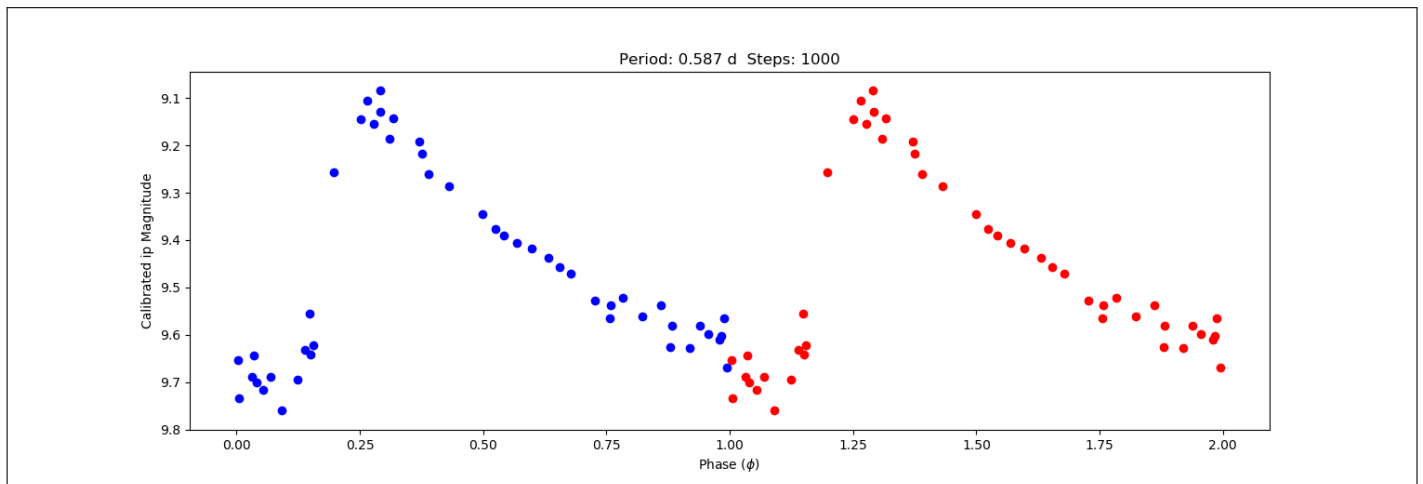


**Fig. 5.** Light curve in i (1290 Angstroms)



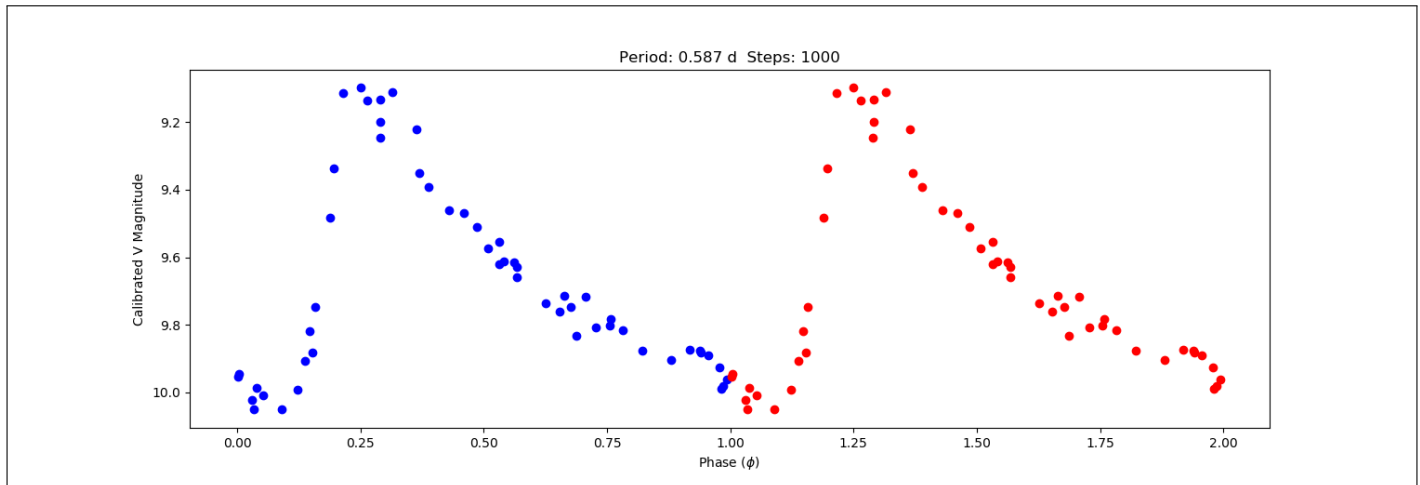


**Fig. 6.** Light Curve in V (840 Angstroms)

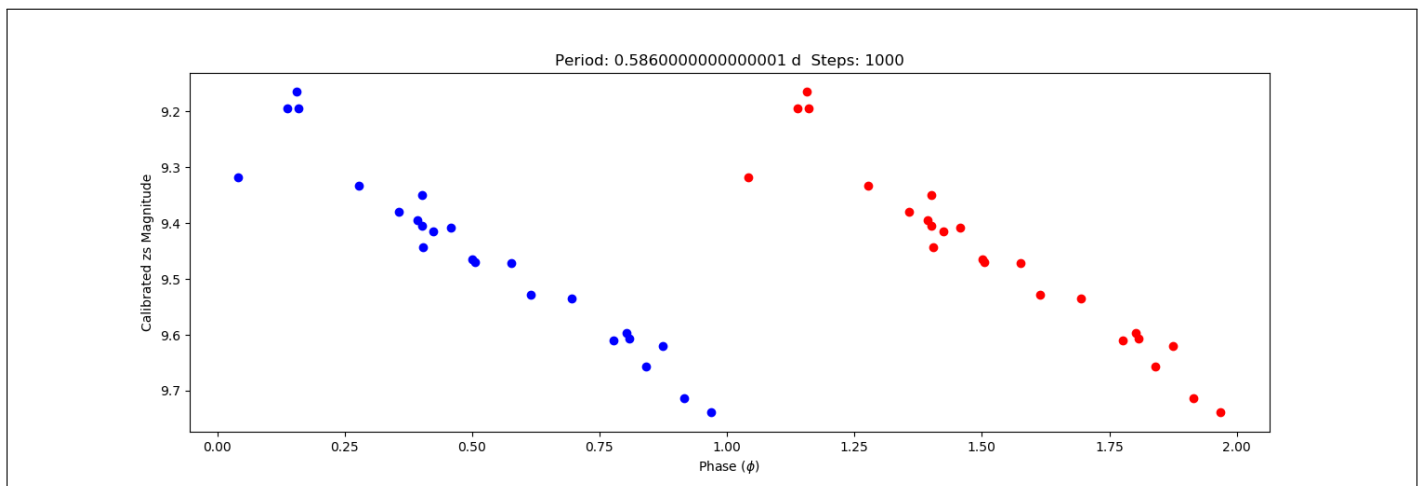


**Fig. 7.** Light Curve in z (1040 Angstroms)

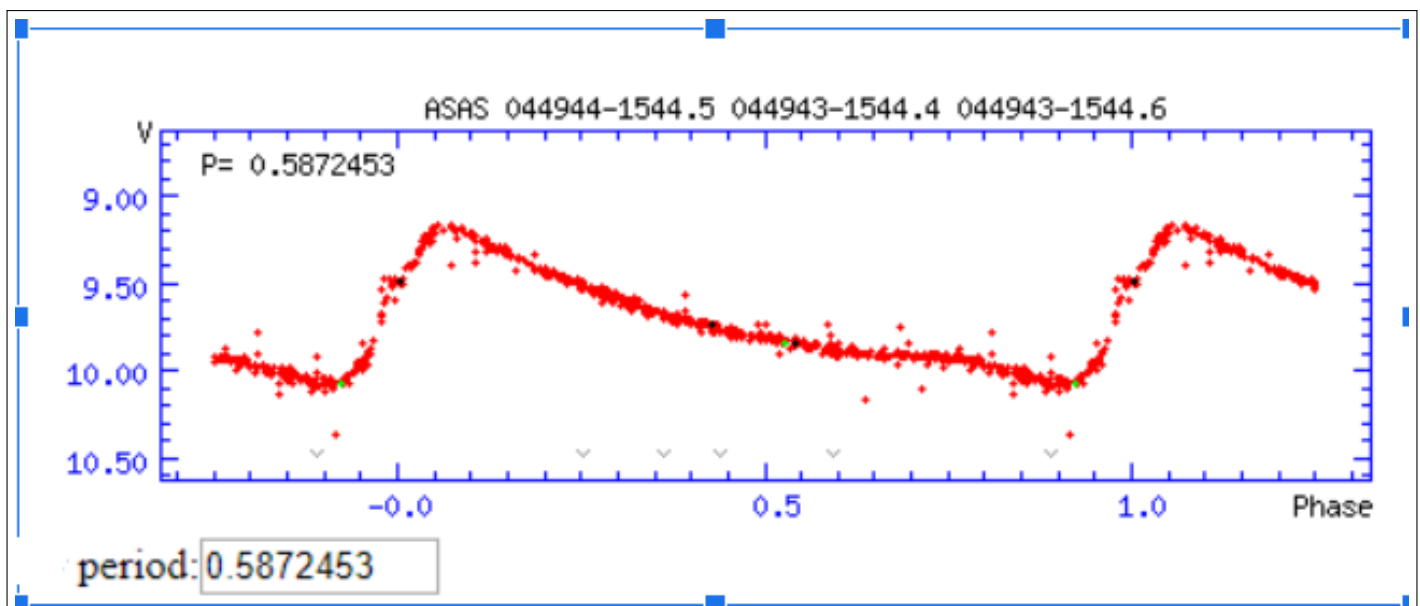


**Fig. 8.** Comparable V band data from AAVSO. After AAVSO 2005-19 accessed at [AAVSO](https://www.aavso.org/) on 31.10.19

distance estimations, V:  $612 \pm 27$ pc, i:  $608 \pm 21$ pc, z:  $613 \pm 23$ pc. and Viz:  $611 \pm 14$ pc. using the Period-Metallicity-Luminosity relationships all agreed within the errors with Gaia DR2's estimation of  $605 \pm 11$ pc.

## ACKNOWLEDGMENTS

I would like to thank the continued support of the Our Solar Siblings staff, in particular Michael Fitzgerald, Alfred Deakin High School and the ACT Education Directorate for their support with this project. This work makes use of observations from the Las Cumbres Observatory Global Telescope Network without which the observations would not be possible. This research has made use of the International Variable Star Index (VSX) database, operated at AAVSO, Cambridge, Massachusetts, USA.

## REFERENCES

- Altunin, I., Caputo, R., & Tock, K. (2020). Period of eclipsing binary epic 201458798. *Astronomy Theory, Observations and Methods*, 1(1).
- Andrievsky, S., Wallerstein, G., Korotin, S., Lyashko, D., Kovtyukh, V., Tsymbal, V., ... Farrell, E. (2017). The relationship of sodium and oxygen in galactic field rr lyrae stars. *Publications of the Astronomical Society of the Pacific*, 130(984), 024201.
- Bertelli, G., Bressan, A., Chiosi, C., Fagotto, F., & Nasi, E. (1994). Theoretical isochrones from models with new radiative opacities. *Astronomy and Astrophysics Supplement Series*, 106, 275–302.
- Bertin, E., & Arnouts, S. (1996). SExtractor: Software for source extraction. *Astronomy and Astrophysics Supplement Series*, 117(2), 393–404.
- Brown, T., Baliber, N., Bianco, F., Bowman, M., Burleson, B., Conway, P., ... others (2013). Las cumbres observatory global telescope network. *Publications of the Astronomical Society of the Pacific*, 125(931), 1031.
- Caceres, C., & Catelan, M. (2008). The period-luminosity relation of rr lyrae stars in the sdss photometric system. *The Astrophysical Journal Supplement Series*, 179(1), 242.
- Carrillo, D., Burki, G., Mayor, M., Burnet, M., Lampens, P., & Nicolet, B. (1995). VizieR online data catalog: Photometric and radial velocity of rrlr stars (carrillo+ 1995). *VizieR Online Data Catalog*, 411.
- Catelan, M., Pritzl, B. J., & Smith, H. A. (2004). The rr lyrae period-luminosity relation. i. the theoretical calibration. *The Astrophysical Journal Supplement Series*, 154(2), 633.
- Fernley, J., Carney, B., Skillen, I., Cacciari, C., & Janes, K. (1998). The slope of the rr lyrae mv-[fe/h] relation. *Monthly Notices of the Royal Astronomical Society*, 293(3), L61–L64.
- Fitzgerald, M. T. (2018). The our solar siblings pipeline: Tackling the data issues of the scaling problem for robotic telescope based astronomy education projects. *RTSRE*, 1(1), 347–358.
- Fitzgerald, M. T., McKinnon, D. H., Danaia, L., Cutts, R., Salimpour, S., & Sacchi, M. (2018). Our solar siblings. a high school focussed robotic telescope-based astronomy education project. *RTSRE*, 1(1), 221–235.
- Gaia, C., Brown, A., Vallenari, A., Prusti, T., de Bruijne, J., Babusiaux, C., ... others (2018). Gaia data release 2 summary of the contents and survey properties. *Astronomy & Astrophysics*, 616(1).
- Henden, A. A., Templeton, M., Terrell, D., Smith, T., Levine, S., & Welch, D. (2016). VizieR online data catalog: Aavso photometric all sky survey (apass) dr9 (henden+, 2016). *yCat*, II–336.
- Kovacs, G. (2005). Iron abundances derived from rr lyrae light curves and low-dispersion spectroscopy. *Astronomy & Astrophysics*, 438(1), 227–238.
- Muraveva, T., Palmer, M., Clementini, G., Luri, X., Cioni, M.-R., Moretti, M. I., ... Rubele, S. (2015). New near-infrared period–luminosity–metallicity relations for rr lyrae stars and the outlook for gaia. *The Astrophysical Journal*, 807(2), 127.
- Neeley, J. R., Marengo, M., Bono, G., Braga, V. F., Dall’Ora, M., Magurno, D., ... others (2017). On a new theoretical framework for rr lyrae stars. ii. mid-infrared period–luminosity–metallicity relations. *The Astrophysical Journal*, 841(2), 84.
- Onken, C. A., Wolf, C., Bessell, M. S., Chang, S.-W., Da Costa, G. S., Luvaul, L. C., ... Shao, L. (2019). Skymapper southern survey: Second data release (dr2). *Publications of the Astronomical Society of Australia*, 36.
- Schlafly, E. F., & Finkbeiner, D. P. (2011). Measuring reddening with sloan digital sky survey stellar spectra and recalibrating sfid. *The Astrophysical Journal*, 737(2), 103.
- Siegel, M. J. (1982). A wbyb photometric study of

rr lyr stars. i. *Publications of the Astronomical Society of the Pacific*, 94(557), 122.

Woolley, R., & Dean, J. (1976). The radius of rx eridani. *Monthly Notices of the Royal Astronomical Society*, 177(1), 247–255.

# An Automated Approach to Modeling Jupiter's Synchrotron Radiation from Radio Telescope Observations

PEYTON ROBERTSON<sup>1</sup>, CONNOR ESPENSHADE<sup>1</sup>, JAY SARVA<sup>1</sup>, OWEN DUGAN<sup>1</sup>, AND KALÉE TOCK<sup>1</sup>

<sup>1</sup>Stanford Online High School, CA

\*Corresponding author: peytonwr@stanford.edu

---

In this study, we used 2.295 GHz radio telescope data to study synchrotron radiation from Jupiter's magnetosphere. We processed scans of Jupiter and calibrators taken by the Goldstone Apple Valley Radio Telescope on various dates, developing and automating algorithms for outlier removal, baseline subtraction, and Gaussian fitting in order to determine the peak intensity of each scan. Comparing the peak intensities of Jupiter to those of the calibrators and the known fluxes of the calibrators, we computed the flux of Jupiter on each scan. Plotting Jupiter's flux against the longitude facing Earth at the time of each scan revealed a periodic relationship between the variables and thus a model for expected synchrotron flux from Jupiter observed at a given longitude. This estimate can corroborate other flux measurements of Jupiter at similar frequencies, such as those taken by the microwave radiometer on the Juno probe.

© 2020 Astronomy Theory, Observations and Methods Journal

**Keywords:** *Physical data and processes: magnetic fields — Astronomical databases: catalogs*

<https://doi.org/10.32374/atom.2020.1.3>

---

## INTRODUCTION

On August 5, 2011, NASA launched Juno, a satellite headed for Jupiter to measure key data and answer questions about the the gas giant. The spacecraft's ability to get within close proximity of Jupiter provided the opportunity to acquire unprecedented data, elucidating its atmospheric composition (including the amount of water in its atmosphere), its magnetic and gravitational fields, and the history of its formation. But many of these measurements must take into account the synchrotron radiation due to Jupiter's

strong magnetic field and radiation belt (Kollmann, 2017).

In this paper, we investigate how Jupiter's synchrotron radiation varies with the geometry of an observer. Using Earth-based telescopes, we can study the intensity variation as a function of Jupiter's Central Meridian Longitude (CML). This model can then enable more accurate measurements of other radiation (such as those taken by Juno) and the molecules that attenuate it. For example, the microwave and radio intensity of Jupiter is largely attenuated by the

presence of water and, to a smaller extent, ammonia. Understanding the degree to which the core's thermal radiation is attenuated by these molecules may provide a means of more accurately estimating their concentrations beneath the cloud tops, which could then give clues about the composition and formation of Jupiter's core. Since synchrotron flux is intermingled with the core's thermal radiation, our separate measurement of it provides a means of disentangling its effect.

Understanding how much these molecules attenuate the thermal radiation from the core may provide a greater understanding of how much water and ammonia exists under the cloud tops, which could then give clues about the composition and formation of Jupiter's core.

For Earth-based observations of Jupiter's synchrotron radiation, we used data from the Goldstone Apple Valley Radio Telescope (GAVRT) (Figure 1). The dataset, initially received from Dr. Thangasamy Velusamy, and later queried directly from databases at the Lewis Science Center, contains data from telescope scans of Jupiter, as well as scans of calibrators taken on the same days. These data allow one to compare the telescope offset (varying linearly with time as the telescope sweeps past the target) with the temperature of the antenna (indicating intensity of the signal) during each scan.



**Fig. 1.** The Goldstone Apple Valley Radio Telescope (GAVRT) (*Goldstone Apple Valley Radio Telescope (GAVRT)*, n.d.).

## SYNCHROTRON RADIATION

Synchrotron radiation is the result of electrically charged particles following a curved path at relativistic

velocities (Nave, n.d.). Synchrotron radiation is highly beamed along the forward direction of particle movement.

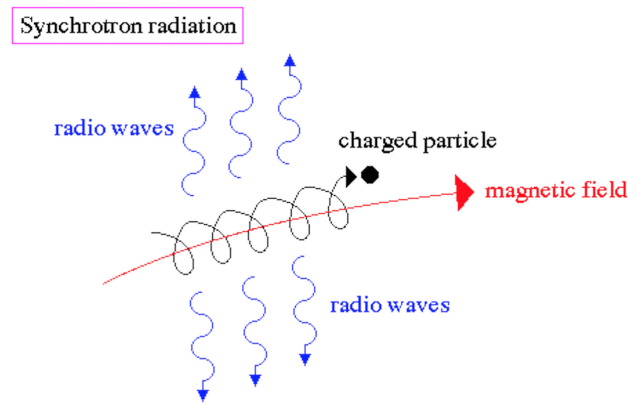


**Fig. 2.** Diagram showing synchrotron emission emitted by electron in the direction of its motion while spiraling around Jupiter's magnetic field lines.

Jupiter has a strong magnetosphere, or magnetic field, which is thought to be produced by metallic hydrogen in its core (Greicius, 2018). Jupiter's high pressure effectively condenses hydrogen gas into a molten flow of elementary particles. The electrons in this flow are accelerated to relativistic speeds as they spiral around Jupiter's magnetic field lines due to Jupiter's magnetosphere (Figure 2). Most spiraling electrons lie in Jupiter's central radiation belt, which is tilted relative to the ecliptic. While spiraling around magnetic field lines in the radiation belt, electrons emit synchrotron radiation in the plane of the belt. The orientation of this plane relative to Earth determines if the radiation is observed by Earth-based telescopes, as demonstrated in Figure 3.

As Jupiter rotates (with a period of approximately 9 hours, 56 minutes), an observer from Earth faces not only different longitudes, but also different parts of its radiation belt. When looking directly at the central radiation belt, synchrotron radiation is expected to increase; when looking above or below it, synchrotron radiation is expected to decrease. Due to this wobble effect, we expect to see two minima (a sighting above and below the central radiation belt) and two maxima (two sightings at the radiation belt) each period. The "beaming curve" is a measure of flux as a function of CML; that is, how much radiation is received during scans of Jupiter as the planet rotates.



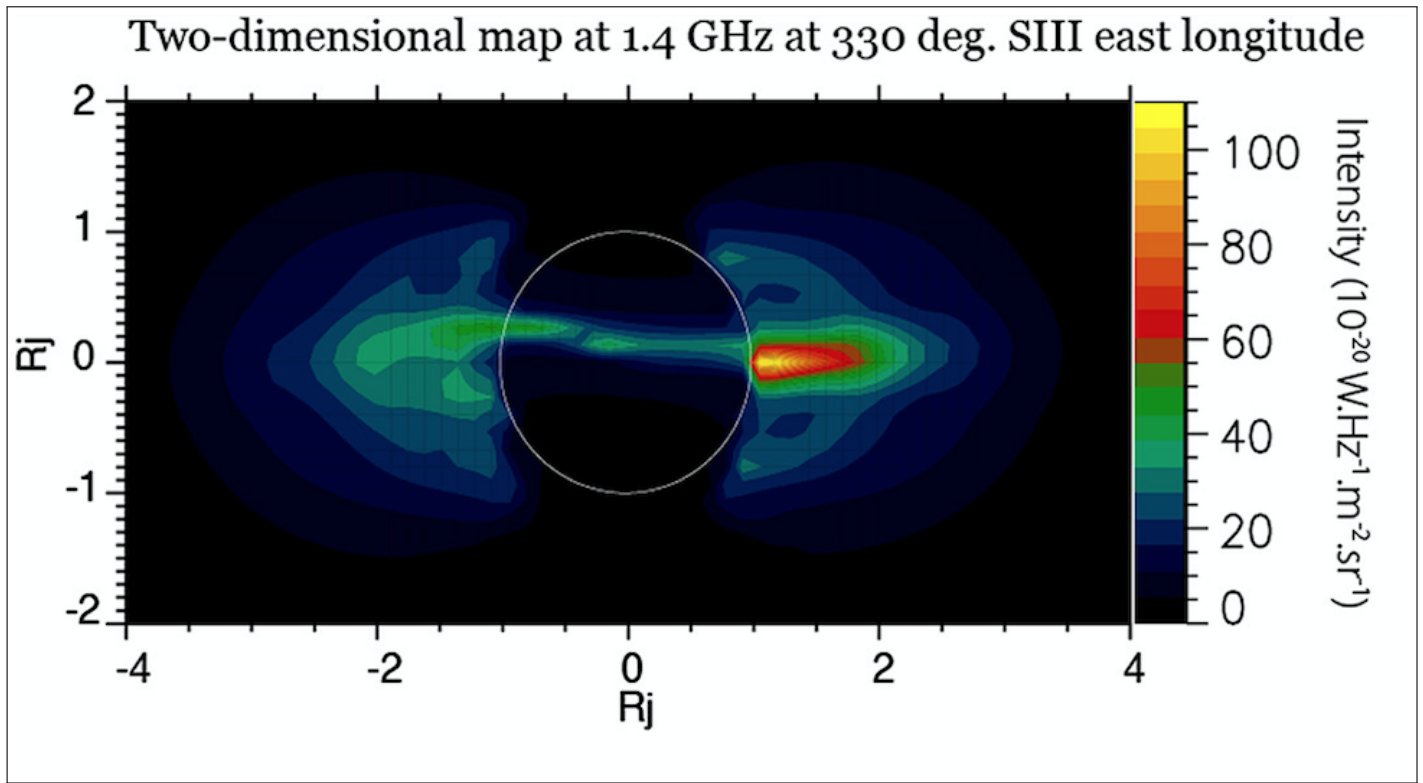


**Fig. 3.** Map of Jupiter's synchrotron emissions at 1.4 GHz (Santos-Costa et al., 2017). Note that in a single scan of Jupiter, only one peak value is observed due to the geometrical perspective of Earth relative to Jupiter's radiation belt at that point in Jupiter's rotation.

### GAVRT SCAN PEAK INTENSITY COMPUTATION

We used scans taken by the GAVRT telescope over January 8, 2018, and January 29-30, 2018.

First, outliers were removed from the scans. For measurements outside the peak (defined by those outside 0.3 degrees of offset from the center offset of 0), a measurement was considered an outlier if it fell considerably above or below the adjacent measurements. To implement this mathematically, we multiplied the differences in scan intensity between the measurement and the adjacent measurements – if this product lied above some threshold, the measurement was an outlier. Outliers were replaced by the average of the adjacement elements. A threshold of  $T = 10^{-3}$  seemed to remove a reasonable number of outliers while minimizing the introduction of stray data points.

To remove the baseline, the noise-reduced curve that lay outside of 0.3 degrees of offset from the target was fit to a quadratic, as most scans have baselines that can be well-approximated by a second-degree polynomial. Then this baseline fit was subtracted

from the data, which placed almost every measurement that was not a part of the peak near zero.

We fit what was left over after baseline subtraction from each scan to a Gaussian curve, as shown in column 3 of Figure 4.

Let  $x$  represent the offset and  $y$  the noise-reduced, baseline-subtracted flux data. Then the Gaussian distribution is given by three parameters:  $a$ ,  $\mu$ , and  $\sigma$ , where  $a$  represents the maximum intensity,  $\mu$  represents the offset of the central maximum, and  $\sigma$  represents the standard deviation.

$$y(x) = ae^{-\frac{(x-\mu)^2}{2\sigma^2}} \quad (1)$$

Attempting to fit a Gaussian to each scan led to some inadequate fits that failed to represent the true maximum intensity. For example, at times the peak of the scan occurred far to the right of central offset. Upon performing a live scan controlling the robotic GAVRT telescope, we discovered that such a false peak may occur when the telescope re-centers after scanning past Jupiter. In order to ensure that the peak is located at the central offset, we introduced bounds on the  $\mu$  parameter of the Gaussian fit:  $-0.3 < \mu <$

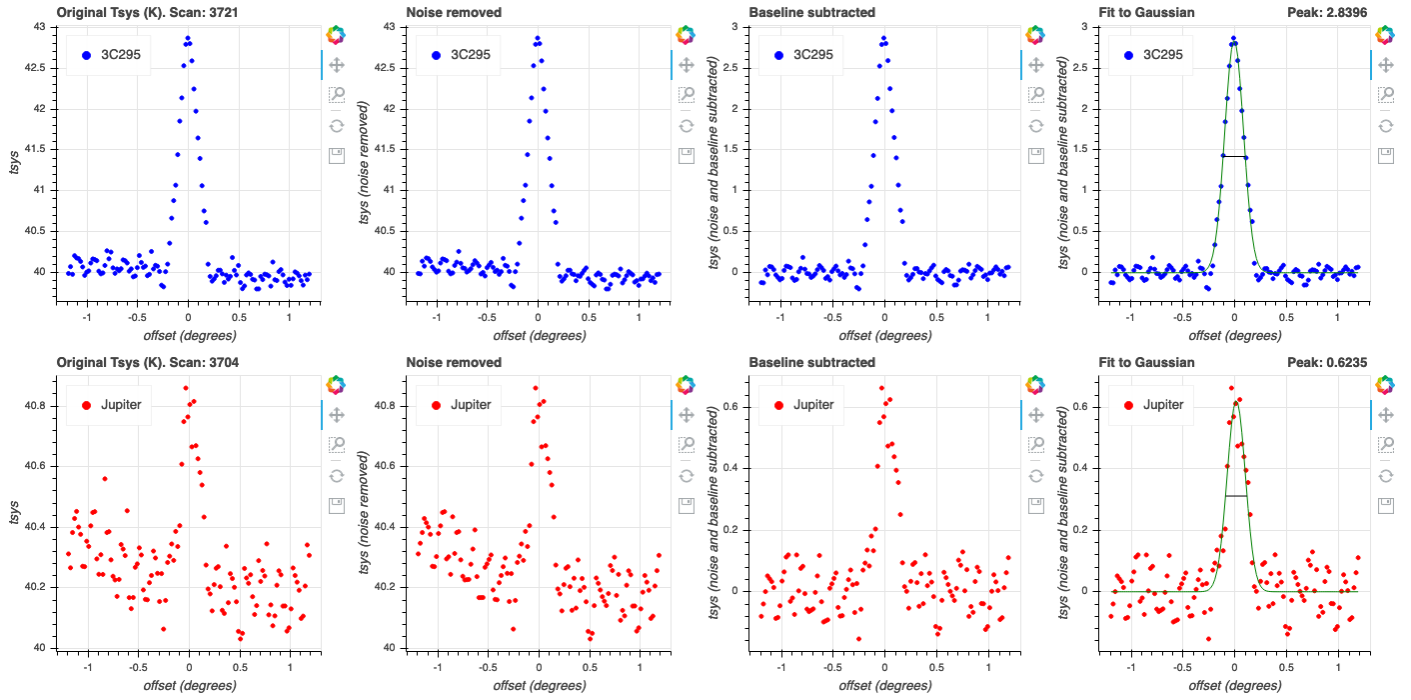


**Fig. 4.** Some example plots of signal data at each stage of processing (from left to right: original, noise removed, baseline subtracted, Gaussian fit). The top row shows a calibrator scan, while the bottom row shows a Jupiter scan.

0.3, where  $\mu$  represents the offset. Such bounds were enforced through the use of the trust region reflective optimization algorithm.

Similarly, it is important that the half-power width remain reasonably constant between scans. Solving for  $x$  in (1) to find the offset at which the half-intensity is reached, we find

$$x = \mu \pm \sqrt{-2\sigma^2 \ln \frac{y}{a}}$$

The half-intensity of the curve is  $y(\mu)/2 = a/2$ .

The half-power width is the distance between the possible  $x$ -values (representing offsets) at this half-intensity, namely

$$H_p = 2\sqrt{2 \ln 2} |\sigma| \quad (2)$$

Thus the half power varies linearly with  $\sigma$ , and we may compute it accordingly. Correspondence with Dr. Velusamy suggested that, from the scan frequency of 2.295 GHz and the telescope diameter of 34m, the half-power width should be fixed to within 20% of 0.225. By (2), we have that  $\sigma$  must lie within 20% of 0.0955—these bounds were also incorporated into the curve fitting algorithm.

## COMPUTATION OF FLUX

Before and after scanning Jupiter, telescopes take scans of a calibrator in order to account for telescope area and other environmental factors such as daily weather conditions. The fundamental principle that allows for such a correction is that, at a given time, the peak intensity of a scan of an emitter (in Kelvin) is proportional to the flux of that emitter (in Janskys). We refer to this ratio the antenna gain.

The relevant constant of proportionality for a given measuring device and set of environmental conditions can be determined by scanning a calibrator for which the flux is known. For the January 8 scans, quasar 3C295 was used as a calibrator; on January 29-30, radio galaxy 3C353 was used. The data from quasar 3C295 was later discarded, as this calibrator's sub-optimal elevation on the date of the scans seems to have compromised the corresponding measurements, as discussed below.

Let  $I$  denote the peak intensity (in Kelvin) and  $F$  denote the flux (in Janskys) for a given source. The subscripts 'c' and 'j' denote the calibrator and Jupiter. Then it follows from the antenna gain relation that

$$\frac{F_j}{I_j} = \frac{F_c}{I_c}$$

Thus we may compute the flux of Jupiter as follows:

$$F_j = I_j \frac{F_c}{I_c} \quad (3)$$

Using the algorithm in the previous section, we compute the peak intensity for Jupiter ( $I_j$ ) at each scan, and the mean peak intensity of all calibrator scans on that day ( $I_c$ ). The mean calibrator intensity is used because there is only one telescope, so the calibrator scans cannot be conducted at precisely the same time as the Jupiter scans. This averaging is acceptable since both calibrators are considered 'stable' sources (Perley & Butler, 2013).

It remains to find  $F_c$ . From (Perley & Butler, 2013), we have that the flux density  $S$  of a quasar can be approximated as a polynomial expression of the form

$$\log(S) = \sum_{n=0}^N a_n \log(v_G)^n$$

where  $v_G$  is the frequency in GHz. Our scans are taken at a frequency of 2.295 GHz. From the coefficients given in the paper, we compute the flux of calibrator 3C295 to be 14.34 Jy, and the flux of calibrator 3C353 to be 39.62 Jy. From these values and the antenna gain relation, we may compute  $F_j$  at each scan according to (3).

Across multiple scans, the distance from Earth to Jupiter may vary, affecting the amount of flux received by our telescope by the inverse square of the distance. Although the variation of distances in our dataset is small, it is important that distance be taken into account for future studies with more scans. We normalize all fluxes to the minimum distance of Jupiter from Earth, 4.04 AU. The normalized flux  $F_J$  can be computed from the distance  $d$  from Jupiter to Earth, and the previously computed flux  $F_j$  by

$$F_J = F_j \left( \frac{d}{4.04} \right)^2$$

## RETRIEVING EPHEMERIDES DATA

In order to understand how the flux varies with other features of Jupiter and its orbit, we accessed the HORIZONS Ephemerides data set. We used the astroquery package to retrieve the data with the target body code of Jupiter (599) and the observer location code for the telescope at the Goldstone Deep Space Communications Complex (257). This allowed

us to query important data from Jupiter, such as the CML at the time of the scan, and collect them into a table such as Table 1.

The Central Meridian Longitude in Table 1 "is based on the 'System III' prime meridian rotation angle of the magnetic field" (Giorgini et al., 1996). As the CML changes, the orientation of the magnetic poles relative to an observer viewing the longitude changes as well, thus affecting the magnitude of the synchrotron radiation emitted.

Table 1 shows data from eight example scans, composed by combining the peak intensities as computed from the GAVRT data with CML and Earth-Jupiter distance data queried from the HORIZONS Ephemerides database.

## MODELING SYNCHROTRON FLUX AS A FUNCTION OF CML

Figure 5 shows Jupiter's flux (both scaled and unscaled for the Jupiter-Earth distance) plotted against the Central Meridian Longitude at each scan, thus producing a rough model of Jupiter's synchrotron radiation as a function of longitude.

The fluxes measured on January 8 using calibrator 3C295 do not produce a smooth curve, suggesting that it is not an appropriate calibrator, likely due to its high elevation relative to Jupiter. The elevations are compared in Table (2).

The two largest outliers are removed in both plots. We may justify their removal through their poor Gaussian fits and thus inaccurate peak intensity, as shown in Figure 6.

To generate a continuous beaming curve, we fit a polynomial model to the 3C353 data. While there was not sufficient data to establish a true periodic fit from a Fourier basis (sum of trigonometric functions), we required the polynomial fit to be semi-periodic – that is, have equal first derivatives at its endpoints:  $f(0) = f(1)$  and  $f'(0) = f'(1)$ . The coefficients with these constraints imposed were determined by Levenberg-Marquardt least squares optimization to minimize residuals. Let  $c$  represent CML measured in degrees. Then the flux  $f(c)$  as a best-fitting polynomial is given by (4), and plotted in Figure 7 (left).

Scan	CML (°)	Jupiter-GAVRT (AU)	peak intensity (K)	Raw Flux (Jy)	Normalized Flux (Jy)
4775	204.0	5.5174	0.68	3.40	6.34
4776	205.5	5.5174	0.57	3.42	6.37
4777	208.4	5.5174	0.63	3.49	6.52
4778	209.8	5.5173	0.60	3.42	6.39
4779	212.1	5.5173	0.71	3.52	6.56
4780	213.6	5.5173	0.67	3.40	6.35
4781	215.5	5.5172	0.69	3.51	6.55
4782	216.9	5.5172	0.70	3.47	6.48

**Table 1.** Example scans with fluxes computed from integrated HORIZONS and GAVRT data.

Source	Mean Elevation	Std. Dev. Elevation
3C295	61.0	9.5
3C353	43.1	10.1
Jupiter	33.6	4.3

**Table 2.** Elevations of Jupiter and Calibrator Quasars

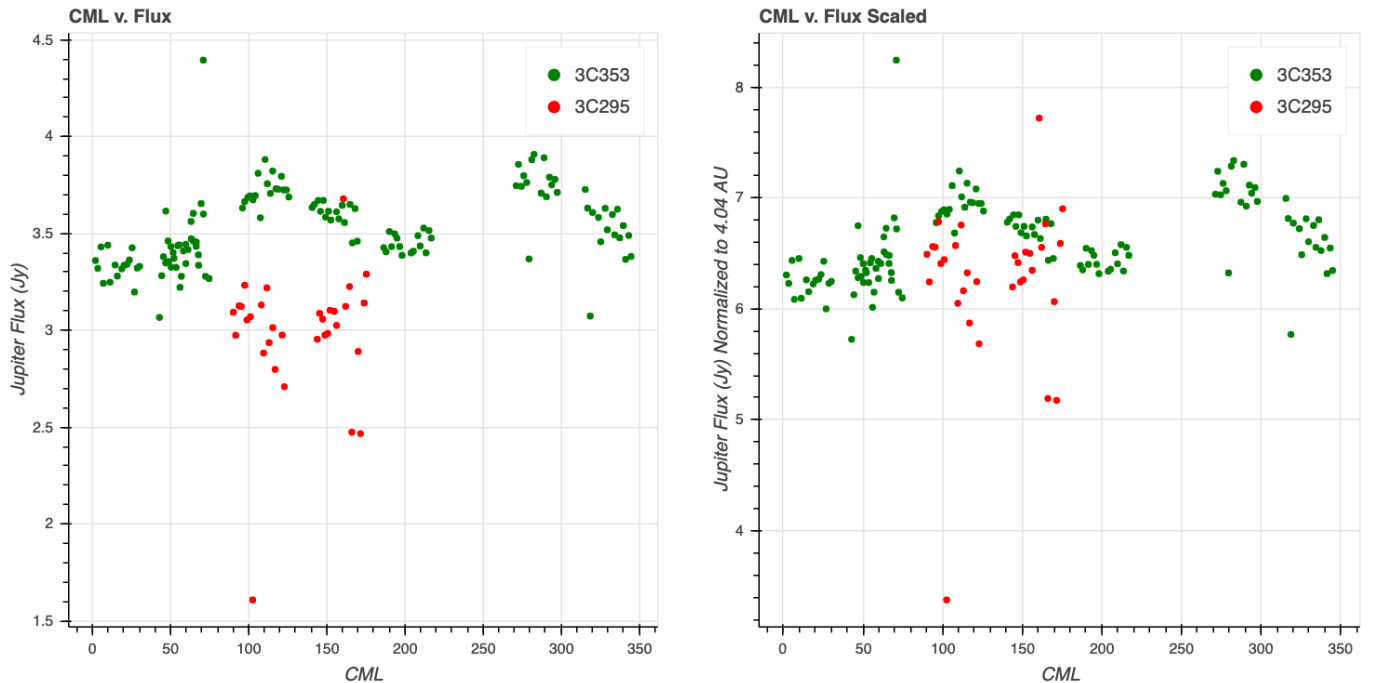


**Fig. 5.** Plots of CML v. Flux of Jupiter's synchrotron radiation measured with different calibrators. (Calibrator 3C295 used on January 8, 2018; Calibrator 3C353 used on January 29-30, 2018.) The right plot is scaled for inverse-square of Jupiter-Earth distance.

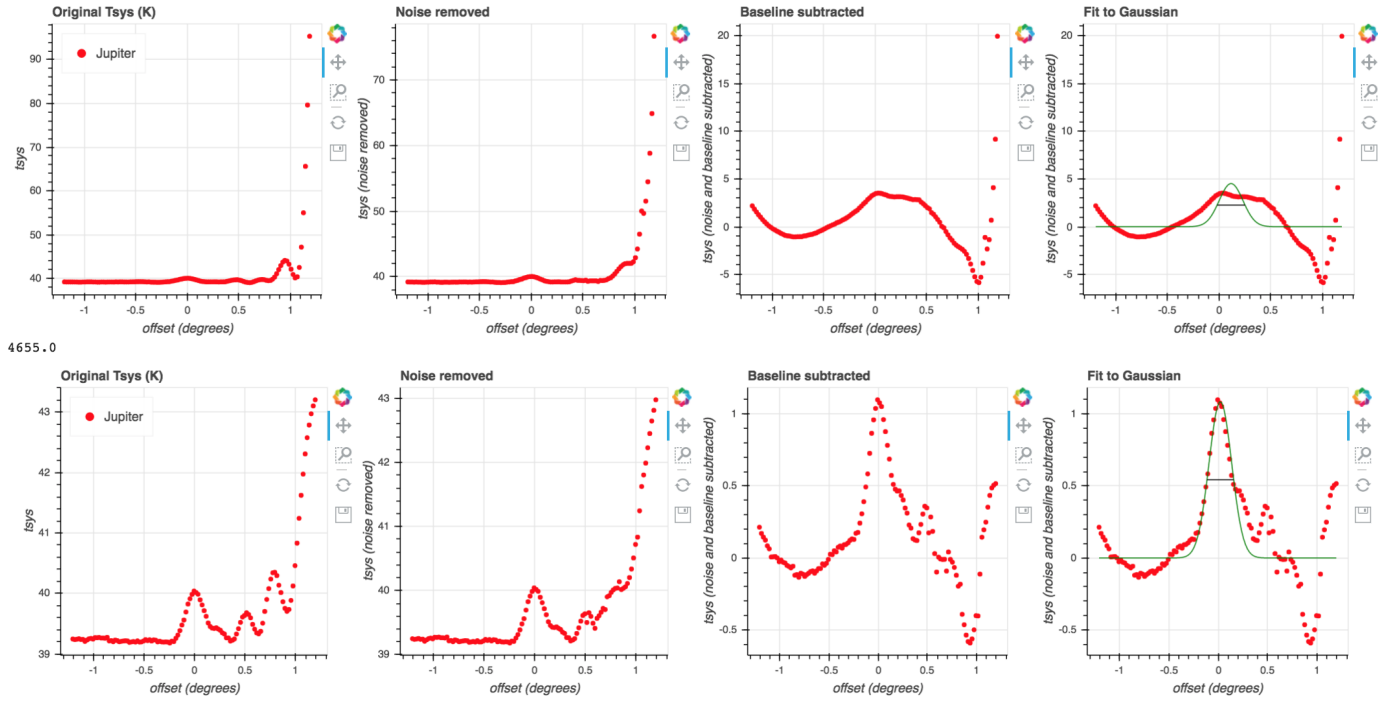


**Fig. 6.** Scans with poor Gaussian fits and outlying peak intensities, shown at each stage of processing (from left to right: original, noise removed, baseline subtracted, Gaussian fit).

$$\begin{aligned}
 f(c) = & 906.734 \left( \frac{c}{360} \right)^7 - 2961.63 \left( \frac{c}{360} \right)^6 \\
 & + 3638.27 \left( \frac{c}{360} \right)^5 - 2056.70 \left( \frac{c}{360} \right)^4 \\
 & + 514.6 \left( \frac{c}{360} \right)^3 - 42.66 \left( \frac{c}{360} \right)^2 \\
 & + 1.472 \left( \frac{c}{360} \right) + 6.189
 \end{aligned} \quad (4)$$

The polynomial function fit well, with a residual square sum (RSS) of 7.94. However, we also believed a sinusoidal function would have made more logical sense in an astronomical context. A piecewise sinusoidal function was manually found to fit the data, given by (5) and shown in Figure 7, with a worse residual sum of squares of 9.23. The piecewise function was necessary as the plot has different amplitudes for the first and second peaks. Residual plots for each curve are compared in Figure 8.

$$f(c) = \begin{cases} -0.44 \cos(0.037(c - 35)) + 6.72 & c < 130 \\ -0.37 \cos(0.037(c - 197)) + 6.82 & c \geq 130 \end{cases} \quad (5)$$

We believe the trigonometric piece-wise function (5) could be beneficial with more data as it makes

more intuitive sense given the periodic nature of the system, but the seventh-degree polynomial fit (4), with a lower RSS and its continuity, should be used for this dataset. We also attempted to find a two-frequency model of the form  $a_0 + a_1 \cos(b_1(x - \delta_1)) + a_2 \cos(b_2(x - \delta_2))$ , but were unsuccessful in finding an adequate fit.

The minima occur at  $0^\circ$  and  $208^\circ$  for the polynomial and  $35^\circ$  and  $267^\circ$  in the trigonometric model. Despite the better fit of the polynomial model, the model constructed by Levin et al. place the first minima at approximately  $35^\circ$ , agreeing with the trigonometric fit (Levin, Bolton, Gulkis, & Klein, 2001).

## FUTURE WORK

Volcanic activity on Io may interfere with Jupiter's magnetic field, which could account for other unexplained variation in fluxes at the same longitude between scan dates (*Observing Jupiter Radio Storms: Past, Present, and Future*, n.d.). Radio bursts from Io in decametric wavelengths are known to affect electrons in Io's field (Clarke et al., n.d.). For future research, it may be useful to compare Jupiter's synchrotron flux at a given longitude with the relative location of Io. It would be necessary to remove the beaming curve, the flux density as a function of CML,



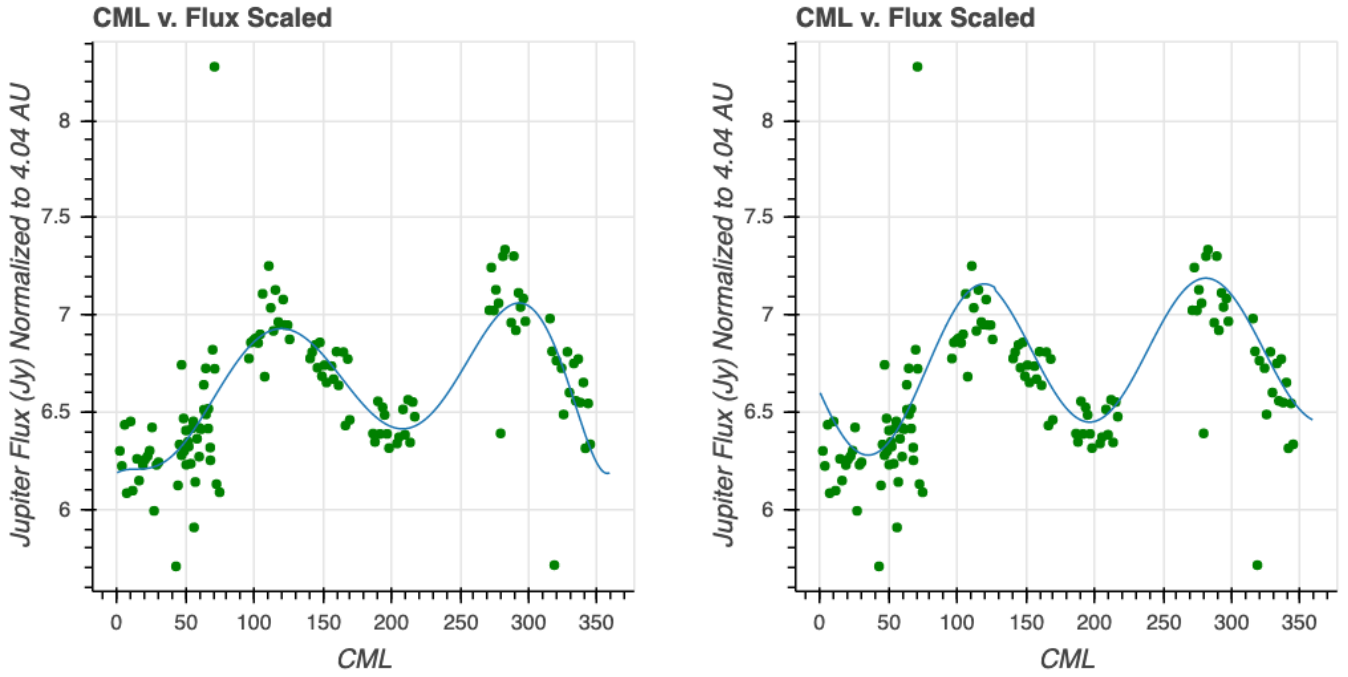


**Fig. 7.** Beaming Curve Fits: Semi-periodic polynomial fit from equation (4) (left); Sinusoidal piece-wise regression for the Flux vs. CML plot (5) (right).

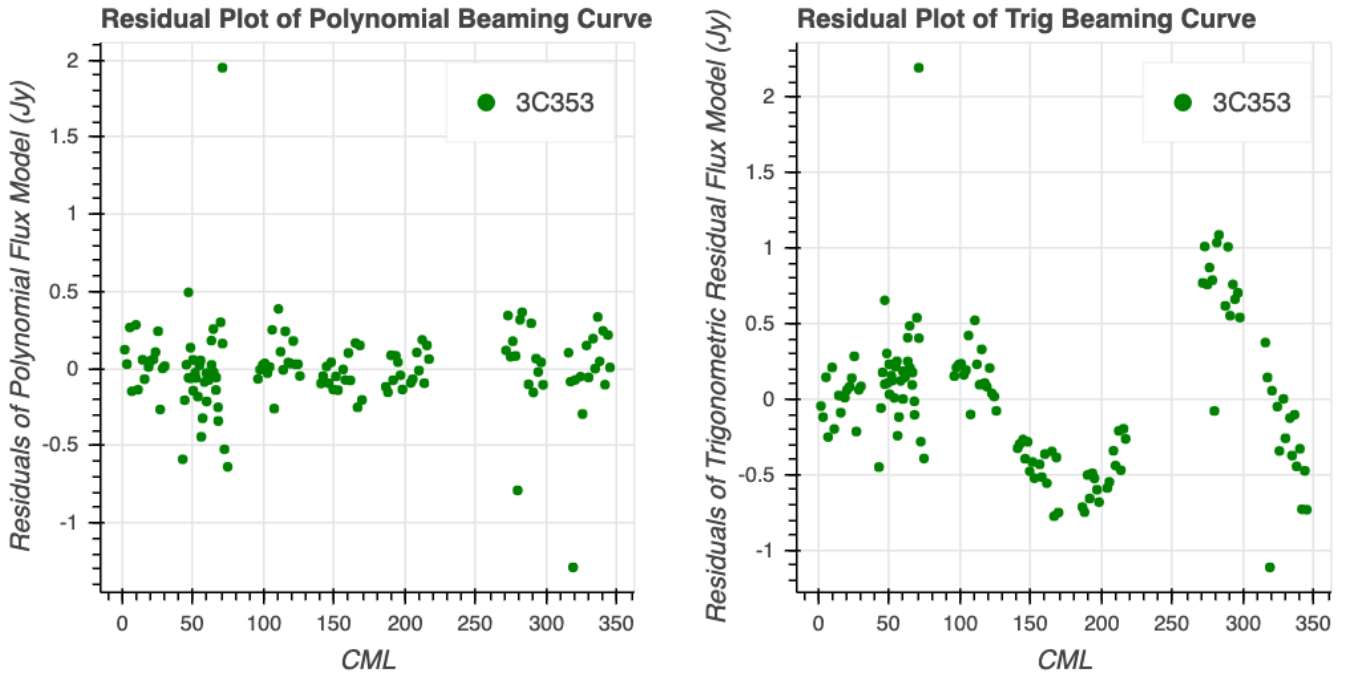


**Fig. 8.** Residual plots of semi-periodic polynomial model (left) and piecewise trigonometric model (right).

to see this. To demonstrate how such an investigation might proceed, we queried the line of longitude on Jupiter nearest to Io's location at each scan time, and computed the difference between Io's Longitude and the CML of Jupiter that is facing Earth. We plotted

this longitude difference against the residuals of the beaming curve, but no general trend was observed. If Io did significantly affect the intensity of synchrotron radiation, we would expect to observe a peak at 0 in Figure 9. However, we had a limited range of dates

of GAVRT data; further research should of course be conducted with a larger dataset.

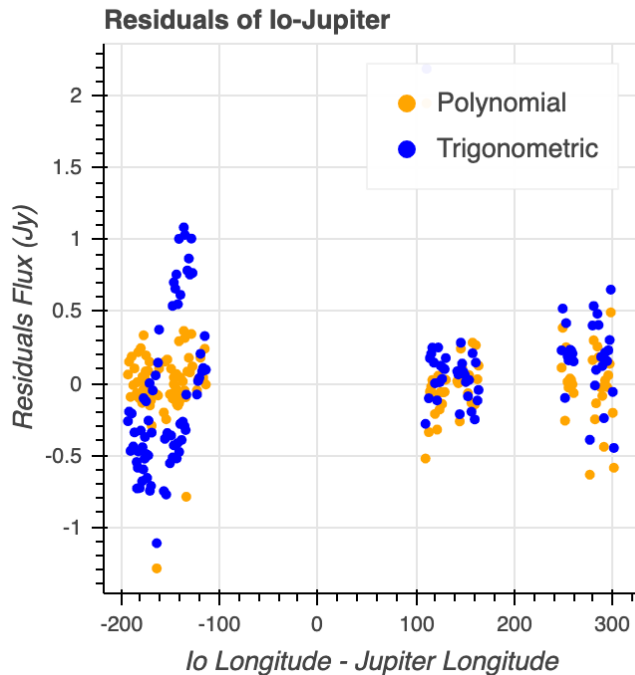


**Fig. 9.** Longitude Difference between the Io and Jupiter plotted against the residual between the estimated and actual flux from each function.

UV radiation from the Sun may also affect Jupiter's radiation belt and thus synchrotron emission. While solar flares and coronal mass ejections would take years to reach Jupiter and have a noticeable effect, UV radiation only would take approximately 43 minutes (traveling at light speed). Thus the effect of UV radiation (reaching Jupiter at various intensities as its orbital radius changes) could be investigated by examining a beaming curve such as that of Figure 8 observed over many more periods of Jupiter's rotation.

## CONCLUSION

We developed code to model the flux of synchrotron radiation in Jupiter's magnetosphere as a function of longitude. We implemented procedures for noise removal, baseline subtraction, and Gaussian fitting to find each scan's peak intensity. We then found the antenna gain ratio in order to compute Jupiter's flux from its scan intensity, as well as the scan intensities and known flux of each calibrator quasar. We scaled the flux for distance so fluxes can be compared between other scans when Jupiter is closer or

farther from Earth. We found a periodic relationship between Jupiter's longitude and synchrotron flux, and fit a predictive mathematical model to this end. This model may help to inform the amount of 2.295 GHz radiation contributed by various sources to the measurements taken by the Juno probe.

## ACKNOWLEDGEMENTS

Special thanks to Dr. Velusamy Thangasamy for providing the GAVRT dataset and explaining his methods for processing it.

Special thanks to the GAVRT staff for providing training sessions and dedicating time to allow us to use the Goldstone Apple Valley Telescope alongside providing useful information relevant to the project.

Special thanks to astronomer Robert Buchheim as well for his thoughtful feedback and suggestions.

## REFERENCES

- Clarke, T., Higgins, C., Skarda, J., Imai, K., Imai, M., Reyes, F., ... Taylor, G. (n.d.). Probing jovian decametric emission with the long wavelength array station 1. *Journal of Geophysical Research*.
- Giorgini, J., Yeomans, D., Chamberlin, A., Chodas, P., Jacobson, R., Keesey, M., ... Wimberly, R. (1996). Jpl's on-line solar system data service. *Bulletin of the American Astronomical Society*, 28(3).
- Goldstone apple valley radio telescope (gavrt). (n.d.). NASA. Retrieved from <https://www.nasa.gov/directorates/heo/scan/communications/outreach/gavrt>
- Greicius, T. (2018). *Juno overview*. Retrieved from [https://www.nasa.gov/mission\\_pages/juno/overview/index.html](https://www.nasa.gov/mission_pages/juno/overview/index.html) (Last accessed 18 January 2019)
- Kollmann, e. a., P. (2017). A heavy ion and proton radiation belt inside of jupiter's rings. *Geophys*, 44, 5259–5268. Retrieved from <https://doi.org/10.1002/2017GL073730> doi:
- Levin, S. M., Bolton, S. J., Gulkis, S. L., & Klein, M. J. (2001). Modeling jupiter's synchrotron radiation. *Geophysical Research Letters*, 28.
- Nave, R. (n.d.). *Synchrotron radiation*. Retrieved from <http://hyperphysics.phy-astr.gsu.edu/hbase/Particles/synchrotron.html> (Last accessed 18 January 2019)
- Observing jupiter radio storms: Past, present, and future*. (n.d.). NASA.

- Perley, R. A., & Butler, B. J. (2013). An accurate flux density scale from 1 to 50 ghz. *The Astrophysical Journal Supplement Series*, 204.
- Santos-Costa, D., Adumitroaie, V., Ingersoll, A., Gulkis, S., Janssen, M. A., Levin, S. M., ... Connerney, J. E. P. (2017). First look at jupiter's synchrotron emission from juno's perspective. *Geophysical Research Letters*, 44(17), 8676-8684. Retrieved from <https://agupubs.onlinelibrary.wiley.com/doi/abs/10.1002/2017GL072836> doi:

# An Exoplanet Transit Observing Method using LCO Telescopes, ExoRequest and astrosource.

JAY SARVA<sup>1,\*</sup>, RACHEL FREED<sup>2</sup>, MICHAEL FITZGERALD<sup>3</sup>, AND SAEED SALIMPOUR<sup>4</sup>

<sup>1</sup>Stanford Online High School, California, USA

<sup>2</sup>Institute for Student Astronomical Research, California, USA

<sup>3</sup>Edith Cowan University, Perth, Australia

<sup>4</sup>Deakin University, Melbourne, Australia

\*Corresponding author: sarva.jay.s@gmail.com

---

Exoplanets have become a very active focus of research in the past few years. This is especially true now as the Transiting Exoplanet Survey Satellite (TESS) was launched in April of 2018 and is expected to find thousands of potential candidate exoplanets every year, with the expectation that students and pro-ams will undertake much of the follow-up work. This paper presents a worked example for those intending to get started with observing exoplanets. We analyzed the transit of the planet HAT P-56 b utilizing data from Las Cumbres Observatory (LCO) Telescopes and two python scripts. One of the scripts, Exorequest, assists with planning the transit observation while the other, astrosource, automates much of the photometric processing of the transit. While this method uses the LCO data and scheduler, this method will work with any typical optical images.

© 2020 Astronomy Theory, Observations and Methods Journal

**Keywords:** Exoplanet astronomy (486), Exoplanet detection methods (489), Astronomical techniques (1684), Astronomical methods (1043)

<https://doi.org/10.32374/atom.2020.1.4>

---

## INTRODUCTION

Since the discovery in 1992 of the first exoplanet orbiting a pulsar (Wolszczan & Frail, 1992) and subsequent 1995 discovery of an exoplanet orbiting a main-sequence star (Mayor & Queloz, 1995), the study of exoplanets has recently exploded, and it will continue growing exponentially into the future. The growth of this field has led to both the discovery of new exoplanets and detailed analysis of known exoplanets, including study of their atmospheres (Seager

& Sasselov, 1998) and potential habitability (Seager, 2013).

The radial velocity method and the transit photometry method have been the two detection methods responsible for most of the exoplanet discoveries. The radial velocity method, proposed in 1952 by Otto Struve (Struve, 1952), finds exoplanets through the observation of Doppler shifts in the parent star's spectrum. Transit photometry detects exoplanets through the slight dimming of a star as the planet passes between the star and Earth (Deeg & Alonso, 2018).

There have been numerous ground-based searches for exoplanets. For example, WASP (Queloz et al., 2010) is one of the most successful ground-based search programs that uses the transit method, as it has discovered over 100 exoplanets. Another example is HATNet (Bakos, 2002), or the Hungarian Automated Telescope Network, which is a set of six robotic telescopes that has discovered several tens of exoplanets since 2003.

There have also been several space-based searches that have been incredibly successful. The Kepler Mission (Borucki et al., 2010) discovered and confirmed over 2000 exoplanets. After one of its gyroscopes failed, it changed its mission, now referred to as K2, and discovered more than 2000 exoplanets. It was retired on October 30, 2018 due to fuel depletion. The Transiting Exoplanet Survey Satellite (TESS) (Ricker et al., 2014), launched in April, 2018, also utilizes transit photometry, and is expected to find 20,000 exoplanets within 2 years. All of these exoplanets are catalogued in NASA's Exoplanet Archive, which is freely available to anyone to conduct further analysis. The example in this paper uses data requested from the Las Cumbres Observatory (LCO) global telescope network (Brown et al., 2013). The process can be applied to non-LCO observatories by using Exorequest as a planning tool and undertaking the observations with the different telescope. These images can then be run through the OSS Pipeline (M. Fitzgerald, 2018) to undertake photometry measurements on the images.

This paper intends to present an efficient method for exoplanet transit observation, analysis and modelling, particularly useful for new entrants into the field, for pro-amateurs, as well as those within student research projects (Fitzgerald, Hollow, Rebull, Danaia, & McKinnon, 2014) and those involved in education programs using the various robotic telescope programs around the world (Gomez & Fitzgerald, 2017). The process is intended to be as robust as possible providing professional quality results. This paper describes in detail: 1) the selection procedure for picking a target, 2) the short script used to request the images, 3) the process used to extract the light curve data from the observed images, and 4) the process used to fit a model transit to the data.

## TARGET SELECTION

As this was the first time the first author had observed an exoplanet transit, an object that would have a high

likelihood of successful observing and analysis was picked. The following steps were used to select the target.

1. To select an exoplanet to observe and track, the [NASA Exoplanet Archive](#) was used (see Figure 1).
2. After clicking on "Confirmed Planets", click on "Select Columns" as seen in Figure 2. Then, check the boxes for Transit Depth, Duration, and Mid-point as seen in Fig 3 and RA and Dec in decimal degrees as seen in Fig 4.
3. An optical magnitude of  $<12$  was selected, to ensure the object would be bright enough to image on the 0.4-meter LCO telescopes. These telescopes can easily observe dimmer exoplanets, but longer exposures would be necessary. A rough limit with the present cameras (SBIG STX6303) is 15th magnitude, where the optimal exposure time becomes  $\approx 400$  seconds with a w filter.
4. A short period was also queried to allow for multiple attempts to observe the transit. As not every attempt to observe a given transit will be successful, mainly due to weather or competing observers, a shorter period allows more possible attempts within a given time period. This is particularly important as an exoplanet with a longer time between transits might only allow for a small number of periods to be observed within a given timeframe, while a shorter period planet might allow for many more transits to be observed.
5. The search was further narrowed to select for a transit depth of  $>1\%$  as the bigger the transit depth, the more noticeable the transit would be on the light curve during analysis. The choice of  $1\%$  is because this is the rough level of scatter for an earth-bound observatory on a typical good night.
6. An appropriate right ascension (RA) of between  $[30,90]$  degrees, which contains the optimal RA value for the given time of the year, 60 degrees, was selected. Targets near this value will be in the sky for the longest period of time over the course of the night for any given observatory. We provide a rough list of best RA values for a given time of the year in Table 1.



There were only a few options of exoplanets that fit all of these criteria to observe, one of which was HAT-P-56 (Hartman et al., 2015). It had a relatively large transit depth, and was very close to the optimal RA. It turns out that HAT-P-56 also has a relatively short transit duration and period, so that meant it was possible to make many observations in a short timespan.

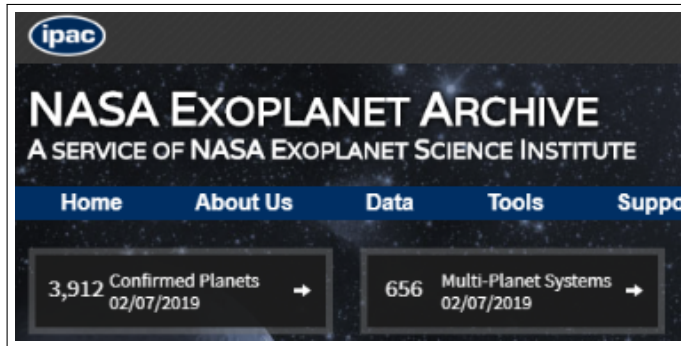


**Fig. 1.** NASA Exoplanet Archive. Click on "Confirmed Planets."

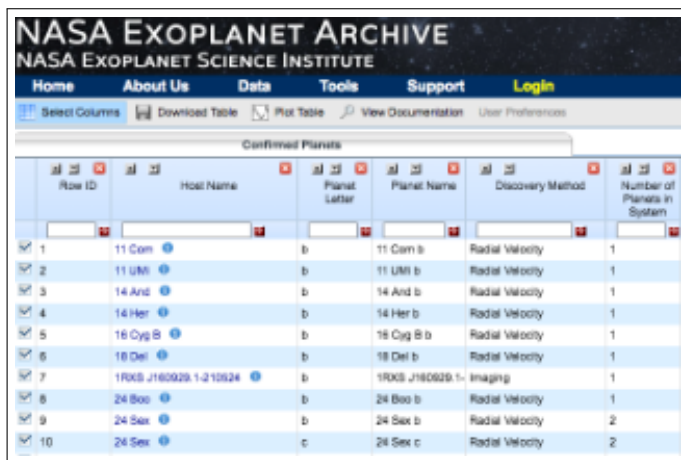


**Fig. 2.** Click "Select Columns."

## USING EXOREQUEST TO REQUEST IMAGES

Exorequest (available [here](#)) is a short python script able to be run online to plan observation times for a given exoplanet transit. It can automatically submit a request to the LCO scheduler, although it can also be used to estimate transit times for any given observatory.

It uses Google Colaboratory for collaborating in Python with other individuals over the internet. To use the version online, a copy will need to be made (File menu -> Save a copy in Drive).

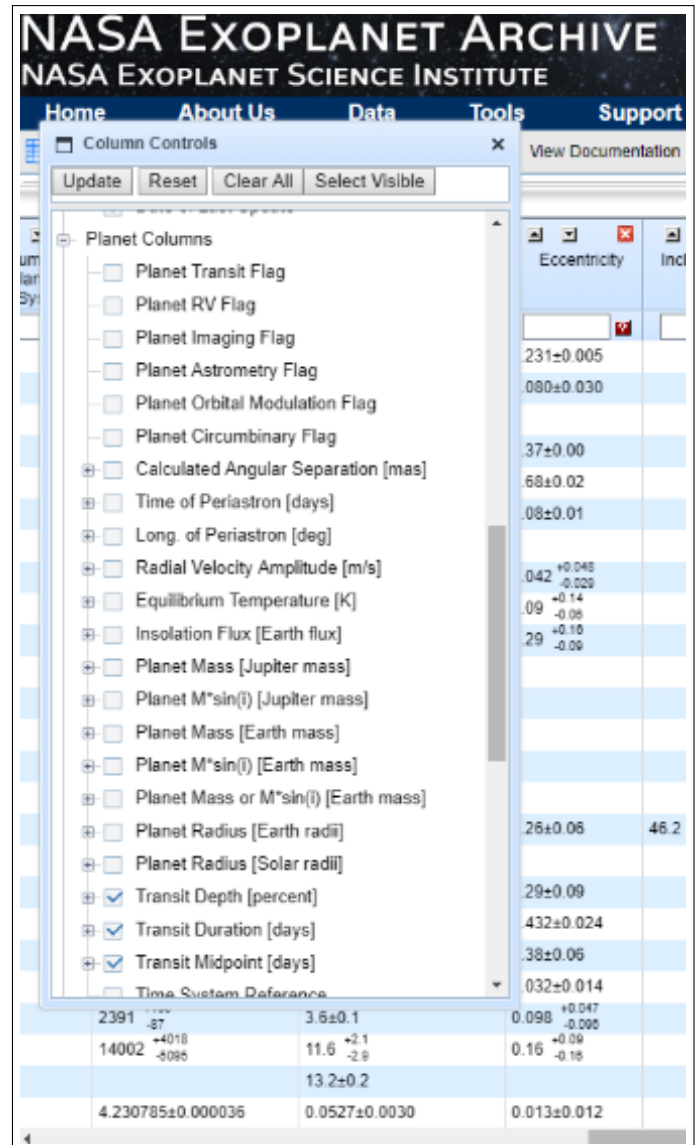


**Fig. 3.** In the NASA Exoplanet Archive check the boxes for Transit depth, Transit Duration and Transit Midpoint and for RA and Dec (decimal degrees).



**Table 1. Preferable right ascensions based on the time of year in both degrees and hours.**

Month	Right Ascension(°)	Month	Right Ascension(°)	Month	Right Ascension(°)
January	120 (45-195)	May	240 (165-315)	September	0 (285-75)
February	150 (75-225)	June	270 (195-345)	October	30 (315-105)
March	180 (105-255)	July	300 (225-15)	November	60 (345-135)
April	210 (135-285)	August	330 (255-45)	December	90 (15-165)
Month	Right Ascension(hrs)	Month	Right Ascension(hrs)	Month	Right Ascension(hrs)
January	8 (3-13)	May	16 (11-21)	September	0 (19-5)
February	10 (5-15)	June	18 (13-23)	October	2 (21-7)
March	12 (7-17)	July	20 (15-1)	November	4 (23-9)
April	14 (9-19)	August	22 (17-3)	December	6 (1-11)

**Table 2. Data needed for ExoRequest to calculate optimal beginning and end times of observation as well as request exoplanet transit images from the Las Cumbres Observatory telescope network.**

Object requested	HAT-P-56b	notes
Transit Midpoint	2456768.50899	BJD preferably, although HJD or JD is approximately correct
Transit Duration (hrs)	2.30	Use decimal format in hours.
Period (days)	2.790830	Orbital Period in days
Period Multiple	1	This value represents which transit in the future you would like to observe. 1 is the next transit, 2 is the transit after that, 3 is the transit after that and so forth.
Optical Mag	10.908	This magnitude is provided in the Nasa Exoplanet Archive. If V band is not available use the Gaia G band.
Exposure Time	0	Set to 0 and it will calculate for you.
RA	100.848038	Use decimal format.
Dec	27.252293	Use decimal format.

**Fig. 4.** In the NASA Exoplanet Archive check the boxes for Transit depth, Transit Duration and Transit Midpoint and for RA and Dec (decimal degrees).

Table 2 shows the information that was needed to be input into the ExoRequest script. This information was obtained from the NASA Exoplanet Archive as described above.

Several parameters are necessary to run the ExoRequest script, all of which are noted in Table 2. The transit midpoint, transit duration, period, RA, and Dec can all be found in the various columns of the NASA Exoplanet Archive, which was explored earlier. "Period Multiple" tells the code to pick either the next available transit (1) or the transit after that (2), and so on.

## HOW EXOREQUEST WORKS

Given an estimated period and an estimated time of midtransit, ExoRequest first estimates the centrepoint of the  $n^{th}$  next upcoming transit, where  $n$  is given by the value of "Period Multiple" set by the user. Even with a global telescope network with multiple sites and telescopes, such as LCO, it is usually unlikely that any given transit is situated well in space and time to be observed by any given observatory (or set thereof). For LCO telescopes, the scheduler will tell the user whether it is available or not. For non-LCO telescopes, the user can set the longitude and latitude

of the observatory and ExoRequest will indicate if the transit is observable. To find the next available observable transit, the user needs to increase "Period Multiple" by 1 until there is an observable transit.

ExoRequest takes the estimated transit centrepoint ( $T_c$ ) and uses the provided estimate of the transit duration, requested out-of-eclipse length and the requested buffer to calculate the start and beginning times of the transit observation. A schematic diagram of this is shown in Figure 5. The out-of-eclipse length is the amount of time, set by the user, that should be observed outside of the transit period. This should be an extended period of time as it is necessary to normalise the transit and to clearly see where the transit starts and ends.

The buffer value is a much smaller value that helps with giving the LCO scheduler a little bit of "wiggle room". For both an LCO and a non-LCO observer, this also makes sure that the transit is still observed even if the timings of the transit center or period were slightly misestimated. ExoRequest will also estimate the exposure time and number of exposures needed if provided a visual magnitude estimate. These values can also be overridden for different filter sets and cameras.

## OBSERVATIONS

Images were obtained by the Las Cumbres Observatory (Brown et al., 2013) 0.4-m telescope located at the McDonald Observatory in Texas, which has been in operation since its installation in April 2012. The network of 0.4-m telescopes were equipped with CCD cameras (SBIG STX6303) with  $4K \times 4K$  pixels, each of which is 0.57 arcseconds square. This gives the telescopes a total Field of View (FoV) of  $19 \times 29$  arcminutes. In our observations, the w-band filter was used to maximise sensitivity and minimise the exposure time per image. The data came from two separate dates: Dec 7, 2018 (624 images) and Dec. 4, 2018 (426 images).

## DATA ANALYSIS

The data, consisting of 1050 images over two different transit periods were processed by the OSS Pipeline (M. Fitzgerald, 2018). This pipeline automatically reduces the images and performs photometry on each one, providing multiple types of photometry. The type of photometry selected for use in this study was

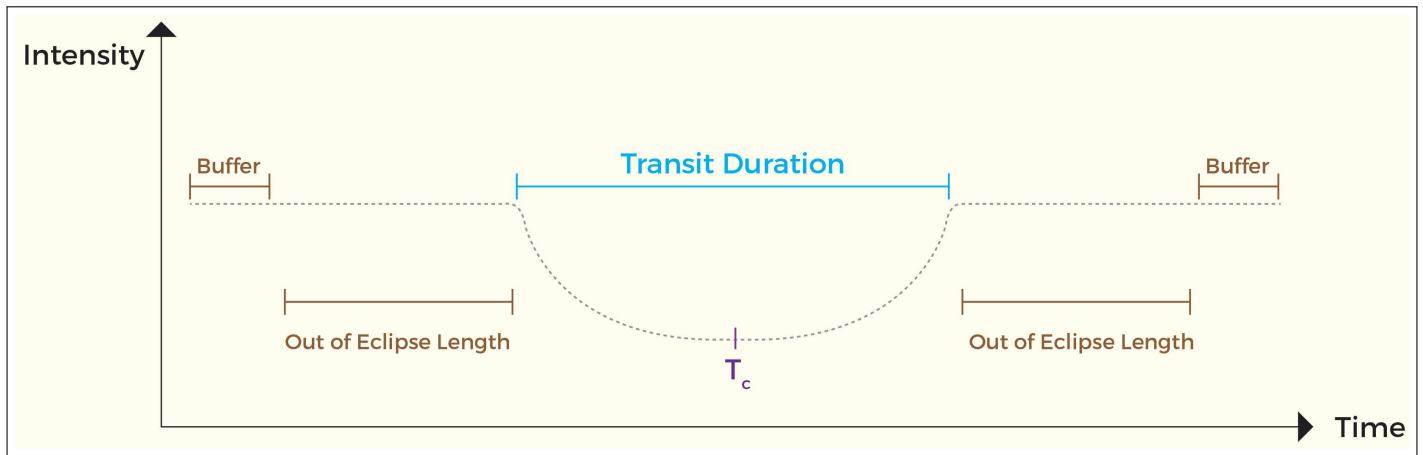


**Fig. 5.** A schematic diagram of the various aspects that ExoRequest takes into account when choosing a beginning and end time of observation.

PSFEx (Bertin, 2011) Point-Spread-Function (PSF) photometry. PSF photometry, when available and feasible, generally provides a higher signal-to-noise than traditional aperture photometry (Heasley, 1999). The use of the pipeline can be bypassed by using LCO provided images which already contain Source Extractor (Bertin & Arnouts, 1996) Photometry.

The *astrosources* python script was used to extract the transit lightcurve from the photometry for each image. The process is described in the following steps:

1. Before starting the process of running each python script, all the observations from a single period must be inserted into the 'inputs' folder.
2. The script sorts through the images and finds the image with the most stars detected by the photometry. That image will be used as a reference frame.
3. After selecting the reference image, the program then sorts through the images and removes the target star as well as any stars that have total counts that are too high (usually 1000000) or too low (usually 10000). This means that stars that have counts that are too high (nearing saturation) and stars with too few counts to achieve a high enough signal-to-noise are both removed.
4. Each image is then reviewed for the number of stars detected. If there are too few stars detected, the image is rejected from the analysis. At the end, the script will output a list of potential comparison stars that have a sufficient brightness and exist in every single image. It will also list out

all the images that it plans to use that have not been rejected.

5. The next step picks out the specific comparison stars to be used. Every potential comparison star's variability is measured. Essentially, all the counts of the comparison stars are added up to create a larger comparison star, and every individual comparison star's variability will be compared to the sum of all the comparisons. Then, any star with variability greater than 3 times the standard deviation of the variability is not included in further searches. The process repeats until no comparison stars are rejected and a list of potential comparison stars and their variability is listed.
6. Finally, the potential comparison stars are sorted in order of increasing variability. Comparison stars are then picked from this list in order, until either the total number of counts exceeds 1000000 ADU, or if the variability of the star exceeds a specific threshold (in this case, 0.025 mag was used). This leaves us with a list of the least variable, optimal, set of comparison stars to be used with this specific dataset.
7. The second last step essentially generates the light curve for the exoplanet using differential photometry against the sum of the identified comparison stars.
8. The final step is to subtract and even out the baseline of the curve using the out-of-transit observations - removing any slight trends over time

in the data and normalising the data - as well as remove any outlier data points that might cause some issues when trying to fit a curve. Prior to this detrending, the transit looks like Figure 6. The slight trend can clearly be seen as well as some obviously poor data values at the end of the transit.

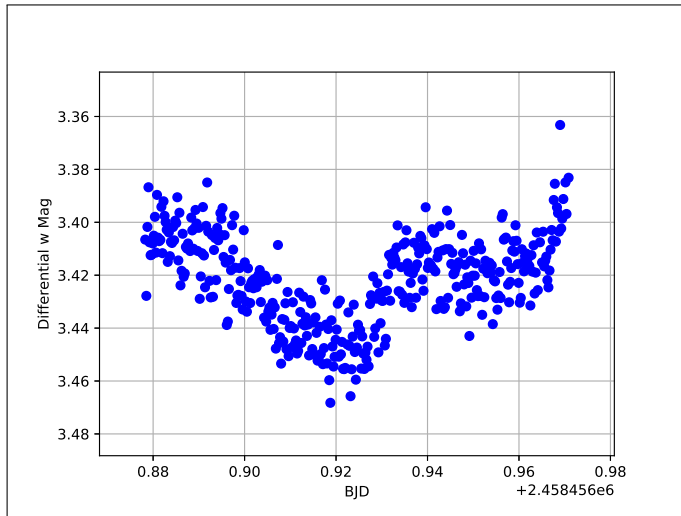


**Fig. 6.** Light curve for the data from the LCO telescopes from Dec 4, 2018

## FITTING A MODEL USING ASTROIMAGEJ

After producing the transit lightcurve from our data, the next step was to fit a transit model to the light curve. To do this, a version of ImageJ known as AstroImageJ (Collins, Kielkopf, Stassun, & Hessman, 2017) was utilized. The steps are outlined below.

1. The first step is to ensure that all earlier AIJ preferences for the multiplot function have been reset to default.
2. First, the table with the data from the light curve produced by the astrosources scripts must be opened by clicking "Open Table From File" in the "File" dropdown. Then, in the main window, select X-data to be "Col\_1," select Y-data to be "Col\_2," check the "Input in Mag" button, and change the colour to Black. Changing the colors will allow for better recognition of the various parts of the fit, and therefore those mentioned in this paper are entirely arbitrary. Finally, ensure to set the "Fit Mode" to the icon that looks like an exoplanet transit.
3. In the Fit Settings window, go to the Plot Settings box. Change the Model line color to "Red" and set the thickness to 3. Furthermore, change both the Residual line color and Symbol Color to purple, and change the shift as much as necessary to clearly separate the two plots such that there is minimal overlap. The settings for the colour and the line thickness are selected to allow for easier analysis of the visualised data.
4. Specify in the same window the estimated period of the exoplanet transit and the radius of the star. It is the radius, not the other values, that is essential as this is used to estimate the true radius of the exoplanet. The other star parameter values have no effect on the measurement.
5. If the orbital eccentricity is known beforehand, uncheck the "Cir" box (which would automatically assume a circular orbit) and enter in the eccentricity (and if available, the omega value).
6. Next, uncheck the "Auto Update Priors" box. Go to the [EXOFAST - Quadratic Limb Darkening website](#) which interpolates the (Claret & Bloemen, 2011) quadratic limb darkening tables and enter the temperature value, the log(g) value and the [Fe/H] value for your star as well as selecting the filter used. Clicking submit will output two values. The left value is for Quad LD u1 and the right value is for Quad LD u2 which can then be entered into the fit window. If sufficient information about the star is not available, select both Quad LD u1 and Quad LD u2 as 0.3, which is the default value. At this point, Quad LD u1 and Quad LD u2 can be set to Lock.
7. Set Baseline Flux (Raw) to lock and uncheck use. Change the value of Prior Centre until the out-of-transit lightcurve data roughly lines up with 1.00 on the y-axis.
8. Set  $T_c$  to Lock and uncheck use. Change the value of prior center until it is roughly the value of the center of the transit and unlock it.
9. At this point, it will be necessary to adjust Prior Centers for  $R_p/R^*$ ,  $a/R^*$ ,  $T_c$  and Inclination until a suitable model is autofit. The key is to attempt to minimize the residual RMS value. You may need to lock or unlock some of these values at various times.

- Once a reasonable fit has been acquired, in the “Fit Settings” window, go to file menu and select “save fit results as text file”, this will save the results of your curve to a text file. The most important parameter is the “Planet Radius ( $R_{\text{jup}}$ )” which provides the radius of the planet in terms of the radius of Jupiter.

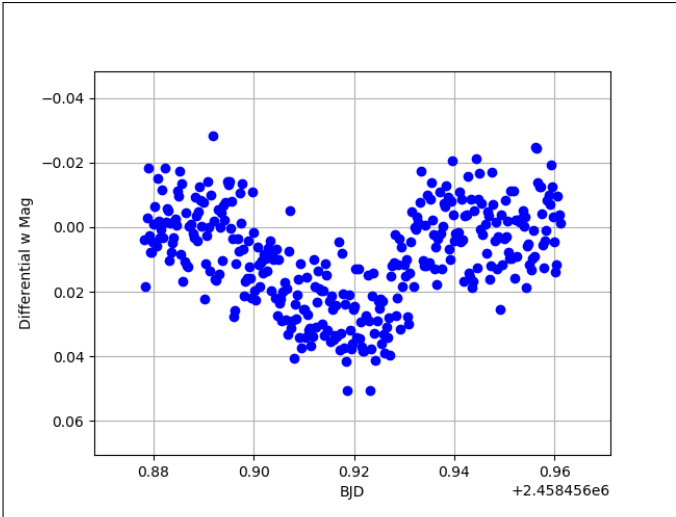


**Fig. 7.** Light curve for the data from the LCO telescopes from Dec 4, 2018

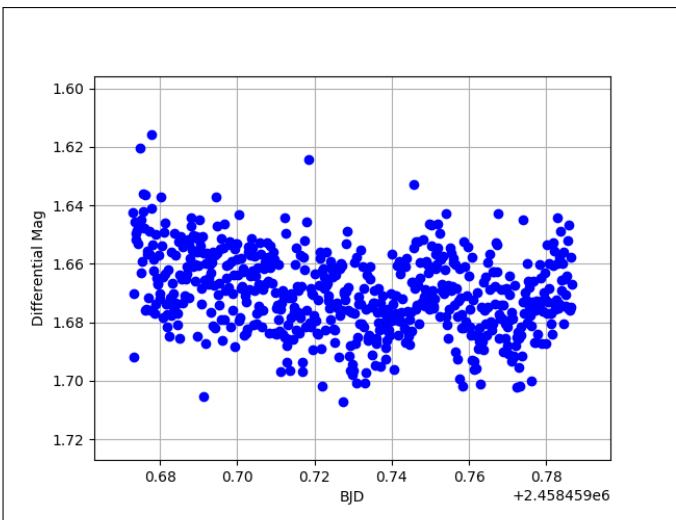


**Fig. 8.** Light curve for the data from the LCO telescopes from Dec 7, 2018. The data from this period appeared to be significantly more noisy and less easily decipherable compared to the other transit.

## RESULTS

We took observations of two different transits. The first lightcurve observed is shown in Figure 7, and

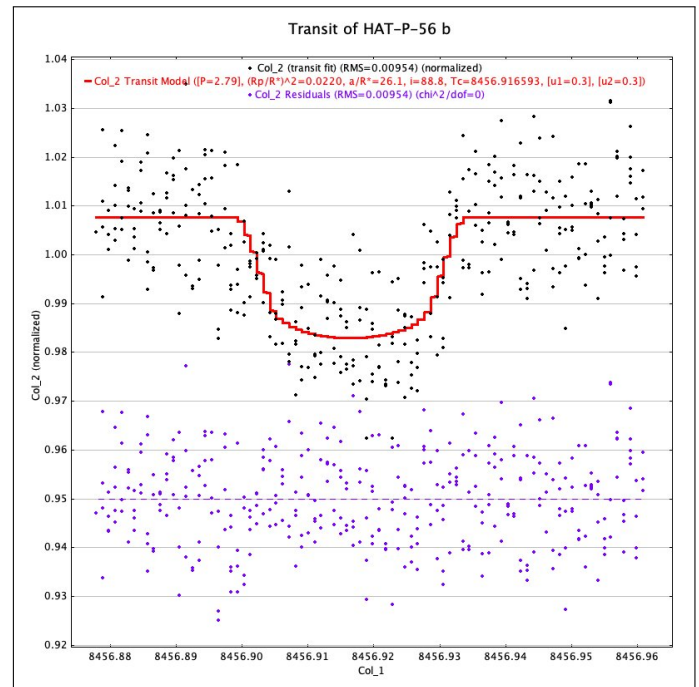


**Fig. 9.** Fit reached through AstroImageJ.

the second lightcurve observed is shown in Figure 8. The first light curve shows a distinct dip, which is representative of a transiting object. The second curve was not the expected shape of a transit, as it had a slight unexpected bump in the middle of the dip and a much larger scatter in the data.

The lower quality data in the December 7th data was likely due to poor weather and seeing at the site at that time. This illustrates the point that even when observations are made at high quality locations with professional instrumentation, the high quality requirements when observing exoplanet transits may be thwarted by conditions outside of the observer's control, such as the weather. When attempting to fit the second lightcurve with a transit model in AstroImageJ, a reasonable fit was not obtained due to the quality of the data.

The December 4th transit lightcurve and the resulting fit are shown in Figure 9. It has a relatively even baseline alongside a very "clean" dip. The planet radius calculated based on the fit settings we used here was  $1.45R_{\text{j}}$ , which is quite close to the published radius of HAT-P-56b of  $1.466R_{\text{j}}$  (Huang et al., 2015).

## DISCUSSION

It is particularly difficult to undertake exoplanet transit observations for beginning astronomers, and this paper provides a simplified approach. This method



enables pro-ams, students and teachers to pursue amateur exoplanet research with a robust approach that can eventually contribute to [TESS follow-up](#) and other exoplanet projects, such as the Exoplanet Timing Survey ([Zellem et al., 2020](#)).

In particular, the use of the OSS Pipeline ([M. Fitzgerald, 2018](#)) removes the necessity of undertaking manual flat/bias/dark reduction (although images provided by LCO are already corrected for these instrumental signatures). The OSS Pipeline automatically fixes header or WCS issues (and automatically estimates a WCS where missing) as well as calculates a variety of new useful header items. A particularly useful example of header adjustment for exoplanets is that the BJD is calculated and inserted directly into the header and into a human-readable filename. The use of the pipeline saves many hours of tedious processing. It also performs all of the photometry necessary, providing 3 PSF types and 3 aperture-based photometry methods, all undertaken with professional level software.

The use of ExoRequest allows the accurate planning (and requesting, if using LCO) of a given exoplanet transit. For a beginner, there is a lot to think about when the transit occurs, when to begin and end observing as well as whether the transit can be clearly observed at a given site, date and time. For a more advanced user, ExoRequest still acts to streamline the selection and submission process for a given transit.

Through the use of astrosource, many of the time-consuming considerations with regards to differential photometry are taken care of as well as removing multiple sources of potential mistakes and bias. For instance, astrosource selects the least variable set of stars within the provided data (as well as rejecting known variable stars), allowing a selection of the absolute best comparison stars in any field within a specific set of data. This makes the selection of comparison stars rapid and also the most optimised, which is simply not possible with manual selection of comparison stars. Astrosource also provides a detrend function that removes any slight trends apparent in an exoplanet lightcurve using the out-of-transit data.

The photometric output of astrosource can be imported directly into AstroImageJ to use the inbuilt modelling functionality that is available there. There are plans in future to explore some of the more advanced transit modelling packages available in python. However, AstroImageJ is well known in the pro-am community for exoplanet analysis and is a

good graphical way to explore modelling the transit lightcurve.

## CONCLUSION

Overall, through the use of ExoRequest, the astrosource scripts and AstroImageJ, we were able to produce a robust plot of a transit lightcurve of the exoplanet HAT-P-56 b. We did have to reject one of the two observed transits due to poor seeing and weather conditions at the time of observation. This method streamlines many of the time-consuming processes for planning, observing and analysing a given exoplanet transit, provides professional quality results while removing multiple layers of human-induced error and bias.

## ACKNOWLEDGMENTS

This work makes use of observations from the LCO global telescope network. Telescope time was provided by the Global Sky Partners program at LCO.

This research has made use of the NASA Exoplanet Archive, which is operated by the California Institute of Technology, under contract with the National Aeronautics and Space Administration under the Exoplanet Exploration Program.

## REFERENCES

- Bakos, G. A. (2002). "system description and first light curves of the hungarian automated telescope, an autonomous observatory for variability search". , 114(799), 974-987.
- Bertin, E. (2011, July). Automated Morphometry with SExtractor and PSFEx. In I. N. Evans, A. Accomazzi, D. J. Mink, & A. H. Rots (Eds.), *Astronomical data analysis software and systems xx* (Vol. 442, p. 435).
- Bertin, E., & Arnouts, S. (1996). SExtractor: Software for source extraction. *Astronomy and Astrophysics Supplement Series*, 117(2), 393-404.
- Borucki, W. J., Koch, D., Basri, G., Batalha, N., Brown, T., Caldwell, D., ... others (2010). Kepler planet-detection mission: introduction and first results. *Science*, 327(5968), 977-980.
- Brown, T., Baliber, N., Bianco, F., Bowman, M., Burleson, B., Conway, P., ... others (2013). Las cumbres observatory global telescope network. *Publications of the Astronomical Society of the Pacific*, 125(931), 1031.



- Claret, A., & Bloemen, S. (2011, May). Gravity and limb-darkening coefficients for the Kepler, CoRoT, Spitzer, uvby, UBVRIJHK, and Sloan photometric systems. , 529, A75. doi:
- Collins, K. A., Kielkopf, J. F., Stassun, K. G., & Hestman, F. V. (2017, Feb). AstroImageJ: Image Processing and Photometric Extraction for Ultra-precise Astronomical Light Curves. , 153(2), 77. doi:
- Deeg, H. J., & Alonso, R. (2018). Transit photometry as an exoplanet discovery method. *Handbook of exoplanets*, 633–657.
- Fitzgerald, Hollow, R., Rebull, L. M., Danaia, L., & McKinnon, D. H. (2014). A review of high school level astronomy student research projects over the last two decades. *Publications of the Astronomical Society of Australia*, 31.
- Fitzgerald, M. (2018). The our solar siblings pipeline. *RTSRE Proceedings*, 1(1), 347–358.
- Gomez, E. L., & Fitzgerald, M. T. (2017). Robotic telescopes in education. *Astronomical Review*, 13(1), 28–68.
- Hartman, J. D., Bhatti, W., Bakos, G. Á., Bieryla, A., Kovács, G., Latham, D. W., ... others (2015). Hat-p-50b, hat-p-51b, hat-p-52b, and hat-p-53b: three transiting hot jupiters and a transiting hot saturn from the hatnet survey. *The Astronomical Journal*, 150(6), 168.
- Heasley, J. N. (1999, Jan). Point-Spread Function Fitting Photometry. In E. R. Craine, D. L. Crawford, & R. A. Tucker (Eds.), *Precision ccd photometry* (Vol. 189, p. 56).
- Huang, C. X., Hartman, J. D., Bakos, G. Á., Penev, K., Bhatti, W., Bieryla, A., ... Sári, P. (2015, Sep). HAT-P-56b: An Inflated Massive Hot Jupiter Transiting a Bright F Star Followed Up with K2 Campaign 0 Observations. , 150(3), 85. doi:
- Mayor, M., & Queloz, D. (1995). A jupiter-mass companion to a solar-type star. *Nature*, 378(6555), 355–359.
- Queloz, D., Anderson, D. R., Collier Cameron, A., Gillon, M., Hebb, L., Hellier, C., ... West, R. (2010, July). WASP-8b: a retrograde transiting planet in a multiple system. , 517, L1. doi:
- Ricker, G. R., Winn, J. N., Vanderspek, R., Latham, D. W., Bakos, G. Á., Bean, J. L., ... others (2014). Transiting exoplanet survey satellite. *Journal of Astronomical Telescopes, Instruments, and Systems*, 1(1), 014003.
- Seager, S. (2013). "exoplanet habitability". *Science*, 340(6132), 577-581. doi:
- Seager, S., & Sasselov, D. D. (1998). Extrasolar giant planets under strong stellar irradiation. *The Astrophysical Journal Letters*, 502(2), L157.
- Struve, O. (1952, October). Proposal for a project of high-precision stellar radial velocity work. *The Observatory*, 72, 199-200.
- Wolszczan, A., & Frail, D. A. (1992). A planetary system around the millisecond pulsar psr1257 + 12. *Nature*, 355(6356), 145-47.
- Zellem, R. T., Pearson, K. A., Blaser, E., Fowler, M., Ciardi, D. R., Biferno, A., ... others (2020). Utilizing small telescopes operated by citizen scientists for transiting exoplanet follow-up. *Publications of the Astronomical Society of the Pacific*, 132(1011), 054401.

# Observations of Eclipsing Binary EPIC 201826968

UMAR AHMED BADAMI<sup>1</sup>, LOUIS GOSART<sup>1</sup>, JAKE NORTH<sup>1</sup>, AND KALÉE TOCK<sup>1</sup>

<sup>1</sup>Stanford Online High School, Stanford, CA, USA

The eclipsing binary system EPIC 201826968 was imaged using the Las Cumbres Observatory Global Telescope Network with Bessel-B, Bessel-V, SDSS-r' and SDSS-i' filters. AstroImageJ was used to determine the optimal exposure time for the images. We coded a phase-dispersion minimization (PDM) algorithm and compared its result to PyAstronomy's PDM algorithm and both PyAstronomy's and Astropy's Lomb-Scargle algorithms. Our distance PDM algorithm gave a period of 0.3617673 days, while the PyAstronomy PDM gave 0.3617724 days. The Lomb-Scargle algorithms both gave very different periods of near 1.83 days, possibly due to Lomb-Scargle's reliance on a sinusoidal fit. Since Kepler measured a period of 0.3617589 days, and the average period from the Python-coded and PyAstronomy PDM algorithms deviated from it by less than a second, we concluded that the period of eclipsing binary system EPIC 201826968 has not changed since Kepler's observations.

© 2020 Astronomy Theory, Observations and Methods Journal

**Keywords:** *binaries: eclipsing — methods: data analysis — techniques: photometric — telescopes*

<https://doi.org/10.32374/atom.2020.1.5>

## INTRODUCTION

An eclipsing binary is a type of binary star system whose orbital shape and inclination causes one star to block the other from Earth's perspective. These systems can be difficult to observe using traditional optical methods, as many are physically so close together that they appear as one star. Therefore, it is impossible to measure the position angle and separation of the stars in the system. However, their orbits can be analyzed by measuring changes in light intensity that occur during eclipses, when one star passes in front of the other. These data can be used to construct a lightcurve, in which normalized flux is plotted versus phase, where phase is the fraction

of orbital period elapsed. Normalized flux is used instead of light intensity in order to scale the graph so that the average flux of data points outside of the eclipse is 1. This provides a convention by which eclipsing binary systems can be easily compared to each other.

From analyzing the lightcurve, the period of an eclipsing binary system can be determined. A sample lightcurve is shown in Figure 1. Due to their small physical separation, eclipsing binaries generally have periods of less than a few days (Giuricin, Mardirossian, & Mezzetti, 1983). Repeated measurements of the system's period can help to determine its rate of change, which indicates the extent of mass

exchange between the stars (Plavec, 1970).

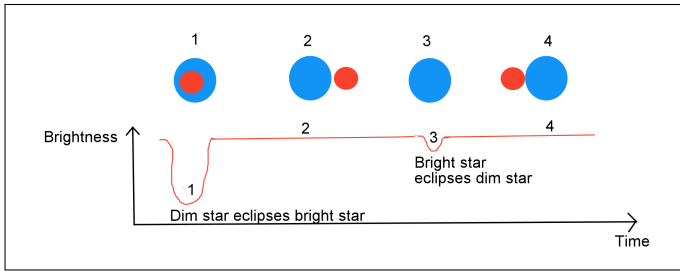


**Fig. 1.** Sample lightcurve of an eclipsing binary. The blue star is brighter than the red one.

In this paper, the eclipsing binary system EPIC 201826968 is analyzed for a change in period since its last observation. This is done by obtaining time-series images in four filters (Bessel-B, Bessel-V, SDSS-r', and SDSS-i'), creating and examining the system's lightcurve, and using period-finding algorithms such as Phase-Dispersion Minimization (PDM) and Lomb-Scargle. In the course of this examination, we also investigated the appropriateness of these algorithms for finding the periods of systems such as ours.

## ECLIPSING BINARY EPIC 201826968

Possible star systems to investigate were selected from Kepler K2 Campaign 1 (Kirk et al., 2016). Campaign 1 was chosen because it contains stars that are visible in late January and February, the time during which imaging was conducted. The eclipsing binary EPIC 201826968 was chosen: its properties are shown in Table 1. Note that two magnitudes are reported because the data in Table 1 are drawn from both the GAIA and Kepler catalogues. The GAIA satellite includes wavelengths between 300 and 1,100 nanometers (Gaia Collaboration et al., 2016), while the Kepler satellite includes a narrower range between 420 and 865 nanometers (Koch et al., 2004).

This system has a secondary eclipse with a depth comparable to that of the primary eclipse, as shown in the lightcurve in Figure 2. The similar depths of the primary and secondary eclipses indicates that the stars may be similar sizes.

## TELESCOPE METHODS

### Telescopes

The Las Cumbres Observatory (LCO) (Brown et al., 2013), which has access to 21 telescopes at 8 sites around the world, was used to image EPIC

**Table 1.** GAIA and Kepler values for EPIC 201826968 (Kirk et al., 2016; Gaia Collaboration et al., 2016)

RA (degrees)	178.3649
Dec (degrees)	+05.85937
Luminosity (solar luminosities)	1.877
Kepler Magnitude	kmag = 11.6430
Gaia Magnitude	Gmag = 11.605
Absolute G-band Magnitude	0.9540
Period (days)	0.3617589
Period Error (%)	0.004
Parallax (mas)	2.9433
Proper Motion (mas/yr)	-34.732, 0.082
Stellar Effective Temperature (K)	5355
Stellar Radius (solar radii)	1.59

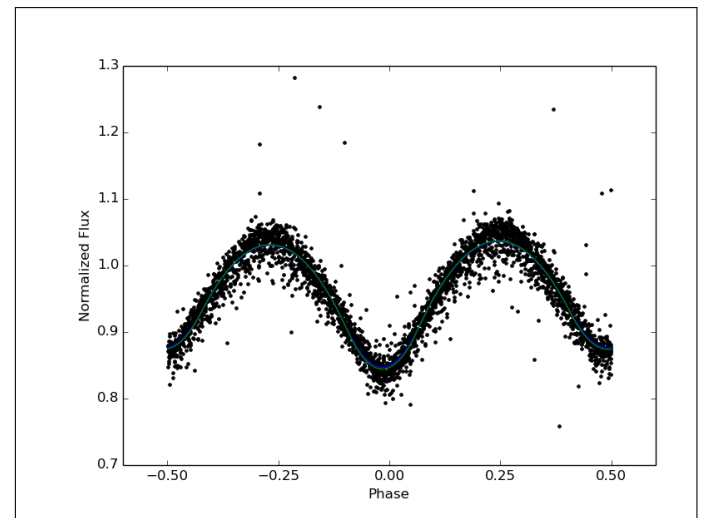


**Fig. 2.** Existing Kepler lightcurve for EPIC 201826968 (Kirk et al., 2016)

201826968 . Figure 3 shows one of the 0.4-meter telescopes in the LCO network.



**Fig. 3.** One of the 0.4-meter telescopes in the LCO network. (Brown et al., 2013)

### Exposure Times

We requested images from the LCOGT network, taken in each of four filters: Bessel-B, Bessel-V, SDSS-r', and SDSS-i'. These images can be found in [Supplemental Documents](#). To find the optimal exposure time for this system on the 0.4m LCO telescopes, source-minus-sky analog-digital unit (ADU) counts were evaluated for the star in 8 images from each of the filters, and averaged for each filter. The counts were found using [AstroImageJ](#) (AIJ) software (Collins, Kielkopf, Stassun, & Hessman, 2017). AIJ uses aperture photometry, which sums the ADU counts of each pixel, or fraction of one, within a given circular aperture surrounding the star. A wider background aperture was set around the star to determine the ADU counts of the back-

ground, which was then subtracted to determine the integrated source-minus-sky count for the star.

Choosing the exposure time so as to obtain a source-minus-sky count between 100,000 and 200,000 is a reasonable range to ensure that the images have a good signal-to-noise ratio (SNR) without being saturated (Fitzgerald et al., 2018). Initially, we had set an exposure time of 50 seconds for the blue filter, which did not have a high enough source-minus-sky value. Then, we requested new images with a modified exposure time of 90 seconds for the blue filter: all other exposure times were kept the same. This doubled the source-minus-sky value, which then fit within the desired range. Optimal exposure times and number of returned images per filter are listed in Table 2.

### Comparison Stars

Examining the stars surrounding the target in our images, we decided on 6 comparison stars, or comp stars, which were used to determine the magnitude of the eclipsing system relative to a non-variable source (Roth, 2009). We used comp stars because the target star counts might vary based on exposure time or atmospheric clarity, which would have interfered with our ability to determine the variation due to eclipses if we had used unaltered magnitudes. However, the ratio of target star ADU count to that of a nearby non-variable star in the same image would be expected to stay constant, because both stars would experience the same variation in their counts from these factors (Buchheim, 2007). This technique is called differential photometry. Additional comp stars can be used to ensure that the chosen comp stars are not themselves variable by comparing them with each other. Out of the six original comp stars, three of them had source-sky counts under 100,000, which were unsuitable for comparisons due to low SNR, and another had asymmetry that made it look like a double star. Table 3 shows the coordinates of the remaining two comp stars chosen for this study.

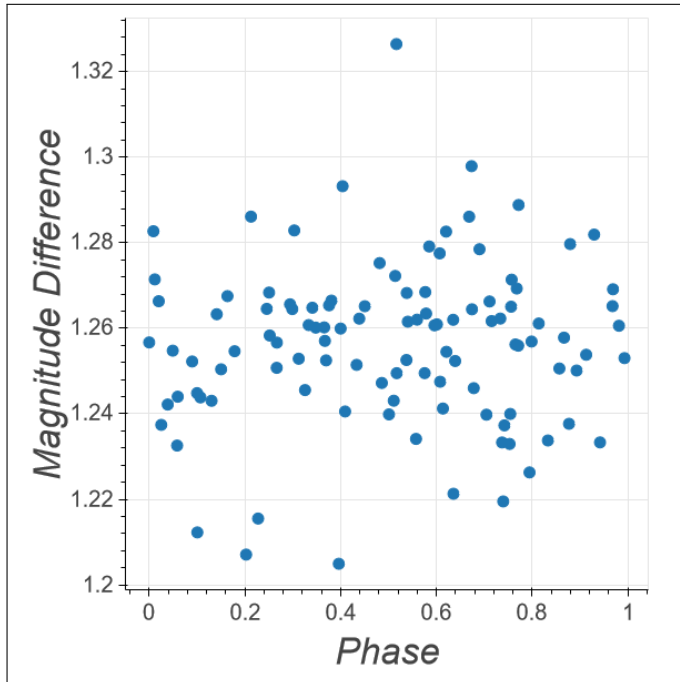
Figure 4 shows the difference between the comp stars' magnitudes: since the difference stays relatively constant over the phase of the target system, the quality of the images used and the non-variability of the comp stars can be inferred. The mean differential magnitude was 1.256, with a standard deviation of 0.019.

**Table 2. Optimal exposure times for EPIC 201826968 on the 0.4m LCO telescopes**

Filter Color	Exposure Time (seconds)	Number of Returned Images
Blue	90	116
Red	20	116
Infrared	30	97
Visible	30	111

**Table 3. Comp star coordinates**

Comp Star Number	RA (Degrees)	Dec (Degrees)
1	178.49805	5.783633
2	178.41852	5.828768

**Fig. 4.** Plot of the difference between comp star magnitudes over phase of the target system, determined using the Kepler period.

## PERIOD DETERMINATION

### Data Transformations

We took a series of images in various filters from LCO (see [Supplemental Documents](#) for the image files used). These images were processed with various photometries by the Our Solar Siblings (OSS) pipeline ([Fitzgerald, 2018](#)). We noted their modified Julian dates (MJDs) and the ADU counts of the target and comparison stars. To turn the MJDs of the observations into phase, the difference between the observation date and the initial observation date was divided by the period, and the portion after the decimal point in the quotient was retained. In other words:

$$P(D) = \frac{D - D_0}{P} \bmod 1, \quad (1)$$

where  $P(D)$  is the phase,  $D$  is the observation date,  $D_0$  is the date of the first observation,  $P$  is the assumed period, and  $\bmod$  is the remainder operator.

The differential magnitude of each observation is calculated by multiplying  $-2.5$  by the base-10 logarithm of the count of the target star divided by the count of the comparison star. This can be represented as:

$$F = -2.5 \log_{10} \frac{S_t}{S_c}, \quad (2)$$

where  $F$  is the differential magnitude,  $S_t$  is the source-minus-sky of the target star for the observation, and  $S_c$  is the source-minus-sky of the comparison star in the same observation.

Phase versus differential magnitude plots were made for all images with all filter color and photometry type combinations. Based on the plots in [Supplemental Documents](#), we determined that data taken with Bessel-B filter and sex (source extractor) photometry gave us the visually clearest lightcurves. This technique is similar to that employed by Altunin and Caputo ([Altunin & Caputo, 2019](#)). Bessel-B filter



and sex photometry were hence used in all following analysis (Bertin & Arnouts, 1996).

### Distance PDM

We coded a Python version of the PDM Minimum Distance method to estimate the period of our system based on (Dworetzky, 1983). Using an assumed period, we obtained the phase of our system based on a phase of 0 at the start date of our observations. Using our differential magnitude, calculated phase, and the distance formula for points on a 2-dimensional graph, we calculated the distance between consecutive points in flux-phase space, and added them together to get one total sum. The smaller our sum, the closer the data points are, the more accurate our lightcurve, and the closer our estimate of the period is to its actual value. For our data, the Minimum Distance algorithm gave us a closest period of  $0.3618 \pm 0.0004$  days, larger than the Kepler period by 0.73 seconds. The error was computed using the width of the primary peak at half maximum.

### PyAstronomy PDM

We used the PyAstronomy version of Wolk's Phase Dispersion Minimization (PDM) Standard Deviation algorithm as a method of estimating the period of our eclipsing binary system (Wolk, 1996; Scanner and PDM Class, accessed 2018). In this method, the phase of each observation is determined by the guessed period and the starting date of the observations. The data is then divided into 10 sections by phase (the phase bins are 0.0-0.1, 0.1-0.2,...0.9-1.0). The standard deviations of the fluxes within each bin are summed, and then divided by the standard deviation of the entire data set, yielding a quantity known as theta. The smaller the theta value, the closer the data points are to each other, and the closer its estimate of the period is to the true period of the system. For our data, the PDM Standard Deviation algorithm gave a closest period of  $0.3618 \pm 0.0004$  days, larger than the Kepler period by 1.17 seconds.

### Astropy and PyAstronomy Lomb-Scargle methods

We also used the Astropy and PyAstronomy versions of the Lomb-Scargle periodogram, originally developed independently by Lomb and Scargle (Lomb, 1976; Scargle, 1982). The Lomb-Scargle method attempts to perform a sinusoidal fit on a large set of observational data, taken over a range of times. The algorithm determines the probability, or power, of a

certain period by measuring the quality of the sinusoidal fit. The period with the largest power is thus the most likely, according to Lomb-Scargle. For our data, the Astropy version of Lomb-Scargle reported a most likely period of  $1.838 \pm 0.044$  days, greater than Kepler's by over 1.47 days. Similarly, the PyAstronomy version gave a period of  $1.832 \pm 0.013$  days, which showed a similar discrepancy from Kepler's measurement.

### Comparison of Algorithms: Periods and Statistics

As shown in Table 4, the period found by Kepler is very similar to the periods found by the Distance PDM and PyAstronomy PDM methods. However, these periods are very different from those found by both Lomb-Scargle algorithms. As explained above, for PDM-analyzed periods lower values indicate a more likely period, while for Lomb-Scargle-analyzed periods higher values indicate a more likely period as determined by the respective algorithm.

Likewise, as shown in Figure 5, the lightcurve made with Kepler's period is very similar to those with the Distance PDM and PyAstronomy PDM periods. However, both Lomb-Scargle algorithms give extremely different and noisy lightcurves.

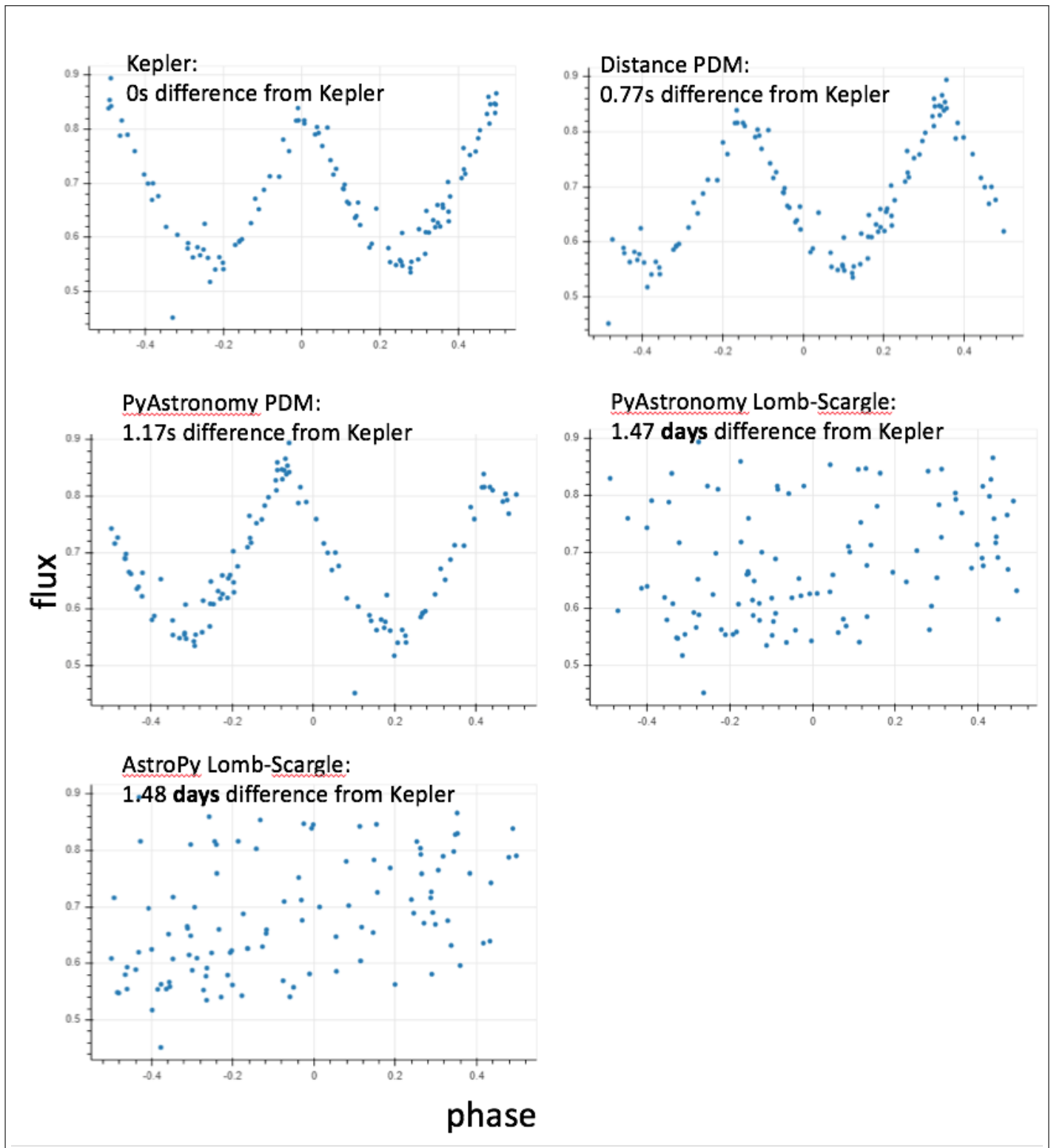
Figure 6 shows the power graph of each period-calculation method, where "power" refers to the likelihood of a given period. Both PDM methods have very clearly-defined peaks at their predicted periods and the remainder of their graphs descend to low-level noise. The power graphs of both Lomb-Scargle methods also demonstrate peaks near their predicted periods, but the peaks are quite noisy and, in the case of the AstroPy Lomb-Scargle algorithm, other similarly-large peaks also occur closer to the Kepler and PDM-derived periods.

## DISCUSSION OF RESULTS

Figures 7 and 8 and show a small selection of lightcurves from Supplemental Documents, which used images taken with various filters and photometry types to produce lightcurves of EPIC 201826968 using the Kepler period. They demonstrate that the "visually cleanest" lightcurve arises from the B filter and sex photometry types, which was the conclusion drawn in Section .

As shown in Table 4 and Figure 5, the Lomb-Scargle-derived periods and lightcurves are extremely different from Kepler's, while the PDM algorithm periods are very similar to Kepler's. Likewise, Figure 6

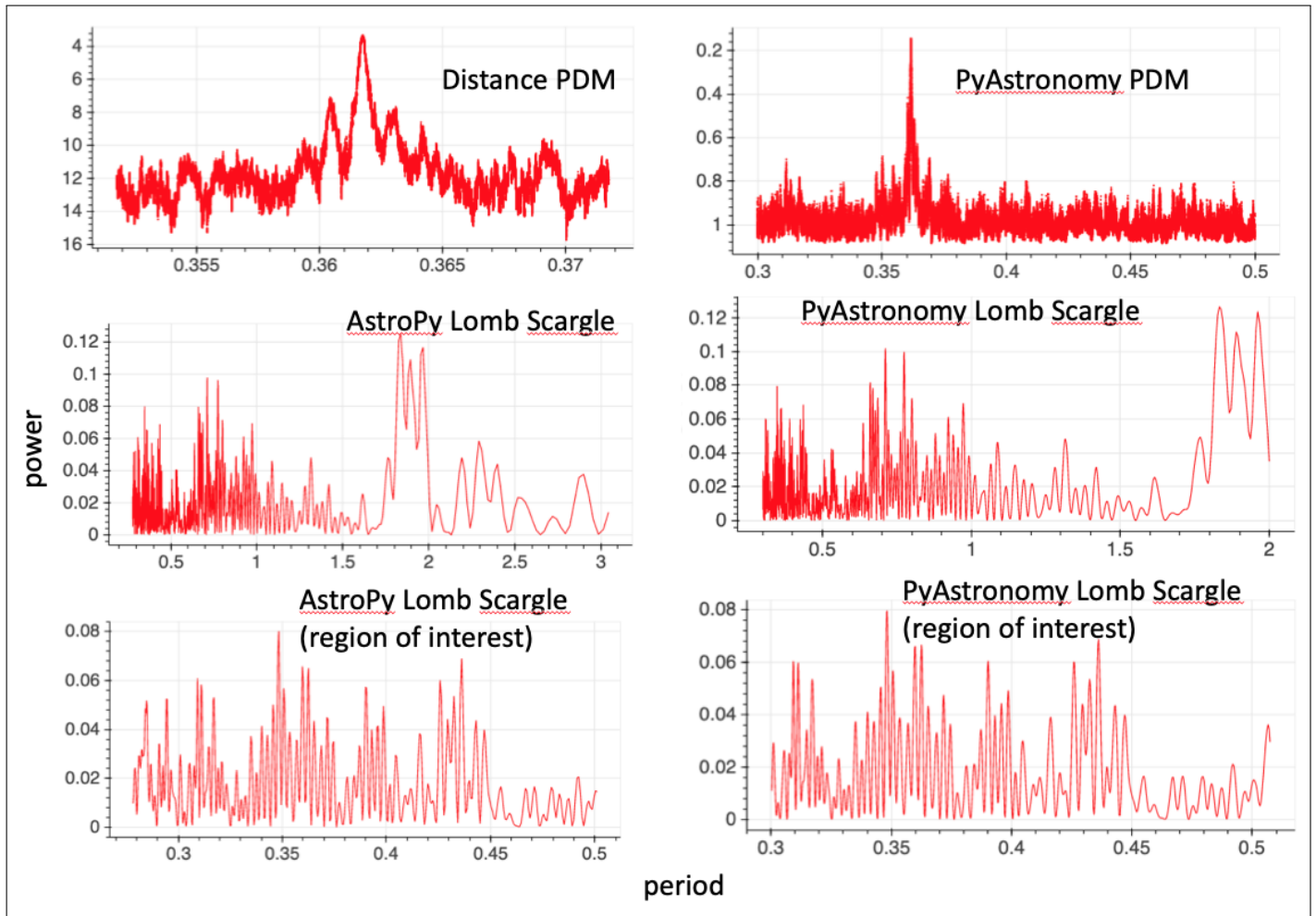




**Fig. 5.** Each period with its period difference from Kepler and a lightcurve.

**Table 4.** Each period method with its period and the measured period's statistics from other methods.

Period Method	Period (days)	Total Distance of this Period Calculated with our Images	PyAstronomy PDM Theta of this Period Calculated with our Images (10 bins)	Astropy Lomb-Scargle Power of this Period Calculated with our Images	PyAstronomy Lomb-Scargle Power of this Period Calculated with our Images
Kepler	0.3617589	3.54	0.190	0.0267	0.00561
Distance PDM	0.3617673	3.33	0.143	0.0273	0.00561
PyAstronomy PDM	0.3617724	3.47	0.143	0.0275	0.00561
Astropy Lomb-Scargle	1.8376291	10.1	0.855	0.125	0.126
PyAstronomy Lomb-Scargle	1.8321272	11.9	0.905	0.126	0.125

**Fig. 6.** Each period-calculation method with its power graph. As lower statistics for the PDM algorithms imply a greater likelihood of a correct period, the y-axes for those graphs go from higher to lower values.

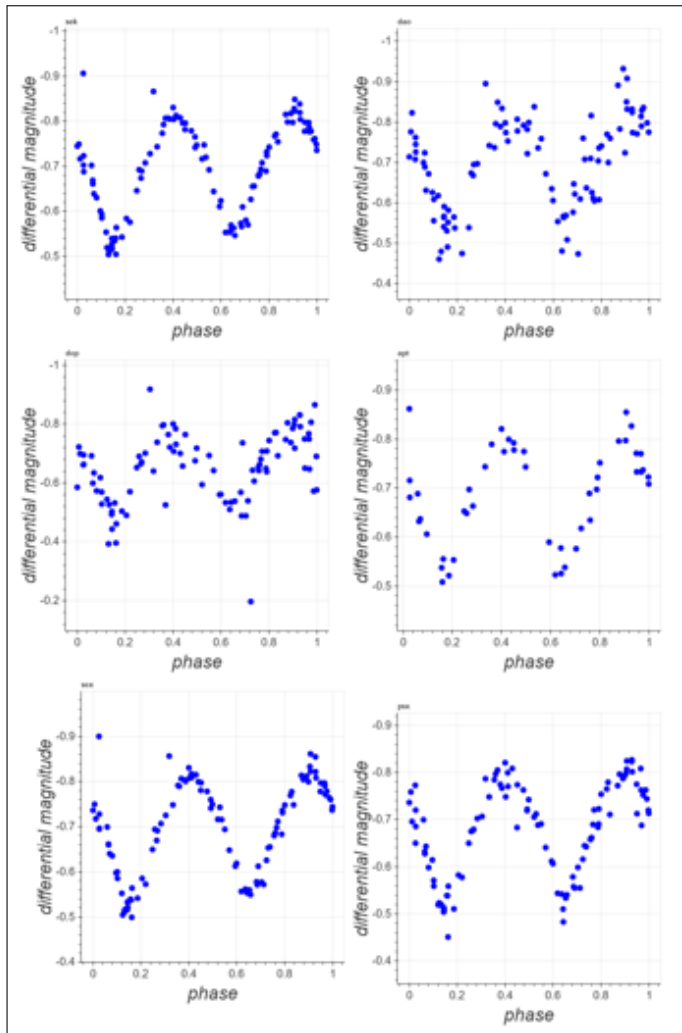


**Fig. 7.** Lightcurves using B-filter images in all six photometry types.

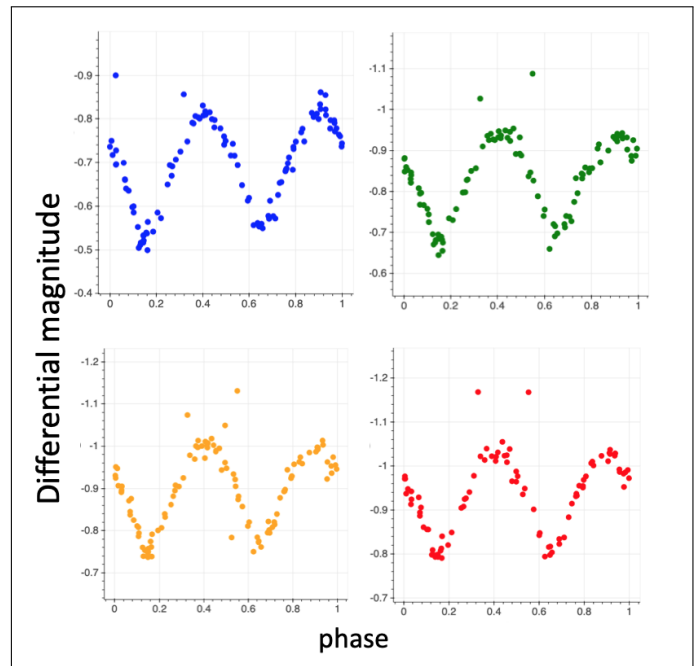


**Fig. 8.** Lightcurves using images in all four filter types processed with sex photometry.

demonstrates much cleaner power distributions for the PDM algorithms than for the Lomb-Scargle ones. Thus, Lomb-Scargle methods appear to be noisier and more inaccurate compared to the PDM methods when applied to measurements of our system. In Table 5, the period of each algorithm is shown together with its error. Except for the PyAstronomy Lomb-Scargle Algorithm, whose error was given directly by the PyAstronomy Lomb-Scargle module, the error is estimated as the full width at half maximum of the corresponding peak in the power plot. As is evident from these values, both our Distance PDM period and the PyAstronomy PDM period are not statistically different from the Kepler algorithm's period, while both Lomb-Scargle algorithms give statistically different results.

According to Lomb, the Lomb-Scargle algorithm works by “fitting sine waves by least-squares to the data” (Lomb, 1976). This statement is also reflected in the Astropy and PyAstronomy descriptions of their slightly modified Lomb-Scargle algorithms. (Mayangsari, Priyatikanto, & Putra, 2014) have determined that PDM algorithms are more accurate for systems with non-sinusoidal fits, which may be the case with EPIC 201826968. Therefore, the Lomb-Scargle algorithm's discrepancy may be explained by the non-sinusoidal nature of this system.

**Table 5. Each period method with its period and the measured period's errors.**

Period Method	Period (days)	Period Error (days)
Kepler	0.3617589	0.000016
Distance PDM	0.3617	0.0004
PyAstronomy PDM	0.3618	0.0004
Astropy	1.838	0.044
Lomb-Scargle		
PyAstronomy	1.832	0.013
Lomb-Scargle		

## CONCLUSION

Using the distance and PyAstronomy PDM methods to determine the period of EPIC 201826968, we conclude that the current period of EPIC 201826968 is  $0.36177 \pm 0.00056$  days (calculated by averaging the Distance PDM and PyAstronomy PDM periods and adding their errors in quadrature). Our period deviates from the previously recorded Kepler period by about 1 second. The Lomb-Scargle algorithm is inappropriate for determining the period of our system, possibly due to our system's non-sinusoidal lightcurve. Further observations of this system would be significantly beneficial to the scientific community to determine whether the period is changing. As of this writing, the period of EPIC 201826968 has changed by less than 48.3 seconds since the time of the observations made by the Kepler space telescope.

## ACKNOWLEDGMENTS

The advice, assistance and information shared with us by Michael Fitzgerald of [Our Solar Siblings](#) was useful to this work. This research made use of [Astropy](#), a community-developed core Python package for Astronomy ([Astropy Collaboration et al., 2013, 2018](#)). This work also made use of [PyAstronomy](#). This work makes use of observations from the LCOGT network ([Brown et al., 2013](#)). This research has made use of the [VizieR](#) catalogue access tool, CDS, Strasbourg, France. The original description of the VizieR service was published in A&AS 143, 23. This work has made use of data from the European Space Agency (ESA) mission [Gaia](#), processed by the Gaia Data Processing and Analysis Consortium ([DPAC](#)). Funding for the DPAC has been provided by national institutions, in particular the institutions participating in the Gaia

Multilateral Agreement. We would like to thank the [Las Cumbres Observatory](#) for allowing researchers to use their many telescopes, and Karen Collins for making the [AstroImageJ](#) software freely available for researchers to use. We would also like to thank the Our Solar Siblings pipeline for processing and performing photometry on all of our images.

## SUPPLEMENTAL DOCUMENTS

All supplemental documents are presented below.

See [this](#) for the images used in this project.

See [this](#) for the code used to plot the difference over phase of comp star magnitudes.

See [this](#) for lightcurves plotted with the Kepler period with all photometries and all filter types.

See [this](#) for supporting content for the lightcurve-plotting Python code.

See [this](#) for supporting content for the Distance PDM algorithm Python code.

See [this](#) for supporting content for the PyAstronomy PDM algorithm Python code.

See [this](#) for supporting content for the Astropy Lomb-Scargle algorithm Python code.

See [this](#) for supporting content for the PyAstronomy Lomb-Scargle algorithm Python code.

## REFERENCES

- Altunin, I., & Caputo, R. (2019). Period of Eclipsing Binary EPIC 201458798. *Astronomy Theory, Observations and Methods*, submitted.
- Astropy Collaboration, Price-Whelan, A. M., Sipócz, B. M., Günther, H. M., Lim, P. L., Crawford, S. M., ... Astropy Contributors (2018, September). The Astropy Project: Building an Open-science Project and Status of the v2.0 Core Package. , 156, 123.
- Astropy Collaboration, Robitaille, T. P., Tollerud, E. J., Greenfield, P., Droettboom, M., Bray, E., ... Streicher, O. (2013, October). Astropy: A community Python package for astronomy. , 558, A33.

- Bertin, E., & Arnouts, S. (1996, June). SExtractor: Software for source extraction. *Astronomy and Astrophysics Supplement Series*, 117, 393-404.
- Brown, T. M., Baliber, N., Bianco, F. B., Bowman, M., Burleson, B., Conway, P., ... Willis, M. (2013, Sep). Las Cumbres Observatory Global Telescope Network. , 125(931), 1031. doi:
- Buchheim, R. K. (2007). *The sky is your laboratory: Advanced astronomy projects for amateurs*.
- Collins, K. A., Kielkopf, J. F., Stassun, K. G., & Hessman, F. V. (2017, January). Astroimagej: Image processing and photometric extraction for ultra-precise astronomical light curves. *The Astronomical Journal*, 153. Retrieved from <http://iopscience.iop.org/article/10.3847/1538-3881/153/2/77>
- Dworetsky, M. M. (1983, June). A period-finding method for sparse randomly spaced observations or "How long is a piece of string ?". , 203, 917-924.
- Fitzgerald, M. T. (2018). The our solar siblings pipeline: Tackling the data issues of the scaling problem for robotic telescope based astronomy education projects. *RTSRE*, 1(1), 347-358.
- Fitzgerald, M. T., McKinnon, D. H., Danaia, L., Cutts, R., Salimpour, S., & Sacchi, M. (2018). Our solar siblings. a high school focussed robotic telescope-based astronomy education project. *RTSRE*, 1(1), 221-235.
- Gaia Collaboration, Prusti, T., de Bruijne, J. H. J., Brown, A. G. A., Vallenari, A., Babusiaux, C., ... Zschocke, S. (2016, Nov). The Gaia mission. , 595, A1. doi:
- Giuricin, G., Mardirossian, F., & Mezzetti, M. (1983, March). The period distribution of eclipsing binary systems. , 119, 218-226.
- Kirk, B., Conroy, K., Prša, A., Abdul- Masih, M., Kochoska, A., Matijević, G., ... Borucki, W. (2016, March). Kepler Eclipsing Binary Stars. VII. The Catalog of Eclipsing Binaries Found in the Entire Kepler Data Set. , 151, 68. doi:
- Koch, D. G., Borucki, W., Dunham, E., Geary, J., Gilliland, R., Jenkins, J., ... Weiss, M. (2004, Oct). Overview and status of the Kepler Mission. In J. C. Mather (Ed.), (Vol. 5487, p. 1491-1500). doi:
- Lomb, N. R. (1976, February). Least-Squares Frequency Analysis of Unequally Spaced Data. , 39, 447-462.
- Mayangsari, L., Priyatikanto, R., & Putra, M. (2014). On the period determination of asas eclipsing binaries. *AIP Conference Proceedings*, 1589(1), 37-41.
- Plavec, M. (1970). Mass exchange in binary stars. *Publications of the Astronomical Society of the Pacific*, 82(489), 957-995. Retrieved from <http://www.jstor.org/stable/40676541>
- Roth, G. D. (2009). *Handbook of practical astronomy. Scanner and PDM Class*. (accessed 2018). Retrieved from <https://www.hs.uni-hamburg.de/DE/Ins/Per/Czesla/PyA/PyA/pyTimingDoc/pyPDMDoc/classes.html>
- Scargle, J. D. (1982, December). Studies in astronomical time series analysis. II. Statistical aspects of spectral analysis of unevenly spaced data. , 263, 835-853.
- Wolk, S. J. (1996). *Phase Dispersion Minimization*. Retrieved from <http://hea-www.harvard.edu/~swolk/thesis/period/node2.html>



# Photometric Determination of the Distance to the RR Lyrae LP Cam.

**BRIAN UZPEN<sup>1,2,\*</sup> AND TIMOTHY F. SLATER<sup>2</sup>**

<sup>1</sup>Natural Sciences Department, Laramie County Community College, 1400 E. College Drive, Cheyenne, WY 82007

<sup>2</sup>School of Teacher Education, College of Education, 1000 E. University Avenue, Laramie, WY 82071

\*Corresponding author: buzpen@gmail.com

Photometric observations of the nearby RR Lyrae, LP Cam, were obtained to verify that the period-luminosity relationships are still valid for RR Lyrae stars with improved parallaxes as part of a larger study. Using both obtained photometry and archival data, photometric distance estimates were made to LP Cam. When accounting for independently measured values of interstellar reddening, the photometric distance determined for LP Cam is not in agreement with the parallactic distance. The likely causes for this mismatch are explored and could be due to greater extinction than measured or incorrect measured effective temperatures from spectral energy distributions. An additional cause could be due to a faint proximate source to LP Cam. When  $E(B - V)$  is changed such that the variance in distance measured between the three filters is minimized, an estimate of  $E(B - V) \approx 0.24$  is achieved with distance estimates of  $V: 780 \pm 40\text{pc}$ ,  $i: 793 \pm 41\text{pc}$ ,  $z: 792 \pm 38\text{pc}$  which compares reasonably well with the GAIA value of  $809 \pm 20\text{pc}$

© 2020 Astronomy Theory, Observations and Methods Journal

**Keywords:** Stars: Variable: RR Lyrae, techniques: photometric, catalogs, parallaxes

<http://dx.doi.org/etc>

## INTRODUCTION

RR Lyrae stars are low-mass horizontal branch stars with short periods of pulsations less than a day. These stars play an invaluable role in understanding the distances of our Universe and are one of several standard candles used to set the distance scale within astronomy. However, it wasn't until Longmore et al. (1986) that the period-luminosity relationship of RR Lyrae stars could be leveraged to determine extragalactic distances. With the advancements of computational stellar photospheric models, Catelan et al. (2004) and Cáceres & Catelan (2008) were able to derive theo-

retical relationships for the absolute magnitude of RR Lyrae stars in common broadband filters. With the increasingly precise parallax measurements of surveys, such as GAIA (Gaia Collaboration et al., 2018), it has yet to be determined whether the distances for the brightest RR Lyrae using the well established relationships of Cáceres & Catelan (2008) and Catelan et al. (2004) are in agreement with the distances determined via GAIA's parallax measurements. The aim of this study is to obtain period relationships in  $B$ ,  $V$ ,  $i$ , and  $z$  filters to determine the distances to the star photometrically and make sure these distances are in



agreement with the distance from parallax measurements.

## OBSERVATIONS/METHODS

We scheduled 57 cadence observations using the Las Cumbres Observatory Network between September 26–October 9, 2019 in Johnsons  $B$  and  $V$  and SDSS  $i$  and  $z$  filters. We were able to obtain 47 images during this window. These observations of the variability of LP Cam allow us to determine the period through generating lightcurves, verify the temperature and luminosity of the star using color relationships, and in combination with previously measured archival values determine the distance to the star.

### Image Processing

Images were processed using the *OSS* pipeline (Fitzgerald, 2018), which includes basic image processing such as cropping, flat fielding and cosmic ray reduction. The *OSS* pipeline also performs photometric source extraction and both aperture photometry or point-spread photometry using algorithms such as DAOPhot (Stetson, 1987). Photometric reduction algorithms were performed on all images in each of the bandpasses. The data was further analyzed via Astropy-based python scripts called *astrosource* that calibrates the sources through identification of the least variable stars in the field, determines their apparent magnitude and then determines the period of the RR Lyrae. With redder filters, fewer comparison stars were identified with 27 stable comparison stars in  $B$ , 25 in  $V$ , 46 in  $i$ , and only 31 in  $z$ . Results for the calibrated apparent magnitude of the LP Cam lightcurves in each bandpass using PSF photometry are shown in Table 1.

Filter	Mag	e(Mag)
$B$	12.248	0.045
$V$	11.322	0.044
$i$	10.795	0.050
$z$	10.661	0.037

**Table 1. Calibrated Apparent Magnitudes.** The calibrated magnitudes of LP Cam from PSF photometry in each filter along with measured uncertainties.

## RESULTS

### RR Lyrae Verification

It is not uncommon for variable stars to be misidentified in the literature. As a check, we used  $B - V$  and the estimated maximum extinction from the *Dust Calculator* using the method of Schlafly & Finkbeiner (2011), to estimate the luminosity and effective temperature of the star. The estimated maximum reddening is  $E(B - V) = 0.6554 \pm 0.0278$ . We determined the luminosity using the relationship in Equation 1.

$$\text{Log} \frac{L_*}{L_{\text{solar}}} = \frac{-(B - V) - 4.77}{2.5} \quad (1)$$

The effective temperature was estimated using both the non-reddened and reddened ( $B - V$ ) relationships using Equation 2 (Ballesteros, 2012).

$$T_{\text{eff}} = \left( \frac{1}{0.92(B - V) + 1.7} + \frac{1}{0.92(B - V) + 0.62} \right) * 4600 \quad (2)$$

The results are summarized in Table 2 and show that LP Cam clearly occupies a position in the HR Diagram indicative of being an RR Lyrae star.

	$(B - V)$	$\text{Log} \frac{L_*}{L_{\text{solar}}}$	$\text{Log} (T_{\text{eff}})$
Non-Reddened	0.926	1.538	3.69
Reddened	0.313	1.783	3.87

**Table 2. Effective Temperature and Luminosity**

We present the maximum and minimum possible extinction values to the RR Lyrae LP Cam. Regardless of the level of reddening, LP Cam occupies a space in the HR Diagram consistent with RR Lyrae stars.

### Period Determination

The period in each of the filters was determined using both the Phase Dispersion Minimization method (PDM) (Stellingwerf, 1978) and the String-Length method (SL) (Lafler & Kinman, 1965). The results for each of the filters are reported in Table 3 in days. The residuals of the fit using both methods are shown in Figure 1 and 2, respectively. The lightcurves for all four bandpasses are shown in Figures 3, 4, 5, and 6.

## DISCUSSION

### Photometry

Due to the relative brightness of LP Cam there are a multitude of observations to compare our measurements with. Photometric measurements from this

Filter	PDM (days)	e(PDM) (days)	SL (days)	e(SL) (days)	Amp (mags)
<i>B</i>	0.5729	0.0086	0.5730	0.0093	0.973
<i>V</i>	0.5729	0.0091	0.5734	0.0082	0.760
<i>i</i>	0.5691	0.0100	0.5688	0.0072	0.489
<i>z</i>	0.5692	0.0121	0.5771	0.0100	0.461

**Table 3. Period Determination.** The period was determined using both the PDM and SL methods. The periods are in good agreement with each other. The amplitude of the light curve in each filter is provided in the last column.

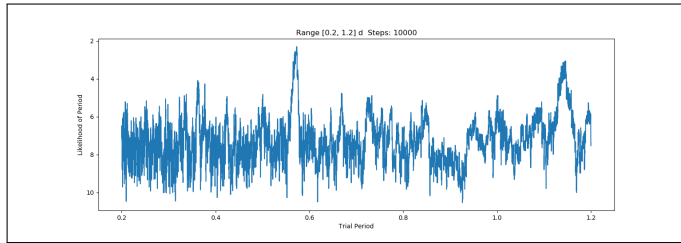


**Fig. 1.** The probability plot for LP Cam's phase using the String-Length method. The is a very strong likelihood of the period at just under 0.6 days with next strongest peak at double the period.

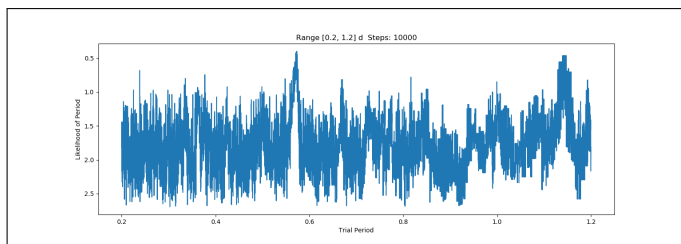


**Fig. 2.** The probability plot for LP Cam's phase using the Phase-dispersion minimization method. The is a very strong likelihood of the period at just under 0.6 days with next strongest peak at double the period, similar to the SL method.

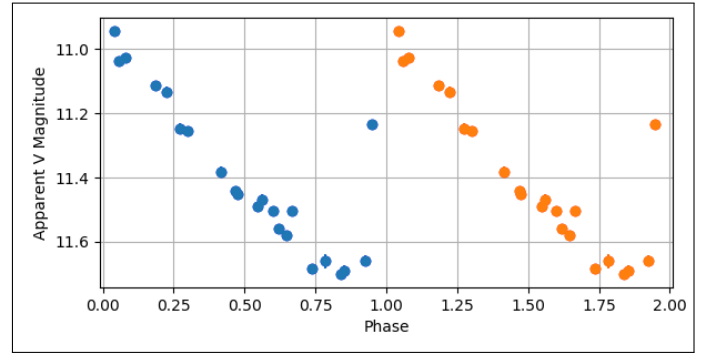


**Fig. 3.** A phased light curve for LP Cam in the *V* band using the PDM period. Given that both the SL and PDM period are equivalent within uncertainties a solution using the SL period is not presented. The data are well-matched to a period of  $0.5729 \pm 0.0091$  days.

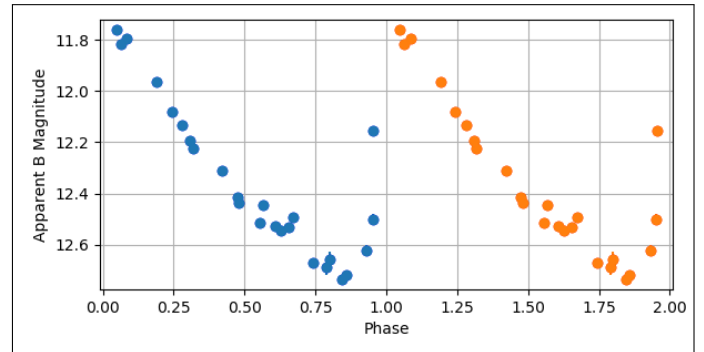


**Fig. 4.** A phased light curve for LP Cam in the *B* band using the PDM period.

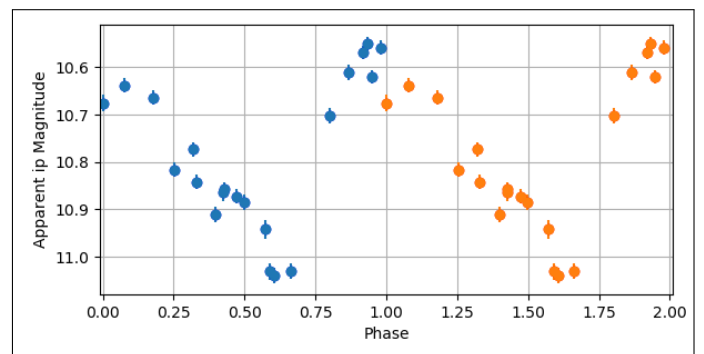


**Fig. 5.** A phased light curve for LP Cam in the *i* band using the PDM period.

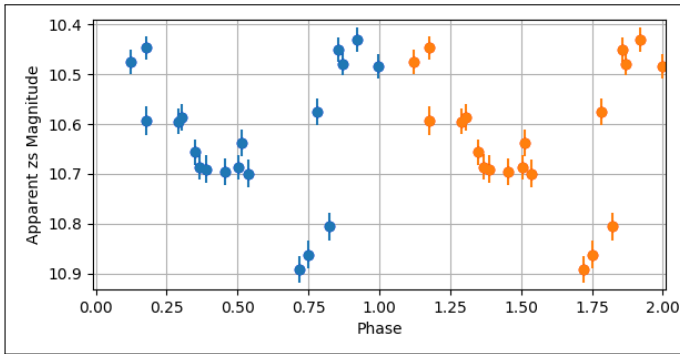


**Fig. 6.** A phased light curve for LP Cam in the  $z$  band using the PDM period.

study are compared to literature values (with uncertainties when available) from both compiled catalogs, such as the AAVSO All-Sky Photometric Catalog (APASS, [Henden et al., 2015](#)), (All-Sky, [Kharchenko, 2001](#)), and (Panstarss, [Flewelling et al., 2016](#)) and previous studies of RR Lyraes, such as [Kinemuchi et al. \(2006\)](#). The results of the comparison are shown in Table 4. In general, the optical measurements of this study using PSF photometry agree with the literature values within uncertainties, with the exception of  $V$  from [Kinemuchi et al. \(2006\)](#). The near-infrared measurements appear to be systematically brighter at  $i$  than those in the literature. Upon inspection of the literature, it was found that [Flewelling et al. \(2016\)](#) detected a faint source within one arcsecond in  $r$  and  $i$  bands. As a test, aperture photometry was compared to the literature values and the aperture values agree better with those previously detected. However, given the proximate nature of this faint source, PSF photometry would be the correct approach to minimize errors for stars in a crowded field and we therefore adopt the values determined from PSF photometry for the remaining analysis (e.g., [Janes & Heasley, 1993](#)). It is important to note that the faint source was not detected in the  $g$  and  $z$  filters in the Panstarrs data set and is not detected in our relatively short exposures of LP Cam using the LCO 0.4m telescopes.

### Period

Using all four filters, the mean period was found to be  $0.5716 \pm 0.0050$  days using the PDM method and  $0.5731 \pm 0.0043$  days using the SL method. Both values are consistent with one-another. A comparison of the results for the period of pulsation is shown in Table 5 and our values agree with those in the literature with the exception of the mid-infrared study done by

[Gavrilchenko et al. \(2014\)](#). The difference between the optical and near-infrared measurements may be a result of the decrease in amplitude as the wavelength increases for these types of stars. However, without reported uncertainties it is difficult to determine if this period is truly different than the other reported values.

### Distance

The purpose of this study is to determine if period-luminosity relationships from [Catelan et al. \(2004\)](#) [Cáceres & Catelan \(2008\)](#) agree with GAIA DR2 parallax measurements for the brightest RR Lyrae. To determine the photometric distance to this star we used the measured PSF photometric values in  $V$ ,  $i$ , and  $z$ , the metallicity of the star from Fourier coefficients of 0.03 [Gaia Collaboration et al. \(2018\)](#) and an estimated reddening value. As previously stated, the maximum assumed reddening is  $E(B - V) = 0.6554$ . The results for each of the filters is provided in Table 6. This maximum value provides a minimum distance of  $517 \pm 16$  pc and a maximum distance of  $1013 \pm 32$  pc. However, a better estimate of reddening can be made by passing photometric measurements through a spectral energy distribution (SED) and determining the best fit. [Pickles & Depagne \(2010\)](#) performed this measurement and determined that LP Cam is best fit by a G5III spectrum, which corresponds to a  $T_{eff} \simeq 5010$  K and  $E(B - V) = 0.04$ . [McDonald et al. \(2017\)](#) also measured  $T_{eff}$  using archival data and stellar atmospheric models at  $5036 \pm 182$  K, which corresponds to about 0.07 magnitudes of uncertainty. The resulting distance measurement using SED fitting for extinction and the relationships of [Catelan et al. \(2004\)](#) and [Cáceres & Catelan \(2008\)](#) is  $971 \pm 57$  pc. The measured distance from [Gaia Collaboration et al. \(2018\)](#) is  $809 \pm 20$  pc. These two derived measurements are not in agreement. In order for our photometric measurements to match this distance, the reddening to LP Cam must  $E(B - V) \simeq 0.24$  magnitudes. Using  $E(B - V) = 0.24$ , we find that the distance using each individual bandpass and their weighted average all overlap with the measured GAIA distance with variance between the photometric data and parallactic data minimized. Thus, we adopt an  $E(B - V)$  value of 0.24 for LP Cam. Furthermore, it is important to note that [Gavrilchenko et al. \(2014\)](#) using mid-infrared data determined a distance of  $843 \pm 14$  pc for the distance to LP Cam, which is in agreement with the GAIA measured dis-

Study	$B$	$e(B)$	$V$	$e(V)$	$i$	$e(i)$	$z$	$e(z)$
	(mag)	(mag)	(mag)	(mag)	(mag)	(mag)	(mag)	(mag)
This Study	12.248	0.045	11.322	0.044	10.795	0.050	10.661	0.058
This Study-Aperture			11.418	0.052	10.890	0.050	10.627	0.037
APASS	12.113	0.474	11.251	0.261	10.664	0.179		
All-Sky	12.295		11.611					
Panstarrs					10.951		10.692	
Kinemuchi et al. (2006)			11.43					

**Table 4. Photometry Comparison.** The calibrated measured photometry from this study compared to values within the literature. Within uncertainties, the values from this study agree with those from the literature using aperture photometry. However, PSF photometry, which we argue is the correct approach, is noticeably brighter in  $V$  and  $i$  than Panstarrs, All-Sky and Kinemuchi et al. (2006).

Study	Period	$e(\text{Period})$
	(days)	(days)
This study	0.5716	0.0050
Watson et al. (2006)	0.5720300000	
Kinemuchi et al. (2006)	0.57205	
Maintz (2005)	0.572092000	
Gavrilchenko et al. (2014)	0.5840	

**Table 5. Period Comparison.** The period of pulsation from this study is compared to those of previous studies. In general, there is good agreement between the measured values of this study and those of previous studies. The exception is the mid-infrared period of Gavrilchenko et al. (2014). The difference in observed period may be due to the decrease in amplitude as the wavelength increases for these types of stars.

tance and extinction decreases with increasing wavelength bolstering the argument to adjust  $E(B - V)$  from the maximum value. Also of note, is that if this analysis were repeated using aperture instead of PSF photometry, the measured distance would increase slightly and still not be in agreement with the measured parallactic distance using reddening values determined from  $T_{eff}$  archival data or maximum interstellar reddening. Aperture photometry would require an even greater extinction in order to agree with the parallactic distance than our adopted value of  $E(B - V) = 0.24$ .

## CONCLUSION AND IMPLICATIONS

Using the relationships of Catelan et al. (2004) and Cáceres & Catelan (2008), the minimum distance to LP Cam is  $517 \pm 16$  pc with a maximum distance of  $1013 \pm 32$  pc. These distances are highly dependent upon interstellar reddening values. Using previously determined values of interstellar reddening of  $E(B - V) = 0.04$  from SED fitting (Pickles & Depagne, 2010), we find the mean distance of LP Cam using all four bandpasses to be  $971 \pm 57$  pc. This measured distance is not in agreement with measured parallax from Gaia Collaboration et al. (2018). The difference between these measurements could be due to errors in archival photometric measurements for this source. LP Cam has a faint proximate source that has been detected in some of the filters in the Panstarrs dataset. Depending upon the type of photometric extraction of the data, the light from this star could be affecting short exposures of LP Cam and subsequent SED fit-

$E(B - V)$	$V$	$e(V)$	$i$	$e(i)$	$z$	$e(z)$	Mean $e$	(Mean)
	(pc)	(pc)	(pc)	(pc)	(pc)	(pc)		
0.6554	431	27	529	27	592	28	517	16
0	1099	68	1002	52	938	44	1013	32
0.24	780	48	793	41	792	38	788	24
0.04	1038	133	963	92	912	72	971	57

**Table 6. Distance Comparison.** Using the relationships of Catelan et al. (2004) & Cáceres & Catelan (2008), the minimum average photometric distance to the star is  $517 \pm 16$  pc, while the maximum distance is  $1013 \pm 32$  pc. Neither of these measurements are in good agreement with the parallactic measurement from *GAIA* DR2 of  $809 \pm 20$  pc. Using the synthetically derived  $T_{eff}$  measured from McDonald et al. (2017) & Pickles & Depagne (2010) the distance to LP Cam is overestimated when comparing to the distance from *GAIA*.

ting that was used to estimate a reasonable value for interstellar extinction. Spectroscopic measurements should be conducted of LP Cam to determine the temperature (and subsequent) extinction to LP Cam. An interstellar reddening value of  $E(B - V) = 0.024$  would result in the distances determined using period-luminosity relationships of Catelan et al. (2004) and Cáceres & Catelan (2008) agreeing with the measured *GAIA* values of distance for LP Cam with a mean derived photometric distance of  $788 \pm 24$  pc. Furthermore, the faint source proximate to LP Cam should be investigated for the possibility of binarity. Few RR Lyraes reside in binary systems (e.g., Hajdu et al., 2015) and this object presents a rare opportunity to determine key stellar parameters (such as mass) for a unique proximate standard candle.

## REFERENCES

- Ballesteros, F. J. (2012, feb). New insights into black bodies. *EPL (Europhysics Letters)*, 97(3), 34008. Retrieved from <https://doi.org/10.1209/0295-5075/97/34008> doi:
- Cáceres, C., & Catelan, M. (2008). The period-luminosity relation of rr lyrae stars in the sdss photometric system. *The Astrophysical Journal Supplement Series*, 179(1), 242. Retrieved from <https://doi.org/10.1086/591231>
- Catelan, M., Pritzl, B. J., & Smith, H. A. (2004). The rr lyrae period-luminosity relation. i. theoretical calibration. *The Astrophysical Journal Supplement Series*, 154(2), 633. Retrieved from <https://doi.org/10.1086/422916>
- Fitzgerald, M. T. (2018). The our solar siblings pipeline: Tackling the data issues of the scaling problem for robotic telescope based astronomy education projects. *RTSRE*, 1(1), 347–358.
- Flewelling, H. A., Magnier, E. A., Chambers, K. C., Heasley, J. N., Holmberg, C., Huber, M. E., ... Shiao, B. (2016, Dec). The Pan-STARRS1 Database and Data Products. *arXiv e-prints*, arXiv:1612.05243.
- Gaia Collaboration, Brown, A. G. A., Vallenari, A., Prusti, T., de Bruijne, J. H. J., Babusiaux, C., ... Zwitter, T. (2018, Aug). Gaia Data Release 2. Summary of the contents and survey properties. , 616, A1. Retrieved from <https://doi.org/10.1051/0004-6361/201833051>
- Gavrilchenko, T., Klein, C. R., Bloom, J. S., & Richards, J. W. (2014, Jun). A mid-infrared study of RR Lyrae stars with the Wide-field Infrared Survey Explorer all-sky data release. , 441(1), 715–725. Retrieved from <https://doi.org/10.1093/mnras/stu606>
- Hajdu, G., Catelan, M., Jurcsik, J., Dékány, I., Drake, A. J., & Marquette, J.-B. (2015, 03). New RR Lyrae variables in binary systems. *Monthly Notices of the Royal Astronomical Society: Letters*, 449(1), L113–L117. Retrieved from <https://doi.org/10.1093/mnrasl/slv024>
- Henden, A. A., Levine, S., Terrell, D., & Welch, D. L. (2015, Jan). APASS - The Latest Data Release. In *American astronomical society meeting abstracts #225* (Vol. 225, p. 336.16).
- Janes, K. A., & Heasley, J. (1993). Stellar photometry software. *Publications of the Astronomical Society of the Pacific*, 105(687), 527. Retrieved from <https://doi.org/10.1086/133187>
- Kharchenko, N. V. (2001, Oct). All-sky compiled catalogue of 2.5 million stars. *Kinematika i Fizika Nebesnykh Tel*, 17(5), 409–423.



- Kinemuchi, K., Smith, H. A., Woźniak, P. R., McKay, T. A., & ROTSE Collaboration. (2006, Sep). Analysis of RR Lyrae Stars in the Northern Sky Variability Survey. , 132(3), 1202-1220. Retrieved from <https://doi.org/10.1086/506198>
- Lafler, J., & Kinman, T. D. (1965, Jun). An RR Lyrae Star Survey with the Lick 20-INCH Astrograph II. The Calculation of RR Lyrae Periods by Electronic Computer. , 11, 216. Retrieved from <https://doi.org/10.1086/190116>
- Longmore, A., Fernley, J., & Jameson, R. (1986). Rr lyrae stars in globular clusters: better distances from infrared measurements? *Monthly Notices of the Royal Astronomical Society*, 220(2), 279–287. Retrieved from <https://doi.org/10.1093/mnras/220.2.279>
- Maintz, G. (2005, Oct). Proper identification of RR Lyrae stars brighter than 12.5 mag. , 442(1), 381-384. Retrieved from <https://doi.org/10.1051/0004-6361:20053230>
- McDonald, I., Zijlstra, A. A., & Watson, R. A. (2017, Oct). Fundamental parameters and infrared excesses of Tycho-Gaia stars. , 471(1), 770-791. Retrieved from <https://doi.org/10.1093/mnras/stx1433>
- Pickles, A., & Depagne, É. (2010, Dec). All-Sky Spectrally Matched UBVRI - ZY and u g r i z Magnitudes for Stars in the Tycho2 Catalog. , 122(898), 1437. Retrieved from <https://doi.org/10.1086/657947>
- Schlafly, E. F., & Finkbeiner, D. P. (2011). Measuring reddening with sloan digital sky survey stellar spectra and recalibrating sfd. *The Astrophysical Journal*, 737(2), 103. Retrieved from <https://doi.org/10.1088/0004-637X/737/2/103>
- Stellingwerf, R. F. (1978, Sep). Period determination using phase dispersion minimization. , 224, 953-960. Retrieved from <https://doi.org/10.1086/156444>
- Stetson, P. B. (1987). Daophot: A computer program for crowded-field stellar photometry. *Publications of the Astronomical Society of the Pacific*, 99(613), 191. Retrieved from <https://doi.org/10.1086/131977>
- Watson, C. L., Henden, A. A., & Price, A. (2006, May). The International Variable Star Index (VSX). *Society for Astronomical Sciences Annual Symposium*, 25, 47.



# Guidelines for TESS Aperture Photometry via AstroImageJ

JEREMY HA<sup>1,\*</sup> AND PAT BOYCE<sup>2</sup>

<sup>1</sup>San Dieguito Academy High School, Encinitas, California, United States of America

<sup>2</sup>Boyce Research Initiatives and Research Foundation, San Diego, California, United States of America

\*Corresponding author: jeremyjha@gmail.com

Observing exoplanets with small telescopes can be a challenging but rewarding undertaking. With the advent of the Transiting Exoplanet Survey Satellite (TESS), a student observer can become qualified to participate in this exciting MIT-led NASA program to make significant contributions to exoplanet science. This paper presents the experiences and recommendations for a student to the complete observation data required for the **Ground-Based Subgroup 1 TESS Follow-up Observing Program (TFOP)**. A training plan is provided along with various websites and instructional documents. Explanations on how apply the AstroImageJ (AIJ) software and procedures are described in *A Practical Guide to Exoplanet Observing* (Conti, 2018). Data is collected from Las Cumbres Observatory (LCO) and calibrated through the OSS Pipeline. This paper deals exclusively with LCO processes and also describes how to prepare the twelve files required for submission to the Exoplanet Follow-up Observing Program for TESS (ExoFOP – TESS). The *AstroImageJ Guide for LCO - TESS Observations* (Boyce et al., 2019) that incorporates the latest *TFOP SG1 Observation Guidelines* (Conti, 2019) is also referenced.

© 2020 Astronomy Theory, Observations and Methods Journal

**Keywords:** MIT TESS – methods: differential photometry, data analysis – techniques: transit modeling – software: AstroImageJ

<https://doi.org/10.32374/atom.2020.1.7>

## INTRODUCTION

This paper addresses the data reduction of TESS exoplanet observations from the Las Cumbres Observatory that are processed through the OSS Pipeline (Fitzgerald, 2018) for submission to the TESS ExoFOP. This process can be convoluted and arduous, which is where this paper's purpose lies. It supplements the already existing guides on data reduction with counseling on the clearest, most efficient ways to un-

dertake data reduction. As such, this paper should be used in conjunction with the aforementioned guides as it assumes general knowledge of the TESS reduction process and its respective vernacular. For the same reason, AstroImageJ (AIJ) is the photometry software utilized in this paper. This paper will address the TESS steps chronologically. Image titles are censored as mandated by TESS publication policies.

## BACKGROUND

TESS is on the [cutting edge of exoplanet research](#). The mission's goal is to deliver fifty Earth-like planets. With such a grand objective, the novelty of this exciting data benefits thousands of scientists all over the world. The possibilities of the data are endless. As such, research foundations such as the [Boyce Research Initiatives and Research Foundation \(BRIEF\)](#) are so vital to TESS as they provide the education necessary to train the next generation of scientists who will unpack the mysteries within the data.

BRIEF is a member of the SubGroup1 (SG1) for the TESS. In April 2018, when the NASA/MIT team launched TESS with its first year's survey being in the southern skies, BRIEF students were already preparing to perform exoplanet transit data reduction by the use of discovery surveys (KELT, K2). BRIEF is a global Sky Partner for LCO ([Brown et al., 2013](#)) that robotically operates 0.4m telescopes sited at three observatory locations in the southern and northern hemisphere. These LCO systems with 6303 SBIG CCDs are well suited to making light curve measurements down to a light curve depth of about five parts per thousand reduction in the star's stellar flux. By the fall of 2018, BRIEF was making TESS observations for the students to perform the data reduction on to submit to the Exoplanet Follow-Up Observing Program (TESS ExoFOP).

The mission of the SG1 worldwide group of ground-based small telescope observers is to, as described by [TFOP](#), "identify false positives due to nearby eclipsing binaries that contaminate the TESS image of a candidate transiting planets." These false positives are common because the TESS images are taken with a resolution of 21 arcseconds per pixel. Often there is light flux from several stars that could create the observed light curve falling on or near that large TESS pixel. Therefore SG1 observers use ground-based telescopes to take higher resolution images in order to discern which star(s) are causing the light curve and recommend their nature. Once a star and the light curve created by the exoplanet is vetted by SG1, the candidate is then observed by the subsequent subgroups using means that are ever more sophisticated. All five subgroups compose a winnowing process that aims to reach the TESS program's goal, fifty rocky planets for future study.

In order to streamline the data reduction process, BRIEF uses the Our Solar Siblings (OSS) Pipeline. The OSS Pipeline further calibrates the CCD images,

removes artifacts such as cosmic rays, and plate solves each image.

In a similar vein, after the initial TESS observations in late 2018, Dr. Conti and the TESS program management developed two important enhancements needed for the TESS ExoFOP SG1 data submissions. The first is a macro incorporated into AIJ that facilitates the measurement of the potential false positive light sources to assess their influence on the light curve. The second is the [TFOP SG1 Observation Guidelines](#), a thorough statement of the requirements for submitting data to the TESS Follow-up Observing Program (TFOP).

Lastly, using the tools and procedures outlined by Dr. Conti's AAVSO course as well as his [Practical Guide to Exoplanet Observing](#) as a foundation, BRIEF has developed a newer guide. It incorporates the more recent developments specific to TESS observations, notably the AIJ macro, the TFOP SG1 Observations Guidelines, and the OSS Pipeline. The current "AIJ Guide for LCO – TESS Observations" defines the procedures referenced in this paper and is available for download at BRIEF's [website](#).

## PREPARATION PHASE

AIJ frequently changes and updates its software, so when AIJ is first opened, the system should be updated to Daily Build. The current Daily Build version of AIJ allows users to use its automated NEB (Nearly Eclipsing Binary) function that will come in handy later on. It's a quick step that will save a lot of time.

While working through the analysis, the TESS Transit Finder (TTF) (Figure 1) comes up a lot. It is a web based tool and database for finding information on exoplanet candidates that TESS has discovered—containing important information that will be used throughout the analysis. The TTF will be the single most important resource while conducting this analysis, so it's important to understand the information it contains before the analysis begins. To help make the analysis run smoother, data is documented from the TTF onto a blank template to organize all the data. Figure 2 shows a sample TTF Organization Sheet.

When the images are imported, make sure "virtual stack" is selected. This ensures that AIJ operates on large data sets without running out of memory, speeding up the process of importing the images.

After the images are imported, an important first step is to go through the images to weed out "bad" images, such as images that have random streaks

Local evening date	Name	TOI	V mag	T mag	Start—Mid—End	Duration	BJD <sub>TDB</sub> start—mid—end	Elev. at start, mid, end	Az. at start, mid, end	HA at start, mid, end	RA & Dec (J2000)	Period (days)	Depth (ppt)	Priority	R <sub>planet</sub> (R <sub>⊙</sub> )	Comments
Sun. 2019-02-10: Nautical twilight 2019-02-10 21:30 — 2019-02-11 06:24 local time / 2019-02-11 00:30 — 2019-02-11 09:24 UTC																
Sun. 2019-02-10 (local date)	<a href="#">Add to TOC</a> Finding charts: <a href="#">Annotated SkyMap</a> , Info: <a href="#">ExoFOP K2</a> , <a href="#">Simbad</a> , <a href="#">Gaia</a> , <a href="#">MAST</a> , <a href="#">All apertures</a> , <a href="#">TIC</a> , <a href="#">VSX</a> , <a href="#">Vizier phot.</a> , <a href="#">Airmass plot</a> , <a href="#">ACP plan</a>		12.62		03:35 — 04:19 — 05:03 ± 0:16	1:28	8525.650 8525.680 8525.711	42°, 43°, 41°	12°, 358°, 344°	-0.6, +0.1, +0.9	08:51:32.35 +17:19:11.4	1.11	7.9	4	8.8	event on target and/or check for faint NEBs within 2' and bright NEBs within full FOV
Nautical twilight 00:30 — 09:24 (UTC)			Moon 32% @100°	11.77												

**Fig. 1.** TTF information for a TESS object of interest.

	A	B	C	D	E	F	G	H
1	<b>FOR TESS / LCO OBSERVATION</b>			<b>Exoplanet:</b>				
2				<b>Observer:</b>				
3	<b>This worksheet can be used for observation runs from LCO 0.4m telescopes and processed through OSS</b>							
4	from the TTF page and ExoFOP; get to correct ExoFOP page via link on the TTF page							
5	from the observatory or FITS header of the images							
6	from camera manufacturer and / or observatory							
7	calculations from the Ohio State online calculator; necessary star data may not be available							
8	calculated fields, do not over-write with data							
9								
10	<b>Item</b>	<b>Host Star/Exoplanet Information:</b>		from the TTF page and ExoFOP - get to ExoFOP from TTF page link				
11	1	RA:			TTF			
12	2	Dec:			TTF			
13	3	Period (days):			TTF	+/-	+/- % variance	
14	4	R <sub>z</sub> :			ExoFOP		#DIV/0!	
15	5	T <sub>eff</sub> :			ExoFOP		#DIV/0!	
16		TESS (T) mag			ExoFOP or TTF			
17		Fe/H (Metallicity)			ExoFOP			
18		log(g)			ExoFOP			
19	6	V mag:			TTF			
20		Suggested range of comp stars:		-0.44 to 0.75 mag				
21	7							
22								
23	8	Date of Observation (UT):						
24		Image cadence for observation			(calculate from the run time and # of images)			
25					<b>HJD_UTC (or BJD_TDB)</b>			
26	9	Ingress:						
27	10	Egress:						
28		Predicted midpoint:			0.00000			
29	11	Model fit midpoint (T <sub>c</sub> ) in HJD_UTC (or BJD_TDB):				TTF		
30		Approximate difference:				minutes		
31	Following data is completed for LCO 0.4m telescope:				LCO Telescopes: <a href="https://lco.global/observatory/status/">https://lco.global/observatory/status/</a>			
32	Observing Location:				See LCO Decoder Ring if unsure			
33	12	Latitude:			from FITS header or LCO			
34	13	Longitude:			from FITS header or LCO			
35	14	Altitude (m):			from FITS header or LCO			
36	15	Aperture (mm):			409	from FITS header or LCO		
37	16	Focal length (mm):			4064	per Meade		

**Fig. 2.** TTF information sheet to organize the TTF data.

or particles across them, or images that are blurry or misaligned with other images. An image with unwanted particles is shown in Figure 3). It also helps to use the two sliders (min and max) at the bottom of the screen to increase the brightness of the image via changing the contrast. To do this, locate the “peak” of the histogram on the bottom of the screen and place the two markers right around it (make sure under Scale, uncheck “use fixed min and max histogram values”). This will improve the readability of the image and help determine its quality. Figures 4 and 5 show a sample image before and after its saturation is improved.

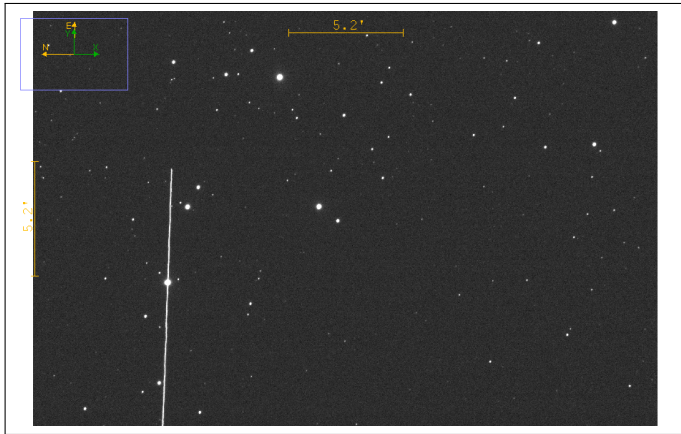


**Fig. 3.** Streaks like the one shown above are satellite trails.

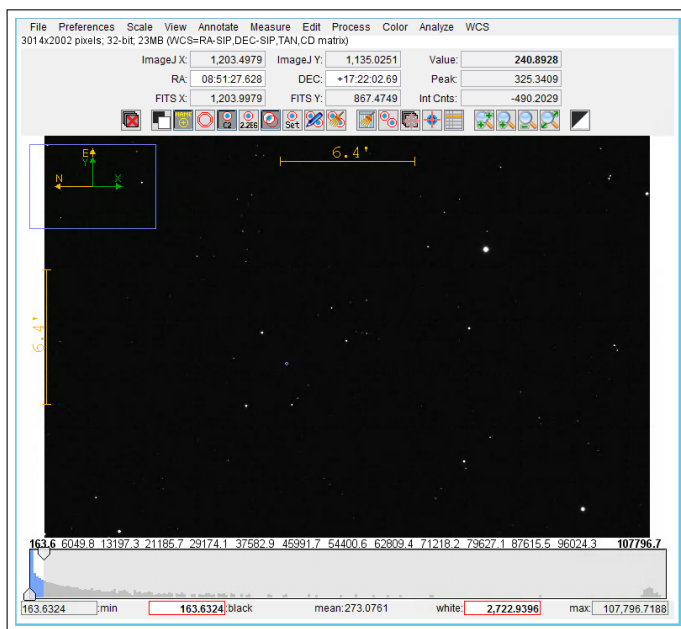


**Fig. 4.** Before utilizing the saturation scale: The image is very dark and essentially unreadable.

## CALIBRATION PHASE

The images are calibrated in order to place the FITS header information onto the images so that the images' TTF data can be inputted into AIJ in later parts of the analysis.

Firstly, the copies of the science images should be used (as opposed to the original files) because often, especially when first learning the process of TESS analysis, mistakes are made. For example, the calibration phase may be done incorrectly or the wrong images may be "quarantined." To mitigate these risks, it is prudent to use the copies of the science images.

After selecting the “DP” icon on the AIJ toolbar, locate and select the “wrench.” This is the General FITS Header. Next, select the “edit” box on the main image profile, and then locate the “edit FITS header” window as well. Note that the FITS header isn't actually being edited. Instead, the “edit FITS Header” table must be checked to see if it matches up with the General FITS Header that pops up when the “wrench” is selected. For example, if Target Name and Keyword, Target RA Keyword, Target DEC keyword, etc. match up for both headers, AIJ will correctly use these keywords to find information about the images when they calibrate (Figure 6). If the keywords don't match, AIJ won't be able to find the necessary information and will not be able to properly complete the calibration. If this is the case, then edit the information on the General FITS Header to match those on the “edit FITS Header.”

The choice of “negate” for “Observatory Longitude” in the “FITS Header Input Settings” comes down to the location of the observatory where images were taken. If the observatory was west of the prime meridian and east of the international dateline (location can be found in FITS Header editor), then its longitude should be negative. Thus, if the FITS header displays longitude as a positive number, then the “negate” box should be clicked to indicate to AIJ that the number found in the FITS header should really have a negative sign associated with it. Observatory Latitude negate box should be unchecked.

These FITS headers contain “Right Ascension and Declination (RA and DEC)” keywords. RA and DEC make up the coordinate system of the sky. RA runs east-west while declination runs north-south. Their units are degrees, minutes, and seconds (the degree is too big of a unit to measure distances in the sky, so it needed to be split further).

For further clarification, “BJD TDB” stands for



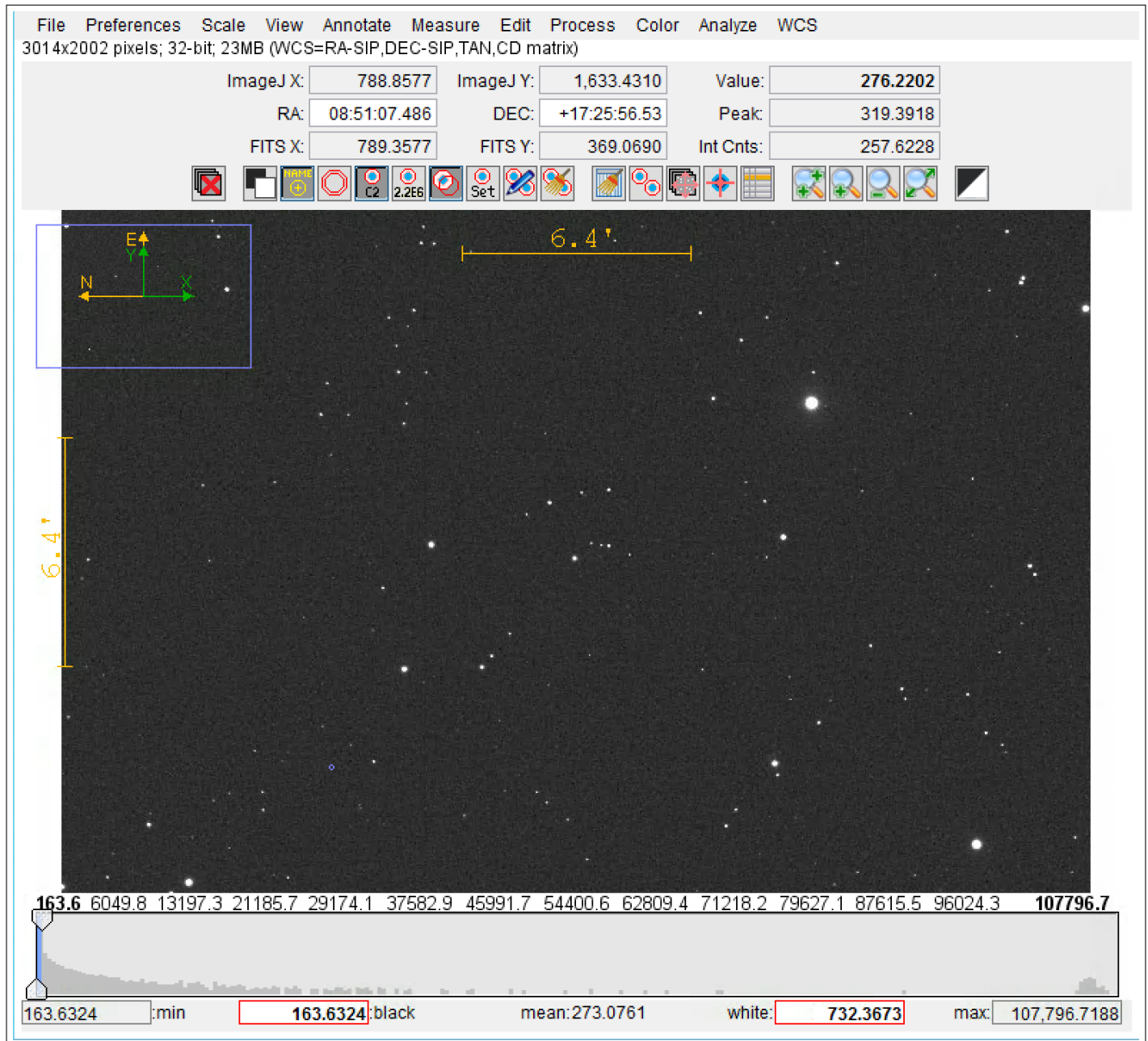


**Fig. 5.** After utilizing the saturation scale: The image is brighter and luminous sources are more visible.



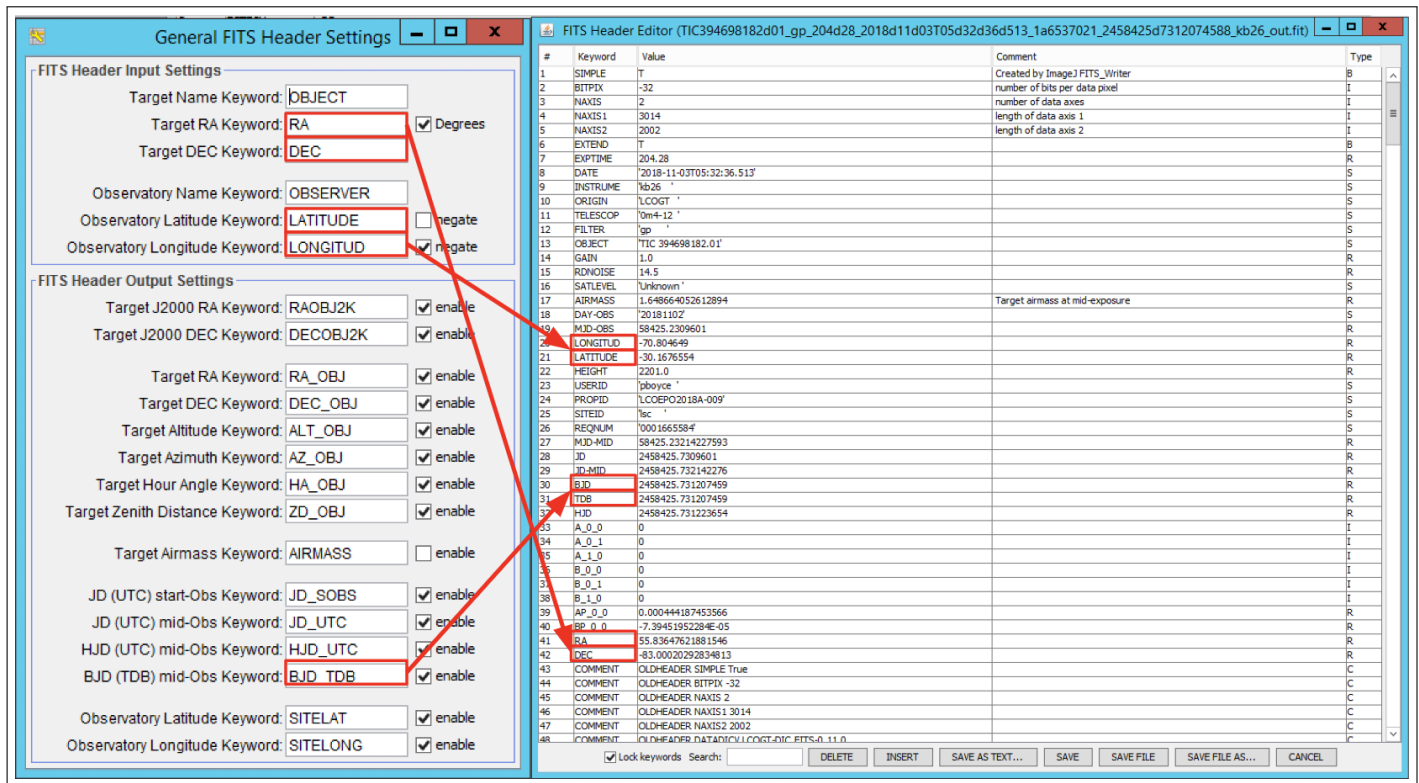


**Fig. 6.** Make sure that the keywords on both the "General" and "Edit" FITS Header Keywords match up.

“Barycentric Julian Date, Barycentric Dynamical Time.” It’s the standard time system for this exoplanet analysis, so make sure that this is enabled on the General FITS Header Settings.

Lastly, if the “Target Airmass Keyword” is disabled when the images already have data for Airmass, AIJ will override the data, creating all kinds of mistakes. For most users, there will almost always be Airmass data since most "fits" images have the Airmass header item. As such, “Target Airmass Keyword” (Figure 7) can be un-checked.

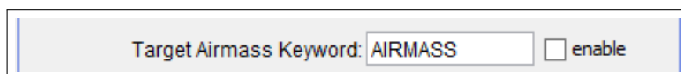


**Fig. 7.** This setting is disabled.

Since the OSS Pipeline already plate-solved the images, “plate-solved” should be unchecked on the CCD Data Processor. Furthermore, on “Target Coordinator Source” and “Observatory Location Source,” selecting “FITS Header target RA/DEC (J2000)” and “FITS header latitude and longitude.” This basically tells AIJ that the necessary data is already on the FITS header. Usually this will be the case and other options won’t need to be selected and this data won’t need to be

manually inputted. Also, make sure the polling interval is set to 0 since AIJ doesn’t need to be working in "real-time." In "real-time," non-zero polling interval values are used and images are imported throughout the exoplanet analysis process.

Finally, after hitting START, the calibration of the images will begin, and a log should show the process. If successful, the log will say “finished” and the calibrated files will be in a folder that’s inside the folder of the uncalibrated images.

Lastly, image orientation has some significance when submitting to Exo-FOP TESS: North should be up and East should be left. If this is not the case, open the first calibrated image, go to VIEW (on the top bar menu), and select Invert X or Invert Y, (or both, if necessary) until the correct orientation is obtained. Sometimes though, this problem of North and East alignment may be a problem with the telescope used for imaging. For example, North might be lined up in the negative x direction of the CCD detector, leaving no way to align North on top and East on the left or right. In this case, it’s acceptable to put North to the left and East pointing down. This is a nuanced problem, so depending on who reviews the analysis, this may or may not be considered.

## DIFFERENTIAL PHOTOMETRY PHASE

One of the most important aspects of the Differential Photometry Phase is the ra.dec aperture file created from GAIA data. Steps on how to import this file can be found on Dennis Conti's *TFOP SG1 Observation Guidelines*. Essentially, this Gaia file finds all the stars in a 2.5 arcsecond circle of the target star, which allows the AIJ macro to check and see if these stars caused the TESS detection—most often these checks determine whether or not these stars are NEBs.

However, while the Gaia file checks for stars in this circle, this circle still needs to be manually created in order for it to show up on the image. First drag the ra.dec file onto the image. Then right click the target star. A box with settings will pop up. Figure 8 shows the correct input settings.

**Fig. 8.** These settings will create the correctly sized "annotation circle" to be used in the differential photometry phase.

The following steps describe how to select comparison stars.

1. Crosshairs are unselected because they might get in the way of the stars. Then click the "multi-aperture photometry" button to open the aperture settings. If the "More Settings" button is selected, then the circle will disappear so the circle will need to be created again (basically, make sure all the Aperture Settings are established before creating the circle).
2. "Use previous X apertures" should be selected, but not "Use RA/DEC..." because AIJ automatically loads in the apertures created from the Gaia database.

3. Next, "Set Apertures" should be chosen. The field will show up again and select the target star. This will show the GAIA stars only, labeled with "T's."
4. Resume by selecting the comparison stars. Comparison ("comp") stars' peak counts (essentially how "bright" the star is) should be around that of the target star's. Comp stars should have about 8,000 peak counts and not more than 50,000 peaks counts. Figure 10 illustrates this notion of selecting comp stars based on their peak counts values.

At least six comp stars are necessary for analysis. Six is usually an adequate number as it leaves room for error in case a comp star's relative flux or other data comes out unusable for further analysis. Comp stars with similar peak values are the most desirable. However, if the number of viable comp stars "run out" before selecting six, which is usually the case, continue to select comp stars that are both above and below the target's peak value so that the data balances out (Figure 9). Lastly, while the preferred method is to use the comp stars' brightnesses to determine their selectability, be aware that there have been recent developments regarding alternative methods. Specifically, some cite using the stars' spectrums instead of their brightnesses.

Once the Differential Photometry phase has concluded, make sure a screenshot of the image with the 2.5 arcsecond circle, all the comp stars, as well as all the Gaia-generated stars is taken. The screenshot is one of the required TESS SG1 files for data submission. This can be done by either manually doing it using the computer's respective function, or by going to file, saving the image as a png, and selecting the "AIJ analysis" folder as its destination. Make sure that the file truly goes there, as AIJ can sometimes be clunky completing steps like these.

## TRANSIT MODELING PHASE

First, the plot configuration ([blank plot configuration template](#)) is a life-saving file when it comes to the Transit Modeling Phase. It saves the settings of an entire plot—curves, labels, etc. As more analyses are completed, this file becoming increasingly important because it allows a researcher to easily go back and edit their plot and its settings without having to replot it from scratch. This can be extremely tiresome and inefficient. Thus, when starting new plots, use

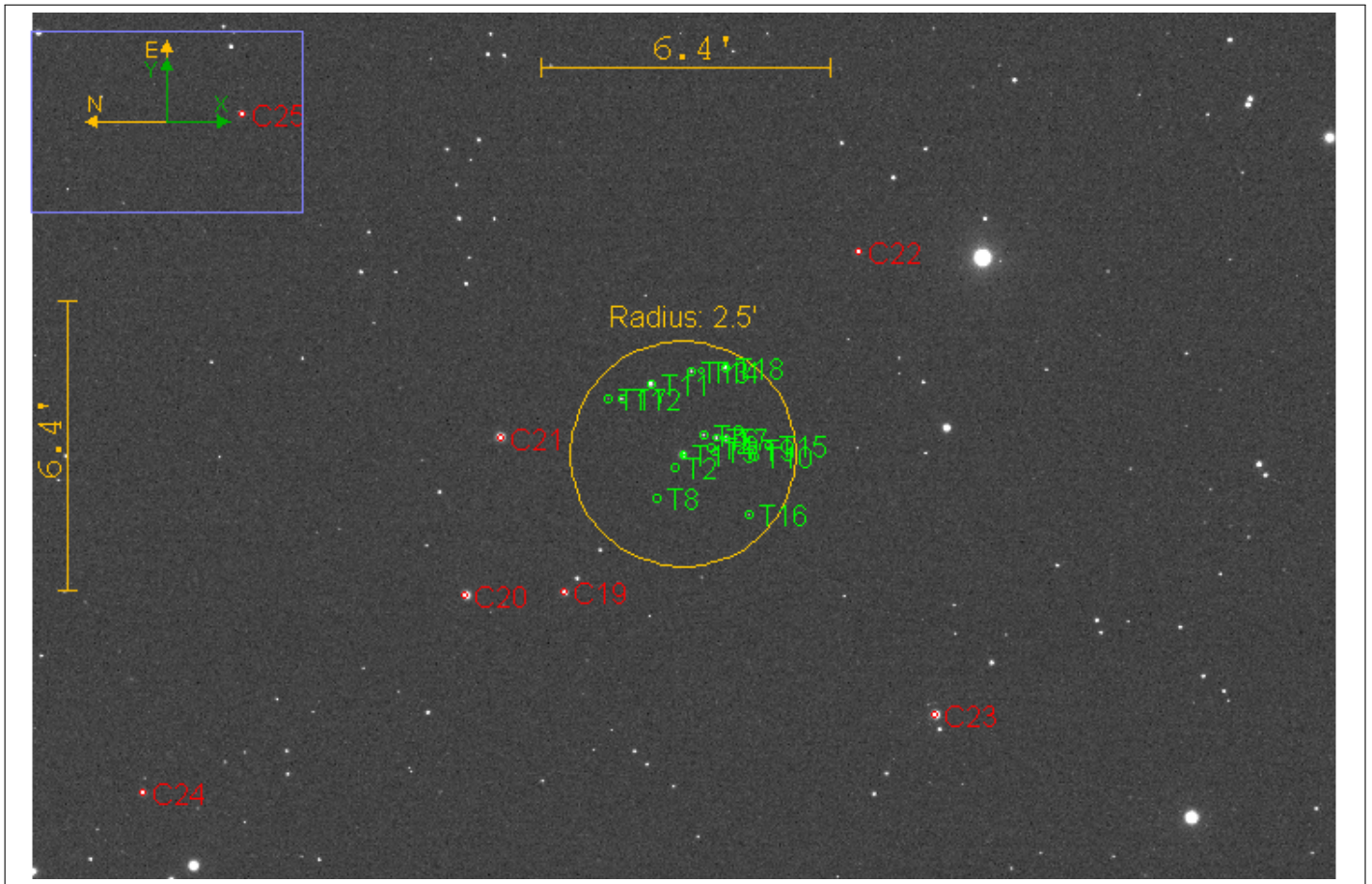


**Fig. 9.** This image shows the selection of reasonable comp stars as well as a 2.5 arcsecond circle around the target star, of which contains possible NEB's as documented by GAIA.



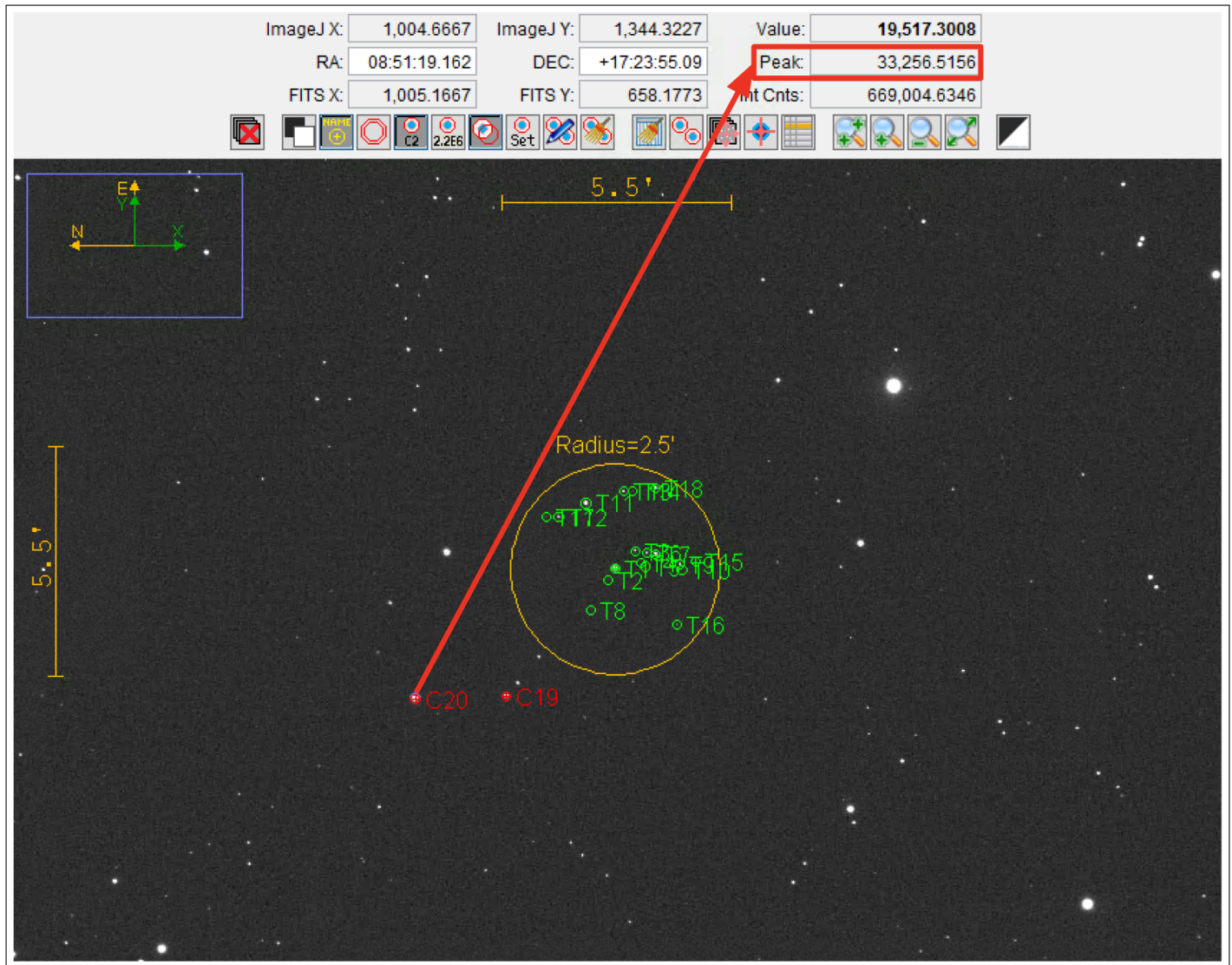


**Fig. 10.** In this case, the Target Star (T1) had a peak value of about 20,000 counts. Since no comp stars had 20,000 counts, comp stars should be chosen where the average of them is near 20,000. C20 and C19 were chosen as comp stars since peaks values were 30,000 counts and 11,000 counts, respectively. Accurate data analysis doesn't require peak values to be perfectly aligned since the data is rarely is.

a [blank plot configuration template](#) so that data can be simply inputted without having to undo previous data. Also remember to save the plot configuration files during/after the process so that the plots can easily be updated even after closing AIJ.

When plotting curves, more often than not, there will be errors. For example, if the curve has outliers and certain data points need to be removed from the light curve, (though it should be kept as even poor data points are useful) there's a technique that can be used to fix it. First, note the BJD TDB (closest approximation) time for the outlier, then go to the sorted measurements table and look at the rows with that BJD TDB time. Next, select the row that has the T1 Rel Flux outlier data and delete it. Then rerun the Transit Modeling Phase. It should not take long since most of the last settings will have remained. Looking at Table 1, Slice (image) 63 would be removed.

**Table 1. Sample Data That Depicts an "Outlier" Plot Due to extraneous Rel. Flux.**

Slice	BJD TDB	Airmass	rel flux T1
19	2458525.604898	1.6973	0.114635
41	2458525.605605	1.708598	0.114128
57	2458525.607008	1.698978	0.114462
63	2458525.607715	1.694244	0.74451
88	2458525.60841	1.689581	0.114248
99	2458525.609117	1.685014	0.115208

Another method to consider when creating light curves has to do with the Multi-Plot Reference Star Settings (Figure 11). These settings deselect a comp star, thereby excluding it from the photometric analysis (model fitting). This can be particularly helpful if a comp star's data points are extremely erratic. Upon deselecting a comp star, the respective comp star become a "target" star, and the field of view will reflect this change. Furthermore, the light curves of all the other comp and target stars will become more or less fitted, as shown on the light curve. If light curves become less fitted, un-plotting a star via the Multi-Plot Y Data Screen may be a better option than using the Multi-Plot Reference Star Settings.

A small, yet interesting part of the transit modeling phase has to do with the ingress and egress times. Why are only the decimals inputted into AIJ and not

the full ingress and egress BJD TDB times? First, the ingress and egress represent the start and end times of a transit (when the exoplanet begins orbiting in front of the host star and after it orbits out of the host star's surface). The TTF only shows the last seven digits (including three decimals) of ingress and egress. The full time is listed on the FITS header. These times usually have the same integer values, which is why AIJ needs only their decimal values. However, sometimes the egress ends on the next day (one unit larger than the ingress). In this case, the egress values should be inputted as 1.XYZ as opposed to 0.XYZ.

Furthermore, the ingress and egress are significant because sometimes the predicted ingress and egress will be different than the observed ingress and egress times. To determine the observed ingress and egress times, use the x-values of the half-way points from the vertical predicted ingress line and the beginning of the flat horizontal line on the curve (do this for both predicted ingress and egress times). A difference between the predicted and observed ingress and egress usually means that the predicted time of transit is inaccurate; this should not have huge implications for determining false positives. Differences will affect the width of the light curve, however. (Figure 12).

In terms of general strategy to optimize efficiency during the Transit Modeling Phase, a useful technique is the "Half and Half Screen" (Figures 13 and 14) technique with the Plot of Measurements Screen and the Multi-Plot Y-Data Screen.

Basically, to see the Multi-Plot Y-Data screen's settings change in real time, split both screens in half so that they're next to each other. This allows for clear tracking of which settings correspond to which plots, reducing the chance of error.

Furthermore, for the Scale and "Then Shift" settings of the target stars on the Multi-Plot Y-Data screen, it is best to have them both be at Scale 1. However, this may not be enough to show any real dip or curvature. Thus, a higher scale factor can be used as long as both rel flux T1 plots have the same Scale factor. The same applies to the comp stars, except that often times the comp stars won't have dips, so extremely high scale factors aren't as necessary.

Aesthetics have a significant place in this process. The plots that are created need to be read by future researchers, meaning that there's a standard of quality and readability that needs to be upheld. It's often best to keep light curves (and other lines) vertically dis-



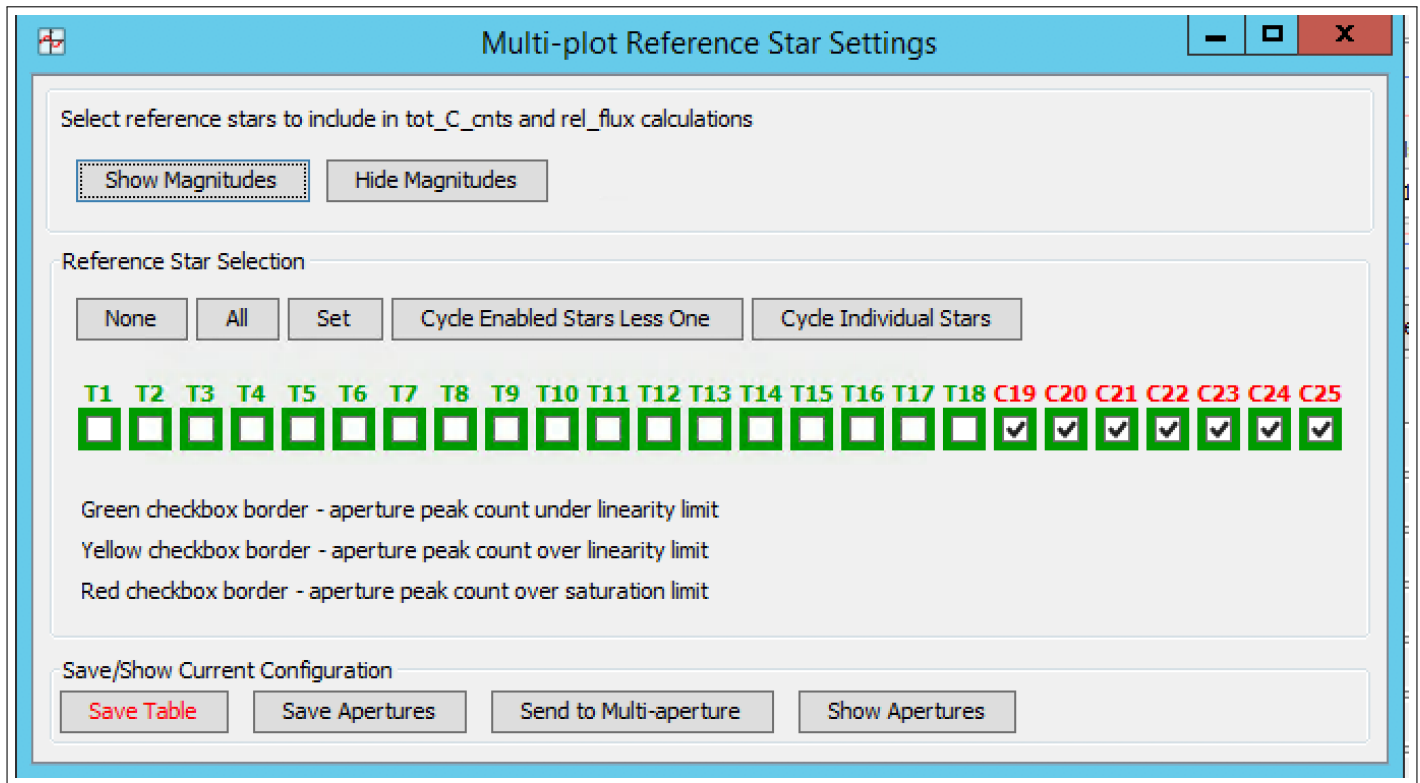


**Fig. 11.** Shown are 18 target stars and 7 comp stars. By deselecting one of the comp stars, it will subsequently become a target star, and will be excluded from the model fitting.

tanced from each other. The target star's light curves should be plotted on the horizontal lines marked by the y-axis in order to distinguish any dips that they might have. Also, a separate plot should be made for the comp stars as it'll expand the target star's plots, making the depth more visible. Figure 15 and its complementary comp star graph shown in Figure 16 show what a submitted light curve should look like in terms of readability.

Thus, one of the light curve plots should only have the target star's light curves and X(FITS) T1, Y(FITS) T1, tot C cnts, AIRMASS, Sky/Pixel T1 and Width T1 plots. The other plot should have just the comp stars (only about four or five are necessary for plotting). The comp stars that are selected for plotting should be the ones that don't change in brightness during the observation and that have the smallest variation. This can be seen by how well a comp star's plots match up with its "line of best fit" (Figure 18).

An important aspect of the Transit Modeling Phase is the Data Set 2 Fit Settings (Figure 17). Here, various information can be inputted to improve the accuracy of the light curve. For example, the period and estimated radius of the host star are information from the TTF that can be inputted here. The "Host Star

Parameters" are used to estimate the radius of the exoplanet. Limb darkening (LD) coefficients can also be inputted. LD coefficients are calculated using the [LD calculator](#), where Fe/H (Iron to Hydrogen ratio) and  $\log(g)$  (the surface gravity of a celestial object measured in  $\text{cm/sec}^2$  expressed as a log of base 10) of a particular TESS object of interest (TOI) can be found on the [ExoFOP - TESS Database](#). If these two pieces of data are not available, 0.3 is used for both LD coefficients.

There are a variety of beautiful colors on the Multi-Plot Y-Data Screen. For target and comp stars, choose the colors freely (with reason: try to avoid making all the comp stars the same color). However, there are some specific [color coordination procedures](#) that must be followed. They only apply to non-target, non-comp star plots.

## CASE STUDIES/ANALYSIS OF LIGHT CURVES

After the light curve has been created, the next step is to classify what kind of planet or host star has been analyzed. This part of the analysis is nuanced and is often regarded as the most difficult because it requires experience and well-justified subjectivity. In this next

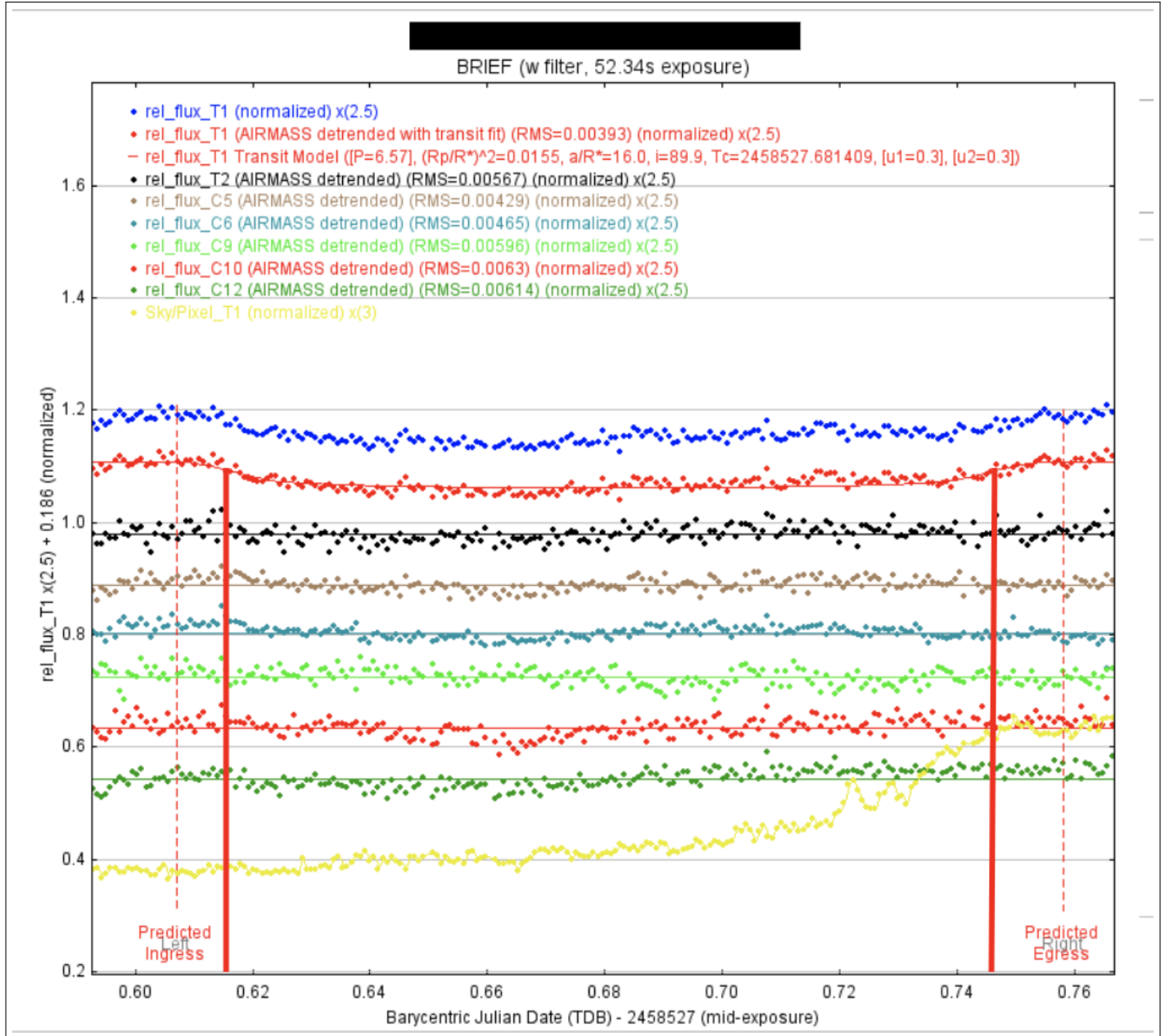


**Fig. 12.** The solid red lines represent the actual ingress and egresses.

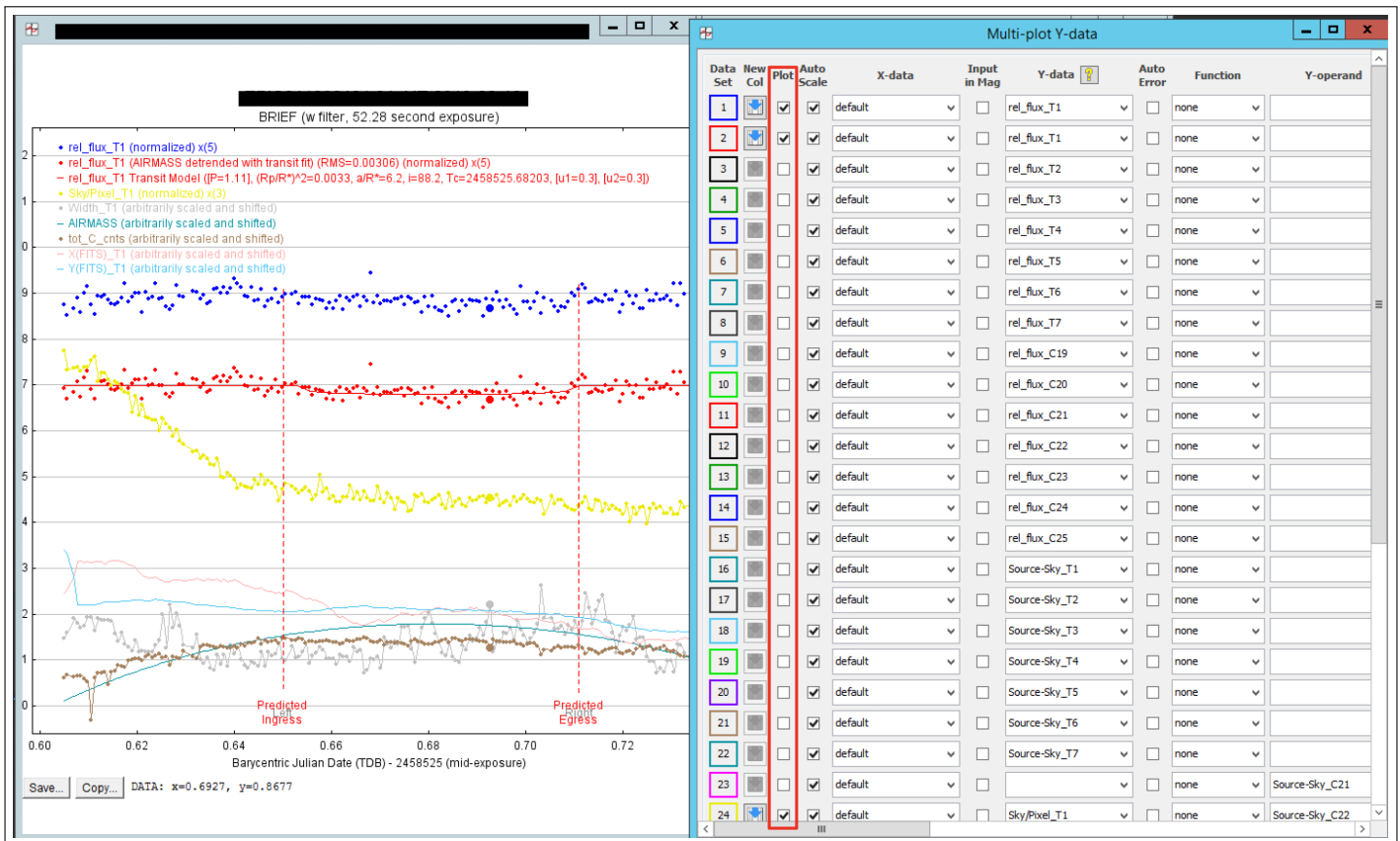


**Fig. 13.** A simple technique to use when modeling light curves. This will save time and increase accuracy.

section, a few common “case studies” will be covered along with how to handle them appropriately.

One possible cause of erroneous plots (plots that have seemingly no pattern in the data and lack form) is if the distance between the closest star and the target star (determined by going to the NEB folder created after doing NEB analysis, clicking on the first NEB depth plot, and then looking to see how far it is) is smaller than the aperture (aperture size can be checked from the seeing profile). Refer to Figures 19 and 20. This closest star could therefore contaminate the target star measurement, as its size isn’t accurately accounted for by the given aperture. Thus, by using a smaller aperture, the amount of potential contamination of the target star measurement is reduced (using a smaller aperture size of half the original is usually safe). On the other hand, if the closest Gaia star is, for example, 20 arc-seconds away from the target and the aperture that is used is around 5 arc-seconds, a second smaller aperture is not necessary. The used aperture size will need to be included the observation email though so that reviewers/future researchers are aware that the aperture was correctly accounted for.

One of the most important aspects in analyzing the light curve is the depth of the light curve. Normally, a shallow depth would indicate that “no clear detection” was found. But, if the predicted depth, as stated in the TTF (as shown back in Figure 1), is also a small number, then it cannot necessarily be concluded that “no clear detection” was found. Vice versa, if the predicted depth is significantly larger than the light curve’s depth on the plot, then it may be appropriate to deem that “no clear detection” was found. “Detection” in this case refers to any detection of a possible exoplanet or eclipsing binary transiting across the host star.

NEBs are commonplace in this analysis. When one star orbits in front of its binary counterpart, a light curve is produced that is very similar to a light curve generated from planet orbiting across its host star. This is why NEBs are called “false positives.” One way to determine whether data has a NEB is through the Dmag vs. RMS plot (Figure 21). RMS is essentially the amount light curve scatter, of which depends on the size of the photometric aperture. If there are any major outliers on the curve (which should have a general trend line of exponentiality), then these

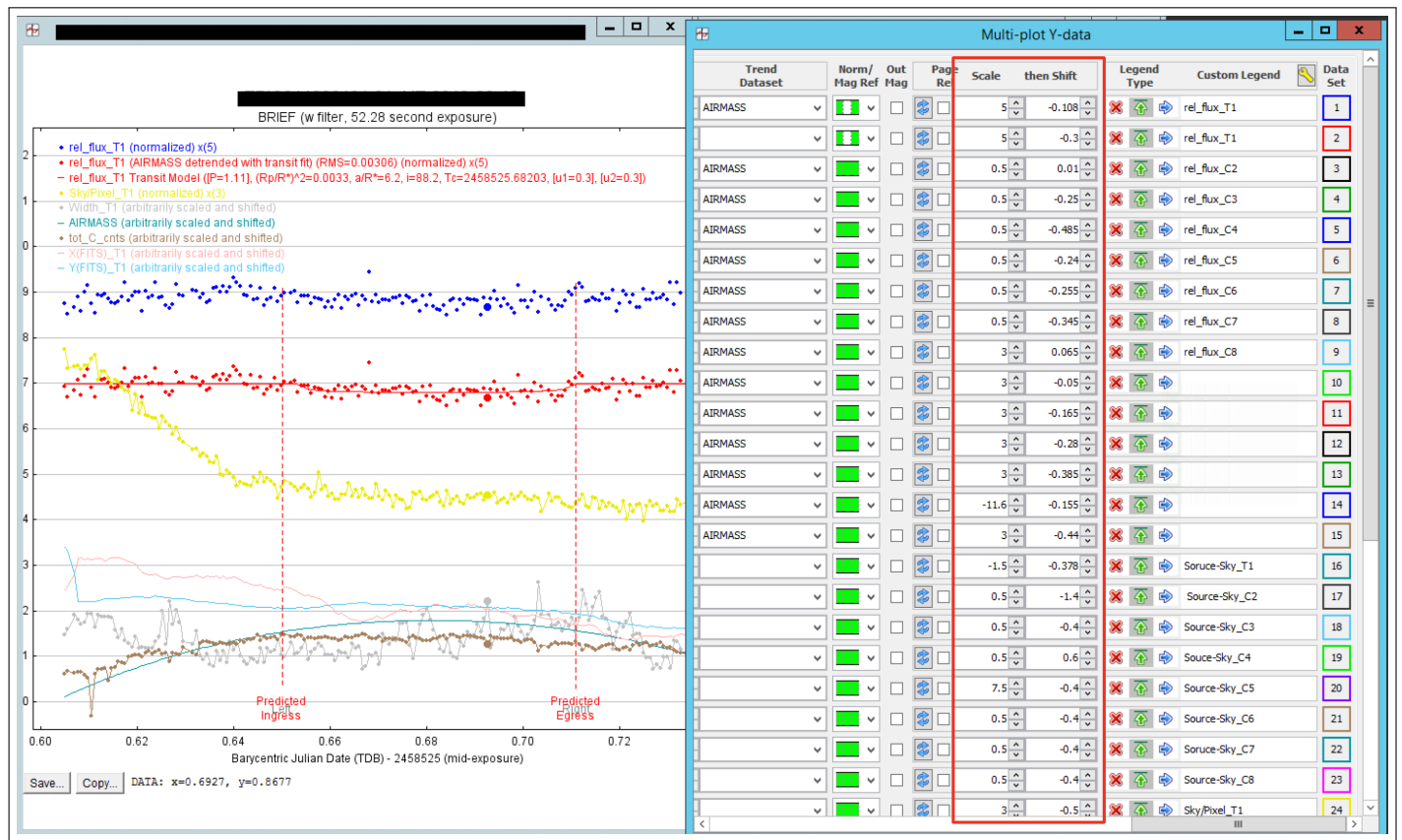


**Fig. 14.** This figure shows the right half of the Multi-Plot Y-Data Screen. The Scale and Then Shift settings for the curves are boxed in red.

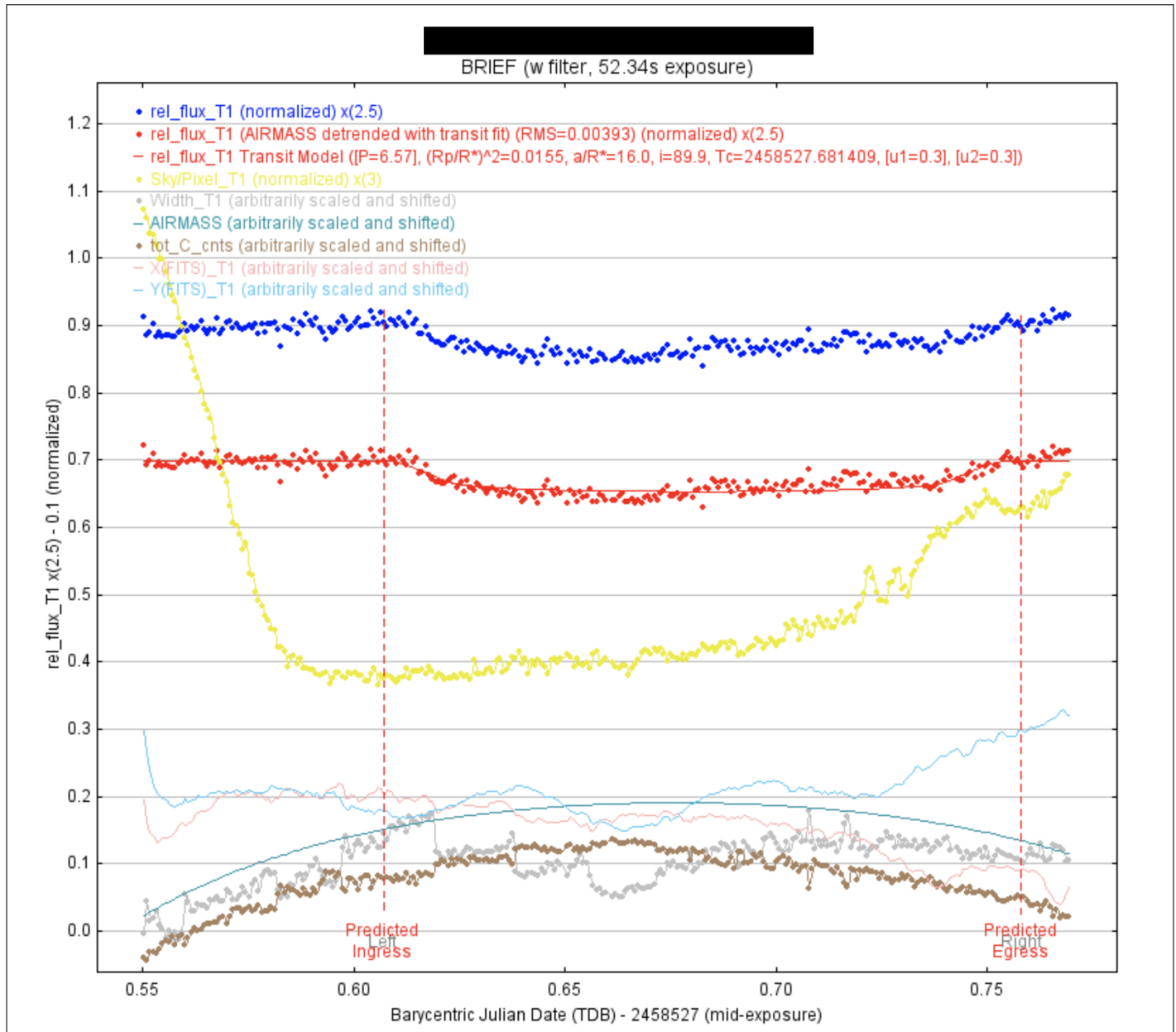


**Fig. 15.** Curves and other data should be spread out for readability purposes.



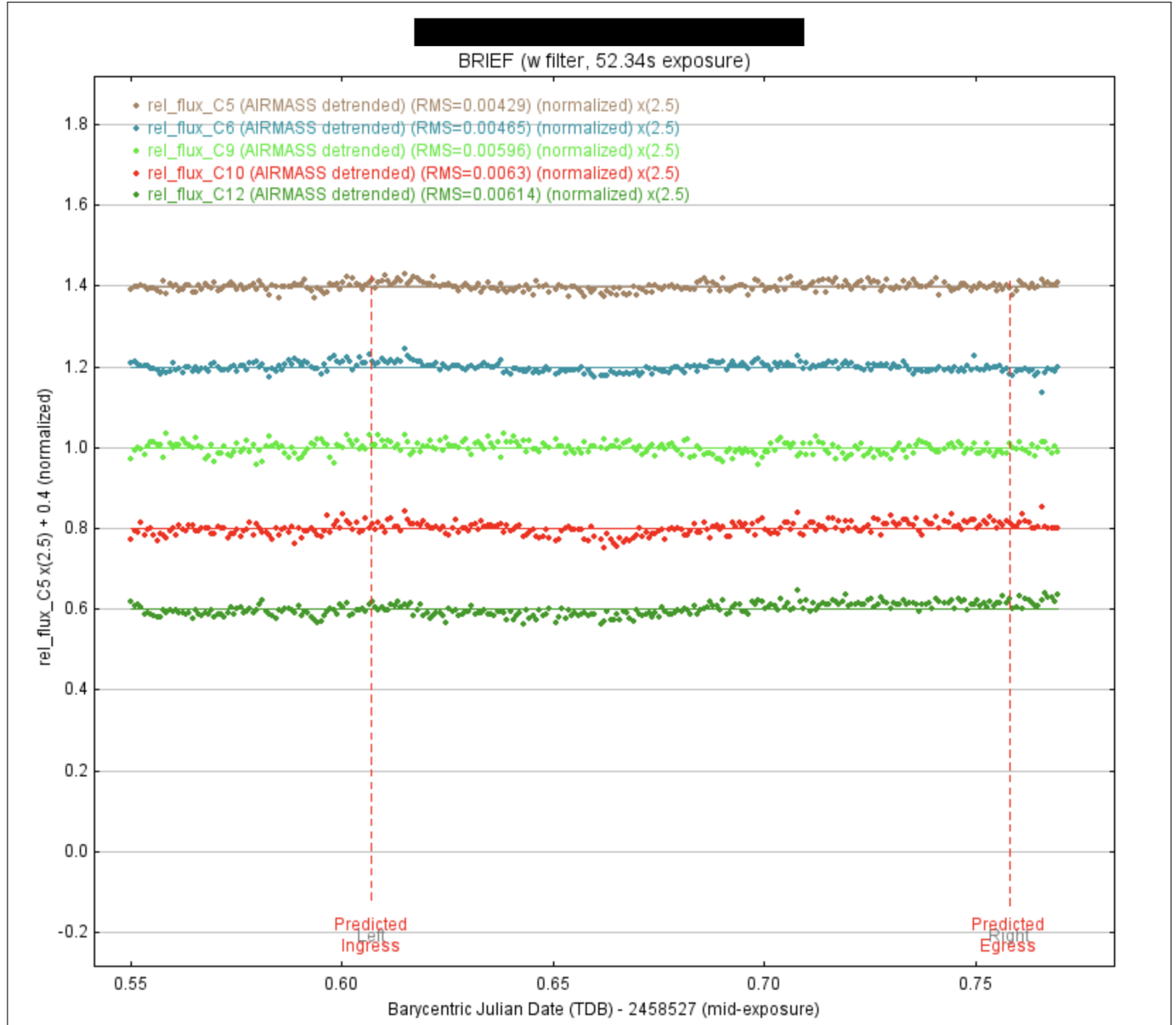


**Fig. 16.** The light curves of comp stars will often need to be graphed on a separate plot to avoid a single, cluttered graph. Mindful spacing applies.

**Data Set 2 Fit Settings**

File Auto Priors

rel\_flux\_T1

**User Specified Parameters (not fitted)**

**Orbital Parameters**

Period (days)  Cir ☒ Ecc   $\omega$  (deg)

**Host Star Parameters (enter one)**

Sp.T.  Teff (K)  J-K  **R\* (Rsun)**  M\* (Msun)  p\* (cgs)

**Transit Parameters**

☒ Enable Transit Fit ☒ Auto Update Priors

Parameter	Best Fit	Lock	Prior Center	Use	Prior Width	Cust	StepSize
Baseline Flux (Raw)	0.367433408	<input type="checkbox"/>	0.366937928	<input type="checkbox"/>	0.073387586	<input type="checkbox"/>	0.1
$(R_p / R_*)^2$	0.003886504	<input type="checkbox"/>	0.003056716	<input type="checkbox"/>	0.001528358	<input type="checkbox"/>	0.003056716
a / R*	9.049866707	<input type="checkbox"/>	7.028613391	<input type="checkbox"/>	7.0	<input type="checkbox"/>	1.0
T <sub>C</sub>	2458687.618354768	<input type="checkbox"/>	2458687.60975	<input type="checkbox"/>	0.015	<input type="checkbox"/>	0.01
Inclination (deg)	84.746652807	<input type="checkbox"/>	85.5	<input type="checkbox"/>	15.0	<input type="checkbox"/>	1.0
Linear LD u1	0.300000000	<input checked="" type="checkbox"/>	<b>0.3</b>	<input type="checkbox"/>	1.0	<input type="checkbox"/>	0.1
Quad LD u2	0.300000000	<input checked="" type="checkbox"/>	<b>0.3</b>	<input type="checkbox"/>	1.0	<input type="checkbox"/>	0.1
Calculated from model	b <input type="text" value="0.829"/> t14 (d) <input type="text" value="0.017393"/> t14 (rms) <input type="text" value="00:25:03"/> t23 (d) <input type="text" value="0.011476"/> tau (d) <input type="text" value="0.002958"/> p* (cgs) <input type="text" value="25.5814"/> (e)SpT <input type="text" value="&lt;M8V"/> Rp (Rjup) <input type="text" value="1.23"/>						

**Detrend Parameters**

Use	Parameter	Best Fit	Lock	Prior Center	Use	Prior Width	Cust	StepSize
<input checked="" type="checkbox"/>	AIRMASS	-0.005793195535	<input type="checkbox"/>	0.0	<input type="checkbox"/>	1.0	<input type="checkbox"/>	0.1
<input type="checkbox"/>	Width_T1		<input type="checkbox"/>	0.0	<input type="checkbox"/>	1.0	<input type="checkbox"/>	0.1
<input type="checkbox"/>	Sky/Pixel_T1		<input type="checkbox"/>	0.0	<input type="checkbox"/>	1.0	<input type="checkbox"/>	0.1
<input type="checkbox"/>	X(FITS)_T1		<input type="checkbox"/>	0.0	<input type="checkbox"/>	1.0	<input type="checkbox"/>	0.1
<input type="checkbox"/>	Y(FITS)_T1		<input type="checkbox"/>	0.0	<input type="checkbox"/>	1.0	<input type="checkbox"/>	0.1
<input type="checkbox"/>	tot_C_cnts		<input type="checkbox"/>	0.0	<input type="checkbox"/>	1.0	<input type="checkbox"/>	0.1
<input type="checkbox"/>	BJD_TDB		<input type="checkbox"/>	0.0	<input type="checkbox"/>	1.0	<input type="checkbox"/>	0.1
<input type="checkbox"/>	Meridian_Flip		<input type="checkbox"/>	0.0	<input type="checkbox"/>	1.0	<input type="checkbox"/>	0.1

**Fit Statistics**

Fit Statistics  RMS (norm)   $\chi^2/\text{dof}$   BIC  dof   $\chi^2$

**Plot Settings**

☒ Show Model ☒ Show in legend Line Color  Line Width

☐ Show Residuals ☒ Show in legend ☐ Show Error Line Color  Line Width  Symbol  Symbol Color  Shift

**Fit Control**

Fit Control ☒ Auto Update Fit  Fit Tolerance  Max Allowed Steps  Steps Taken

**Fig. 17.** The Data Set 2 Fit Settings improves the "fit" of the light curve.

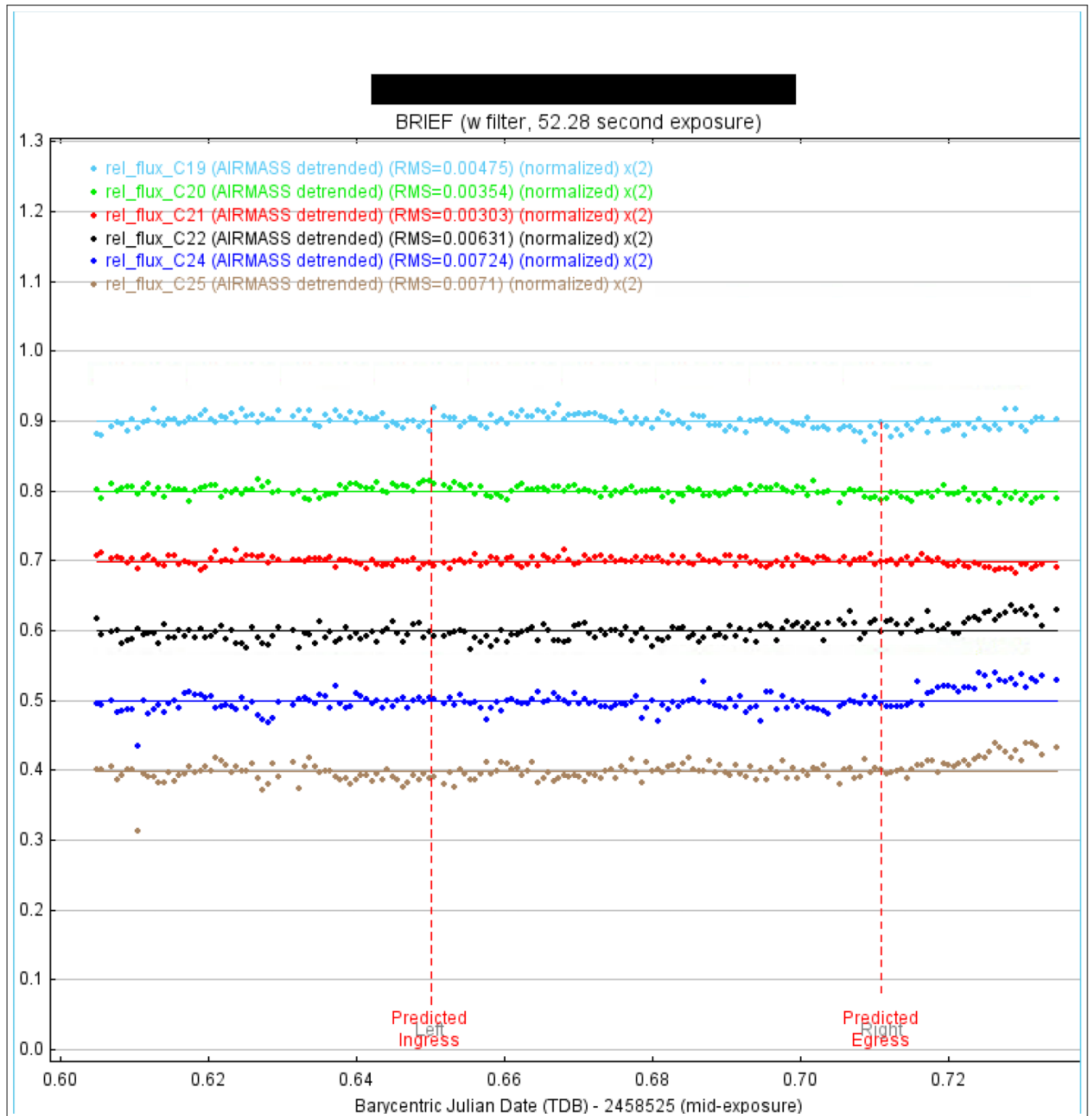


**Fig. 18.** Notice how the points nicely follow the line of best fit that runs through them.

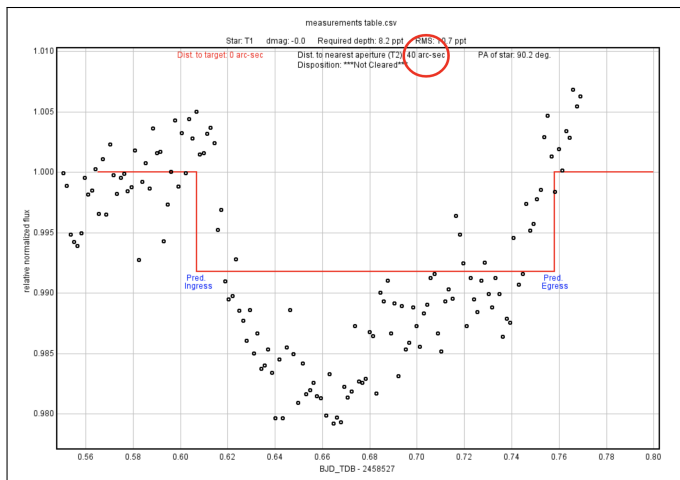


**Fig. 19.** The NEB Depth Plot of the Target Star. The distance, in arc-seconds, of the Target Star to the closet target star (from GAIA) is circled in red.

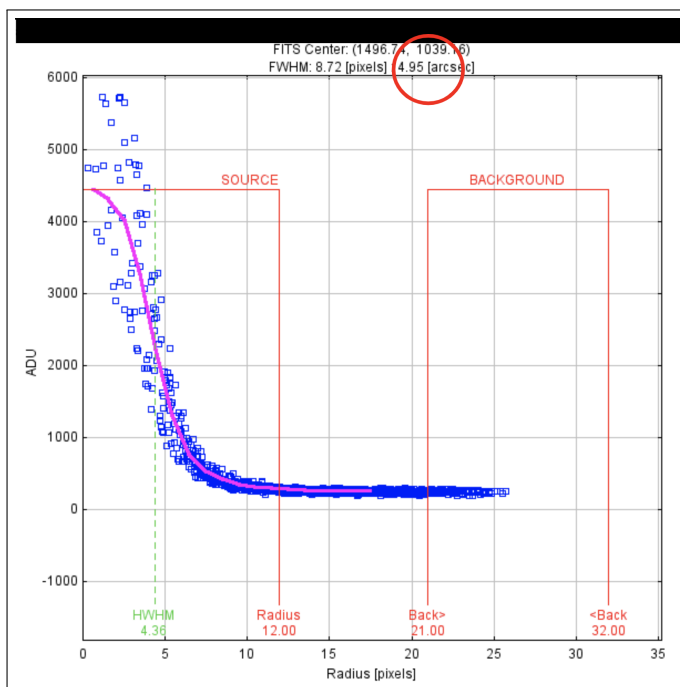


**Fig. 20.** The Seeing Profile shows the various radii of the aperture, inner, and outer annuli. The red circle shows the aperture of the instrumentation used to obtain the images.

target/comparison stars are usually either NEBs, EBs, or other objects of interest.

Another way to discern NEBs is using the NEB Table (Figure 22). This list stars that are “Cleared, likely cleared,” “too faint,” or “not cleared.” “Cleared” in this case means that it is cleared of not being a potential NEB, where “not cleared” means that a star could possibly be a NEB. Other keyword definitions are defined on the NEB Table.

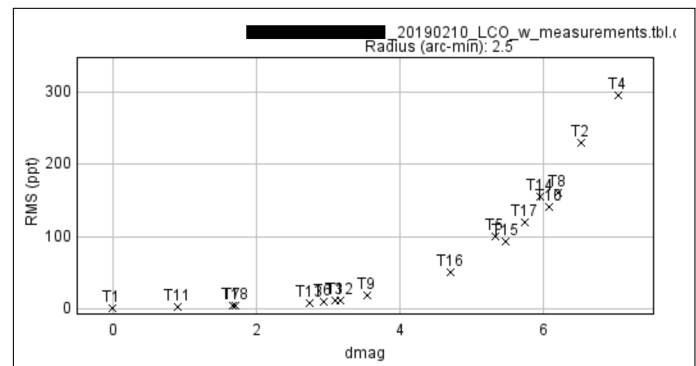


**Fig. 21.** Dmag vs. RMS Plot: Comp stars should compose an exponential curve; if certain stars deviate substantially, then they might be an NEB or EB.

## THE “REAL” CASE STUDIES

In terms of categorizing a light curve and drawing conclusions, There are three predefined "cases."

The categorization of the target of interest is "Case 1" if there's a clear “dip” on the target star's light curve and there aren't any false positives (as stated by the NEB Table or other aforementioned methods). It should look like the light curve presented in Figure 23. Case 1 often leads to planet candidates.

The target star should be categorized as Case 2 if non-target stars (outside the 2.5' radius) show an "event"—a dip in its light curve. Case 2 basically states that a NEB, or another possible planet candidate, is the cause of the event because it's outside the target star's region. Case 2 evidence, apart from just the light curve, can be found in the NEB Table, Dmag. vs. RMS Plot, and other resources mentioned in "Case Studies." However, be prepared for further investigation and validation from more experienced researchers.

If not Case 1 or Case 2, then the target of interest may be Case 3 which is defined as no events being detected by the target star nor with any checked, nearby

## TFOP NEB Search Table for:

20190210\_LCO\_w\_measurements.tbl.csv

Created by AIJ macro Revision 2.15  
on 2019-06-04

-----  
Pixel Scale (arc-seconds/pixel): 0.57  
Predicted ingress time: .650  
Predicted egress time: .711  
Target predicted depth: 7.9  
Target Star: T1  
Search Radius: 2.5  
Duration of Observation (min.): 187.1  
Number of Images: 179  
Average Exposure Plus Delay Time (sec.): 62.7  
Cadence Requested When Calculating RMS (sec.): 180.0  
Binning Used When Calculating RMS: 2  
Average Aperture Radius: 8.0 (pixels); 4.6 (arc-seconds)  
Dmag correction factor to account for difference with TESS band:-0.5

Star	Separation from target	PA (deg.)	Uncorr. dmag	RMS(ppt)	NEBdepth(ppt)	NEBdepth/RMS	Disposition
T2	0'20"	304	6.531	231.32	2041.2	8.8	Cleared-too faint
T3	0'38"	136	3.102	12.88	86.8	6.7	Cleared
T4	0'39"	165	7.040	298.27	3263.8	10.9	Cleared-too faint
T5	0'43"	174	5.325	102.39	672.4	6.6	Cleared
T6	0'50"	152	2.934	11.49	74.4	6.5	Cleared
T7	1'01"	159	1.670	6.21	23.2	3.7	Likely cleared
T8	1'08"	300	6.208	162.66	1516.5	9.3	Cleared-too faint
T9	1'32"	175	3.545	20.47	130.6	6.4	Cleared
T10	1'35"	180	6.086	143.60	1354.9	9.4	Cleared-too faint
T11	1'43"	65	0.903	3.60	11.5	3.2	Likely cleared
T12	1'50"	42	3.170	13.66	92.4	6.8	Cleared
T13	1'51"	95	2.738	10.41	62.1	6.0	Cleared
T14	1'54"	101	5.950	157.24	1195.9	7.6	Cleared-too faint
T15	1'55"	174	5.472	94.38	770.1	8.2	Cleared
T16	1'59"	221	4.700	52.47	378.1	7.2	Cleared
T17	2'04"	36	5.741	122.31	986.0	8.1	Cleared
T18	2'09"	115	1.711	6.70	24.1	3.6	Likely cleared

Possible dispositions of the star being the source of the target predicted depth:

Likely cleared (NEBdepth/RMS is between 3 and 5)

Cleared (NEBdepth/RMS is  $\geq 5$ )

Cleared-too faint (NEBdepth  $\geq 1000$ ppt)

\*\*\*Not Cleared-flux too low\*\*\* (weighted average of Source-Sky counts per aperture pixel  $< 2$ )

\*\*\*Not Cleared\*\*\* (none of the above conditions are met)

Image shift statistics:

stdev.(arc-seconds): 3.3455 in X and 3.6058 in Y

max. deviation (pixels): 19.9961 in X and 48.3511 in Y

**Fig. 22.** NEB Table: Characterizes the likelihood of each of the GAIA-determined potential target stars being NEBs.



stars. Case 3 is often deduced by process of elimination. Sometimes there may be an extremely slight dip in the light curve, causing the analysis to be in the grey-area between Case 1 and Case 2. In this context, it is recommended to state the findings instead of ascribing them to a certain case. Also, further judgments about classification of what analysis yields can be offered by review teams.

## NEEDED FILES

After analysis is complete, a researcher has to compile twelve total files for submission to ExoFOP TESS.

- **File 1: Measurements Table.** Referenced in the Transit Modeling Phase. This table is created upon completion of the Calibration Phase.
- **File 2: Plot Configuration File.** This file is downloaded upon completing the Transit Modeling Phases (reference respective section).
- **File 3: Apertures File.** This file is created upon completing the Transit Modeling Phase and when "save all" is selected. Essentially, this file saves all the selected target and comp stars. Thus, if the Differential Photometry Phase needs to be re-done, the previous apertures will be available to be referenced.
- **File 4: Light Curves.** Reference Transit Modeling Phase. These curves are the heart and soul of the transit-photometry analysis.
- **File 5: Field Image with Apertures.** Refer to the Differential Photometry Phase. This is "screenshot" of the field with the GAIA stars, comp stars, and 2.5' arcsecond circle around the target star. This is necessary for TESS professionals to reference which comp stars correspond to various curves on the light curve plots.
- **File 6: Plate Solved Image.** This is not a screenshot, but rather the file itself. Since the OSS Pipeline will be utilized, the images will automatically be plate-solved.
- **File 7: Seeing Profile.** Refer to the Case Studies/Analysis of Light Curves Section. The seeing profile is created by right-clicking the target star (or by finding the respective option in the main toolbar of the image). The seeing profile provides aperture size recommendations.
- **File 8: Notes and Results Text File.** Refer to *TFOP SG1 Observation Guidelines* page 14. This file essentially includes the classification of the potential exoplanet along with any other conclusions made from the data.
- **File 9: Delta Magnitude (Dmag) vs. RMS plot.** This plot is a useful tool in determining potential NEBs. Reference the Case Studies/Analysis of Light Curves Section for a full description.
- **File 10: NEB Table.** This table is also instrumental in determining false positive. Refer to the Case Studies/Analysis of Light Curves Section.
- **File 11: A zip file that contains NEB Depth Plots for comp and target (GAIA) stars.** These plots show the "shallowest event required for that star to mimic the TESS predicted transit depth" (Conti, 2019).
- **File 12: A Zoomed-in Field-of-View Image.** This screenshot should show only the stars within the 2.5 arcsecond circle. The purpose lies in showing more detail to the individual brightnesses of each potential NEB within the GAIA field-of-view. Further explanations can be found *TFOP SG1 Observation Guidelines*.

## CONCLUSION

This paper is a guide that helps SG1 TESS researchers avoid the common pitfalls of aperture photometry in AIJ. These pitfalls were documented by the BRIEF team who noticed the common mistakes that students were making in their exoplanet analyses.

Categorized into four different sections, this paper mirrors the set-up of Dennis Conti's *A Practical Guide to Exoplanet Observing* (Conti, 2018) in order to simplify the exoplanet analysis as well as to coordinate cross usage between this paper and other AIJ Guides.

## ACKNOWLEDGMENTS

Special thanks to the Boyce Research Initiatives and Research Foundation for the opportunity to learn about this amazing field of exoplanets and introducing me to the cutting-edge TESS research. Further thanks goes to Dr. Dennis Conti in being a pioneer in making high-level exoplanet research more understandable and accessible to the masses. Also, big thanks goes to Dr. Scott Dixon for helping me on a day-to-day basis learn the specific methodology of

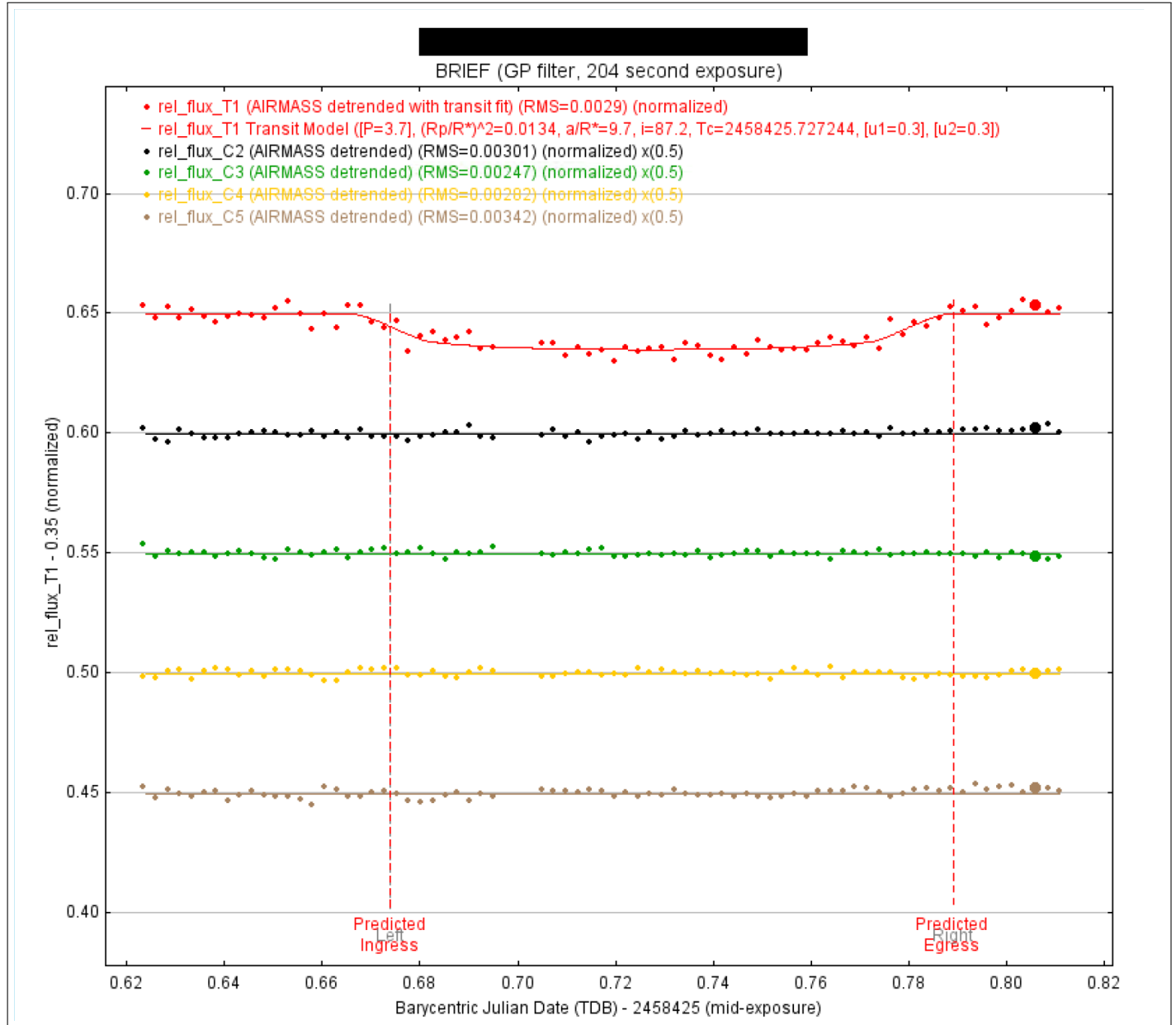


**Fig. 23.** Taken from real TESS data, this light curve represents an ideal situation where there's a nice dip and non-skewed comp stars.

photometric analysis. Lastly, another big appreciation for Michael Fitzgerald for plate-solving the images through the OSS Pipeline, serving to streamline the research.

## REFERENCES

- Boyce, P., Boyce, G., Dixon, S., Conti, D., Falatoun, A., Wiley, E., ... Ha, J. (2019). *The astroimagej guide for lco - tess observations processed through the oss pipeline*.
- Brown, T., Baliber, N., Bianco, F., Bowman, M., Burleson, B., Conway, P., ... others (2013). Las cumbres observatory global telescope network. *Publications of the Astronomical Society of the Pacific*, 125(931), 1031.
- Conti, D. M. (2018). *A practical guide to exoplanet observing*.
- Conti, D. M. (2019). *Tfop sg1 observation guidelines*.
- Fitzgerald, M. (2018). The our solar siblings pipeline. *RTSRE Proceedings*, 1(1), 347–358.